MINISTRY OF EDUCATION, RESEARCH, YOUTH AND SPORT

THE ANNALS OF "DUNAREA DE JOS" UNIVERSITY OF GALATI

Fascicle IX
METALLURGY AND MATERIALS SCIENCE

YEAR XXIX (XXXIV),
December 2011, no. 4

ISSN 1453-083X

2011
GALATI UNIVERSITY PRESS

THE ANNALS OF "DUNAREA DE JOS" UNIVERSITY OF GALATI.
FASCICLE IX. METALLURGY AND MATERIALS SCIENCE
N^0. 4 – 2011, ISSN 1453 – 083X

Table of Content

THE ANNALS OF "DUNAREA DE JOS" UNIVERSITY OF GALATI.
FASCICLE IX. METALLURGY AND MATERIALS SCIENCE
N^0. 4 – 2011, ISSN 1453 – 083X

INVESTIGATING TRIBOLOGICAL PROCESSES IN POLYMERIC COMPOSITES*

Lorena DELEANU, Constantin GEORGESCU, Constantin GHEORGHIEŞ
"Dunarea de Jos" University of Galati
email: lorena.deleanu@ugal.ro

ABSTRACT

The paper presents some results on investigation of the superficial layers of several polymeric composites intended for tribological applications. The evaluation of the tribological behavior is done with the help of SEM images, virtual images obtained by 3D profilometry and X-ray diffractometry.

KEYWORDS: tribology, polymeric composites, 3D profilometry, X-ray diffractometry, SEM, optical microscopy

1. The necessity of non-destructive investigations in tribology

One of the general trends is the development of the integrated systems, with high degree of automatization in industry including manufacturings, energetics and transports. These systems necessitate a closer control and are vulnerable to failures, reducing the failure consequences being nowadays a design criterion due to the associated risks for the economical organizations, environment, labour force and population and for avoiding financial and time deadlines losses. Failures and damages of the machine elements, especially those produced by tribological processes, have an undesirable high percentage in making the systems unavailable (Fig. 1).

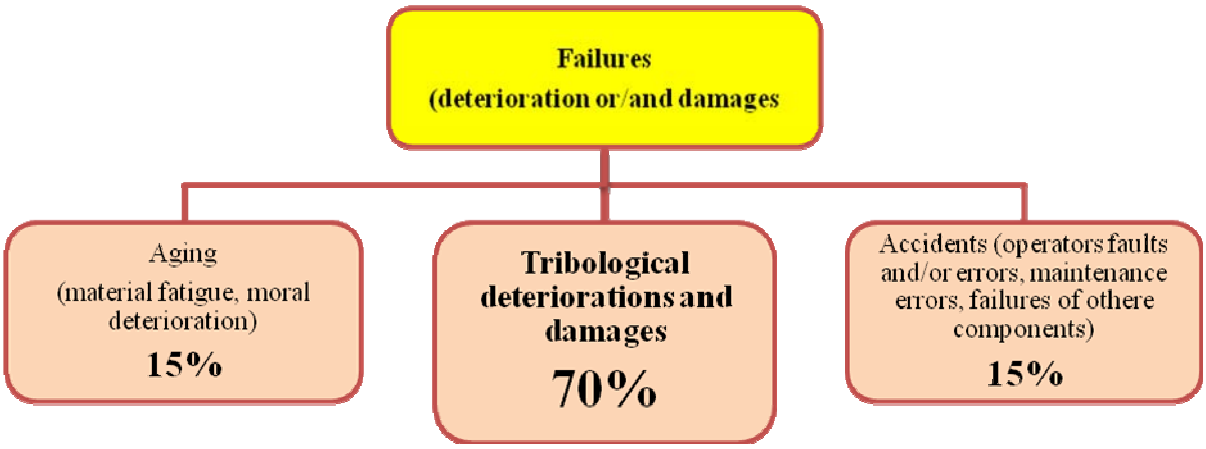

Fig. 1. *Percentage distribution of tribological deteriorations.*

Studies and researches in this field of tribology have a determinant influence in improving reliability and durability, starting from design but also in maintenance and diagnosis of the complex systems [1, 8, 41].

*Paper presented at the Symposium ***"The Impact of Nanotechnologies and Nanomaterials on Industrial Development and Quality of Life",*** Galati, May 19, 2011, organized by the Center for Nanostructures and Functional Materials (CNMF), Faculty of Metallurgy, Materials Sciences and Environment, "Dunarea de Jos" University of Galati

There are generally admitted that the economic loss due to wear represents 6...10% from the gross national product of the developed countries and 30% of the failures of mechanical systems are caused by wear (Fig. 2) [1, 37].

The analysis of a tribological deterioration (Fig. 3) is usually included in a failure analysis or it could be the subject of an exploratory research in order to optimize the tribological behaviour of the system. Monitoring the tribological tests is difficult as it implies sophisticated and accurate equipment and alteration in a certain manner of the tribotester by introducing sensors [8, 9, 11, 15]. The tribologists have to prove inventivity for establishing a testing methodology with results that could be applied in practice.

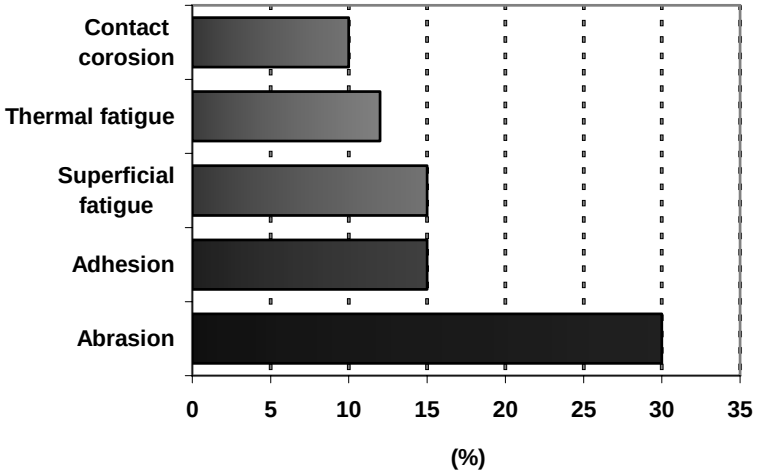

Fig. 2. *Percentage of different types of wear in the wear deteriorations.*

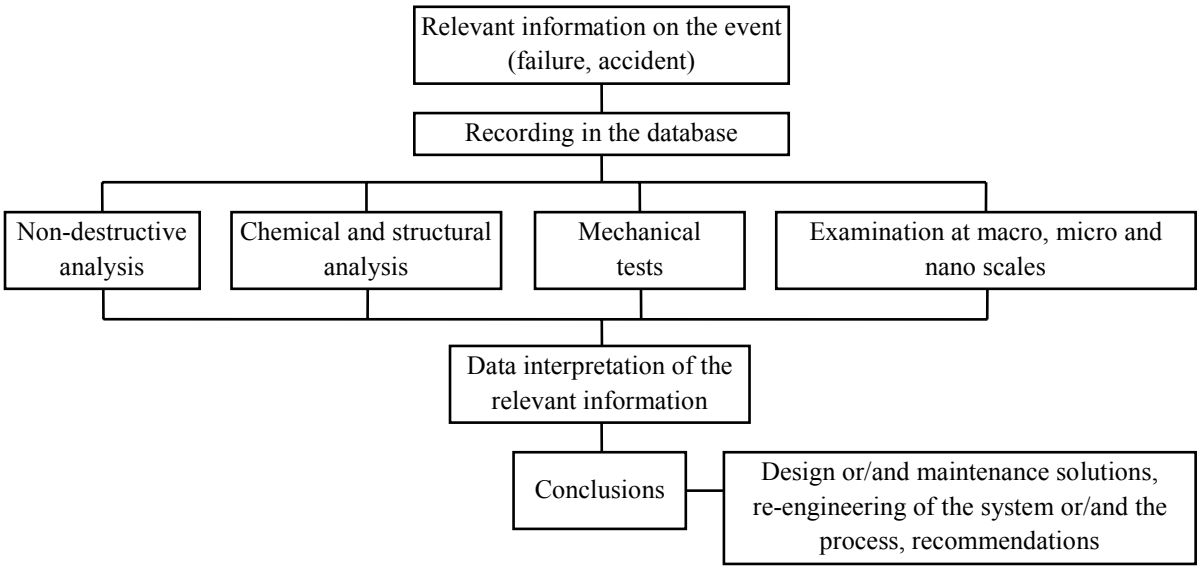

Fig. 3. *The chart for analysing a tribological deterioration.*

2. On polymeric composites

The polymeric composites are materials obtained by mixing different materials using a polymeric matrix: one or more adding materials could play the role of the reinforcement (Fig. 4) or/and of the solid lubricant. For other than mechanical applications the adding material could modify the physical, thermal and chemical response of the composite [2, 29].

Why are there so many grades of composites with polymeric matrix? The answer is given by the large ranges for the physical, thermal, mechanical, tribological properties of the constituent phases (two, three or even more) with very different concentrations. Even the polymer matrix could be

selected from many polymers [4, 7, 15] depending on the application. This diversity may offer solutions for a particular application taking into account the movement, the loading and speed regime, the lubrication, the working temperature, the environment.

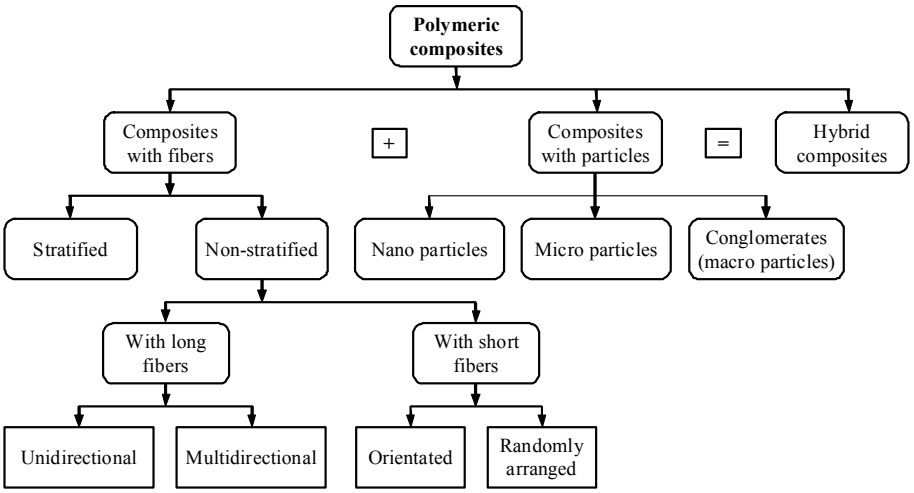

Fig. 4. *A classification of polymeric composites based on the shape and dimension of the adding materials.*

2.1. Tribological behaviour

The tribological behaviour of a polymeric composite is complex, including the tribological parameters and it has to explain the interconditionality of the influencing factors [5, 10, 29, 34, 37]. Tests on simpler triboelements such as pin-on-disk, block-on-ring etc., are easier to investigate and to identify the processes and the synergic influence of two or many factors.

The tribological behaviour means establishing relationships among influencing factors and tribological parameters such as friction coefficient, wear and wear rate, thermal field, structural and chemical changes, modifications of the physical and mechanical properties of the materials in contact, but also for the lubricant and the environment, changes of the surfaces topography etc.

2.2. Processes within the superficial layers of the polymeric composites

A synthesis of these processes is given in Figure 5 based on the recent references [6, 15-19, 25-26, 30, 34, 37, 38].

Taking into account the research field the authors are involved in [11-14, 20, 28, 39], the tribological processes of the polymeric composites are exemplified with the help of composites with PTFE and PA matrix, the polymers being kept as reference. PTFE [32, 33, 39, 40] and polyamide [8, 22, 27, 31, 35, 36] are two polymers frequently used as matrix due to their tribological behaviour.

3. Non-destructive analysis

Non-destructive analyses are preferable because they do not alter the structure or/and composition of the superficial layers [41], but there are limitations in monitoring the contact by non-invasive and non-destructive techniques.

3.1. Optical microscopy

This observation method has the advantage of easy preparation of the samples, sometimes they do not have to be cut from the tested pieces and nowadays there are available optical microscopes with high performances. One of the disadvantages is the magnification from 50...1400 (at least in our laboratory): a good resolution depends on the studied materials and on the quality of the worn surfaces. Sometimes scale like 200:1, 500:1 are preferable because they give images of the superficial layers allowing to understand the statistical characteristic of the processes. Figure 6 presents several PTFE composites and each image pointed out characteristics of the superficial layers. These scales are useful for evaluating, in a statistical and qualitative manner, the dominant processes within the superficial layers.

4. Scanning electron microscopy (SEM)

Scanning electron microscopy offers information about the sample's surface topography, composition and other properties such as electrical conductivity.

It has the advantage of high magnification 100...6000 (at least for the author's experience on polymers and polymeric composites and for the available equipment at our University).

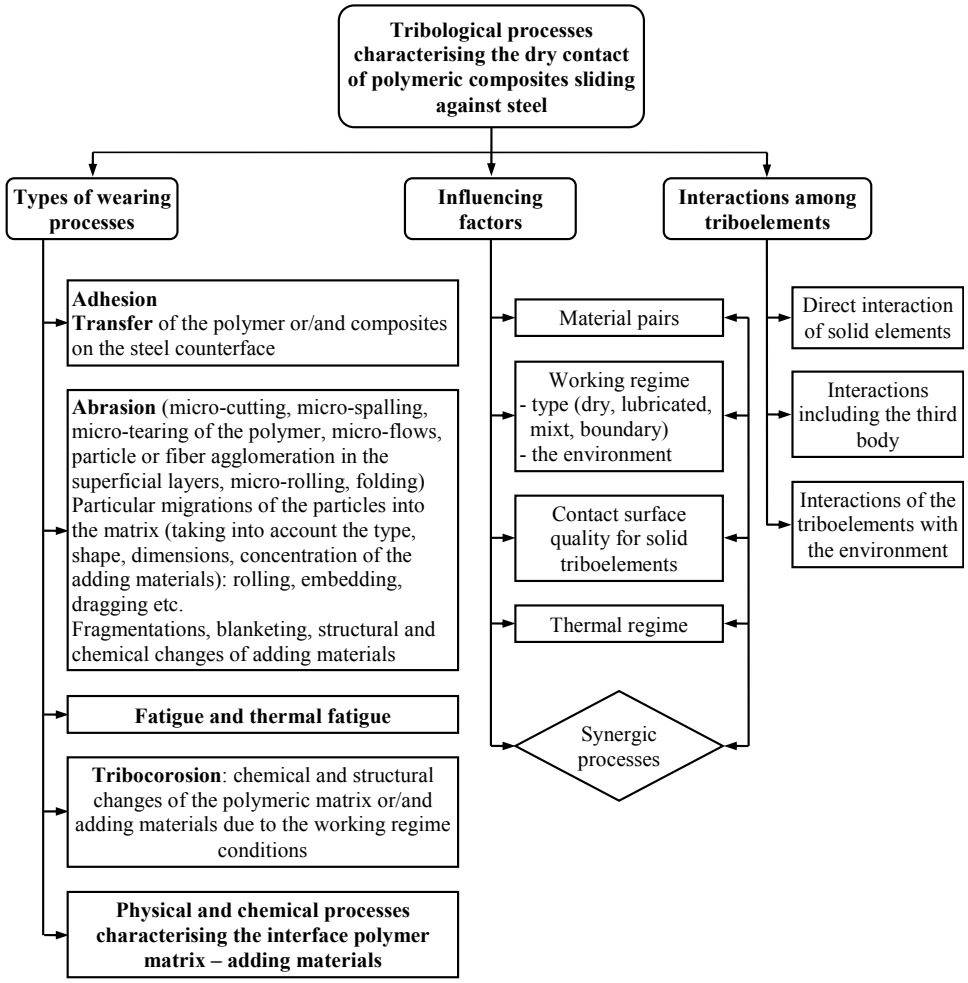

Fig. 5. *An overview of the tribological processes characterising the dry contact of polymeric composites sliding against steel.*

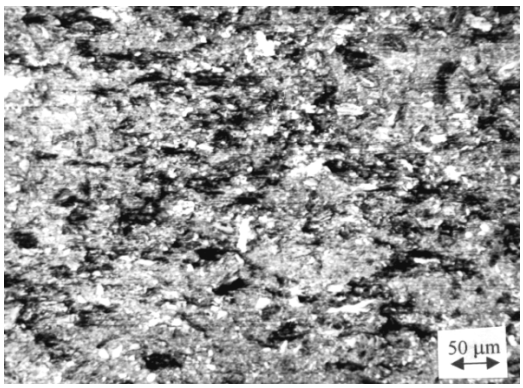

c) PTFE + 23% carbon + 2% graphite: micro flows of PTFE in the sliding direction and a mixing process of the polymer and carbon components into the superficial layer

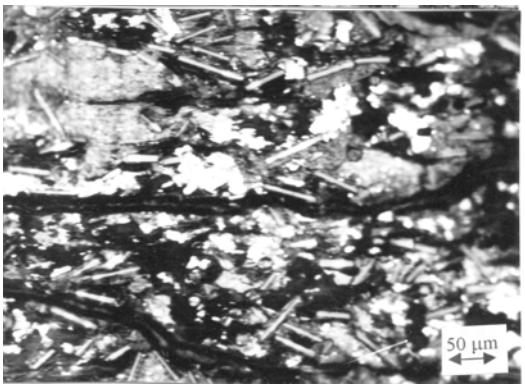

d) PTFE + glass fiber + graphite: fiber orientation in the sliding direction and micro flow of polymer and graphite mix

Fig. 6. *Dry sliding against steel, p =0.76 MPa, v =1 m/s Tribotester shoe/roller (Ra=0.8...1.2 µm) [13, 39].*

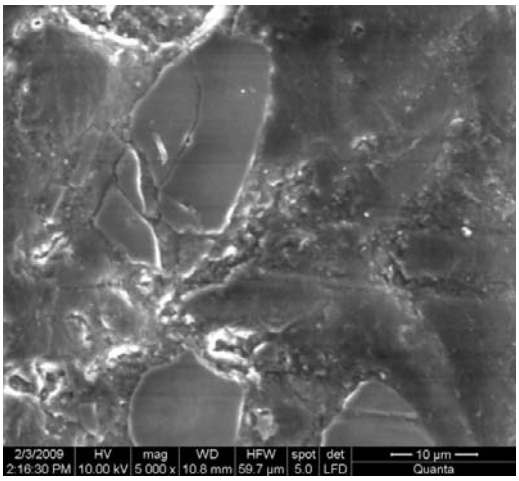

a) PTFE +15% glass fiber; particular processes: a broken glass fiber, fragments embedded in the PTFE matrix; local flow of the polymer and wear debris adhering among the fibers [13, 39]

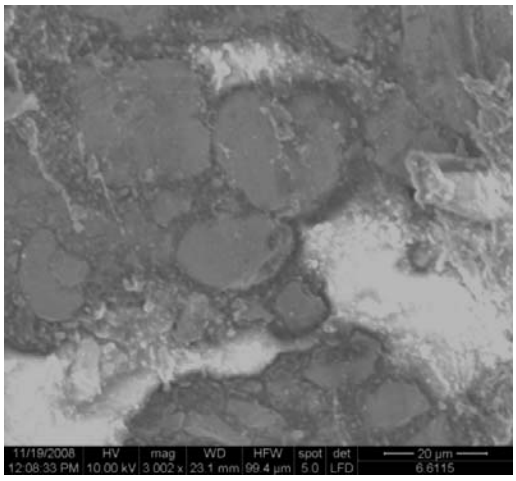

b) PTFE + 60% bronze; particular processes: very thin bands of polymer torn off from the matrix and spread on the hard constituent, explaining low friction and reduced wear [13, 39]

Fig. 7. *SEM images revealing processes influencing friction and wear of the tribosystem*

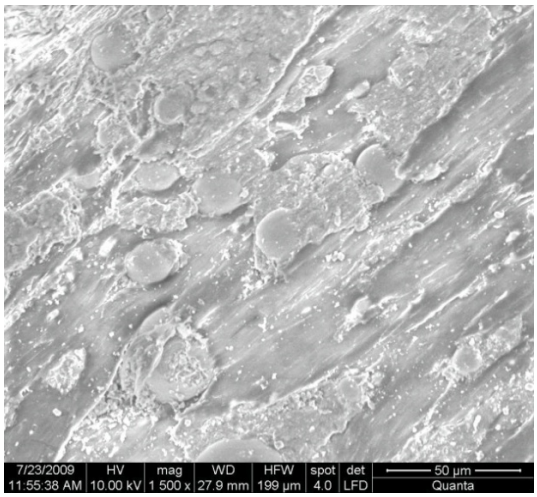

a) p=2 MPs, v=0.5 m/s

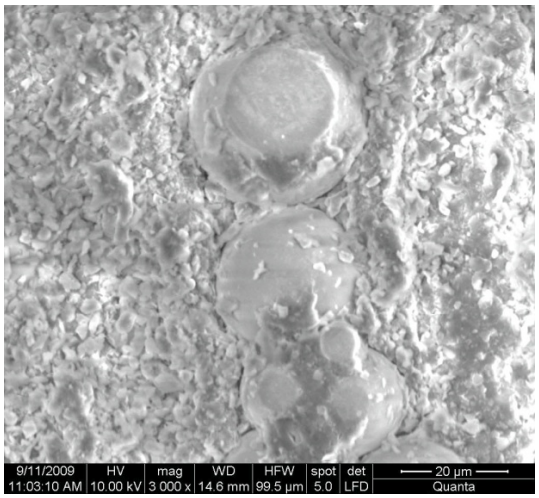

b) p=3 MPa, v=1.5 m/s

Fig. 8. *Influence of the sliding speed on the processes taking place into the superficial layers of the composite polyamide +20% micro glass spheres, after dry sliding of a steel pin on the composite disk [29].*

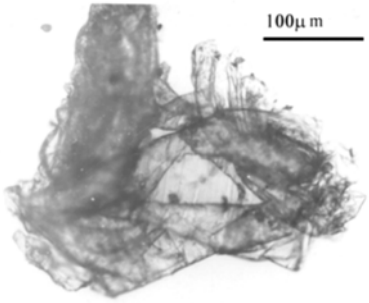

Fig. 9. *Wear particle from a shoe made of PTFE, dry sliding (p=0.76 MPa and v=0.5 m/s).*

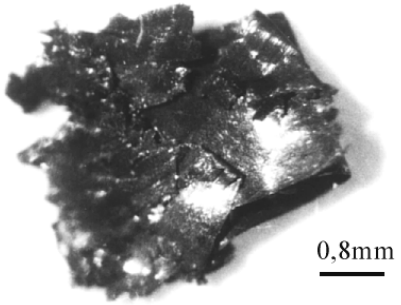

Fig. 10. *Wear particle from a shoe made of PTFE + 60% bronze, water lubrication (p=0.76 MPa and v=0.5 m/s).*

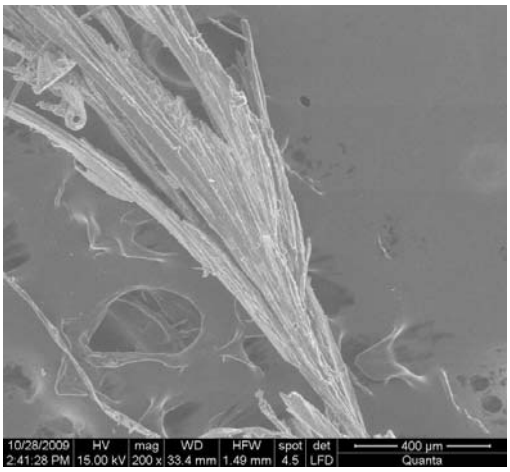

Wear particle obtained after dry sliding 10 km at v=1 m/s, p=1 MPa, pin-on-disk, disk made of polyamide, pin made of steel (background - carbon strip)

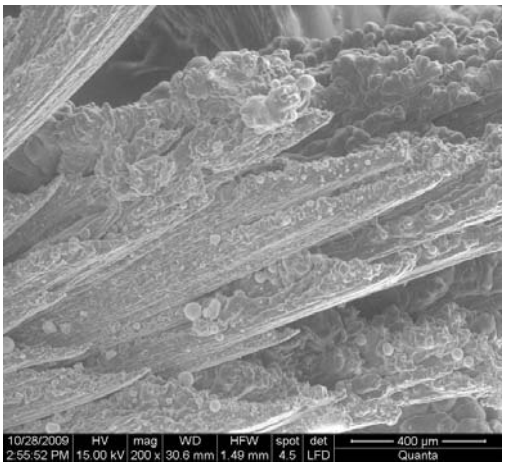

Wear particle obtained after dry sliding 10 km at v=1 m/s, p=1 MPa, pin-on-disk, disk made of composite with polyamide matrix and 20% micro glass spheres, pin made of steel

***Fig. 11.** SEM images of debris detached after pin-on-disk tests.*

The disadvantages are that it is a time-consuming investigation and special higher resolution coating techniques are required for high magnification imaging of either organic or inorganic thin films.

The images could reveal how a glass fiber is broken (Fig. 7a) or how the soft polymer such as PTFE is acting like a solid lubricant (Fig. 7b).

The symbol *p* is used for average pressure on contact.

Both optical and SEM microscopies allow studying the wear debris and the influence that some factors such as regime type, speed and load could influence their generation. SEM and optical images could be useful for estimating the size distribution of the adding materials, but the results are sensitive to the scale and the number of the analyzed images. For instance, Figure 12 presents two SEM images of micro glass spheres that will be added into a polyamide matrix. Using an appropriate soft, the images at a smaller scale could give a more accurate size distribution but a larger scale reveals the smaller particles and their size around several hundred nanometers.

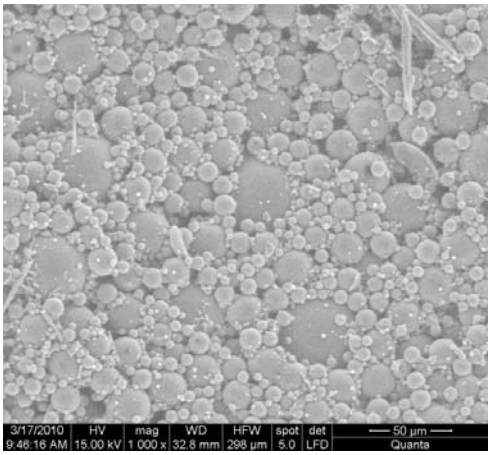

a)

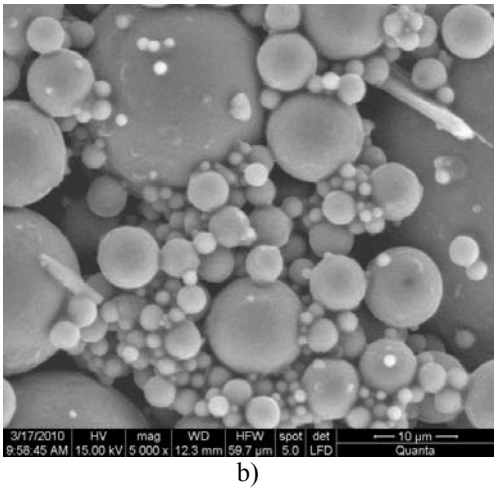

b)

***Fig. 12.** SEM images of the micro glass spheres, at different scale that could be used for evaluating the size dispersion.*

If the composite constituents are chemically non-reactive one to each other during the functioning of the tribosystem, the images could serve to evaluate the surface concentration of each one. For instance, in dry regime for the composite PTFE + 60% bronze, it was obtained a surface concentration of 15.7...21.5% PTFE. The bags of PTFE have the tendency to get longer in the sliding direction and the process of

polymer transfer is observed even on the composite (Fig. 7b) not only on the steel roller, in thin slices (light-grey colours); this process is favourable for reducing friction as presented in the model [5, 37]. After sliding in water, the surface percentage of PTFE on the tribolayer is 11.35...18.35% for the studied shoes, similar to the other shoes tested in water in open circuit at speed higher than 1m/s. For this composite, PTFE is captive and isolated in the metallic mass and this is the reason why the surface concentration on the tribolayer is not significantly changed. PTFE bags have the tendency to become spheres under the action of stress field, maybe with flat or cut zone on the surface. These spheres are smaller towards the surface as the tribolayer is locally compressed and fragmented (Fig. 13). In dry regime it was obtained a surface concentration of 15.7...21.5% PTFE.

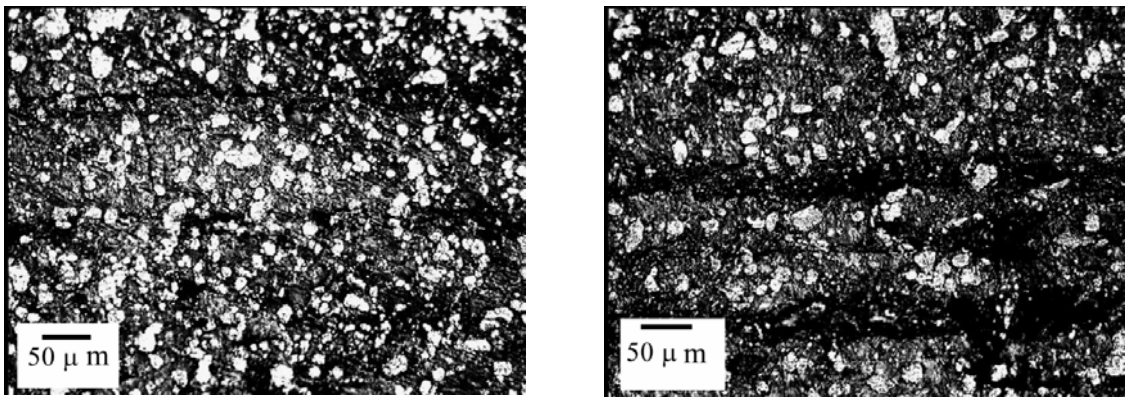

a) the highest concentration obtained for the shoe tested at 4 kN

b) the least concentration on the same shoe, obtained in the middle zone of the loaded zone

Fig. 13. *Surface of the composite PTFE + 60% bronze after sliding in water for 10,500 m at v=2.5 m/s and F=4 kN, test done on shoe ∅60 x 25 mm on steel shaft.*

3.3. X-ray diffractometry

X-ray diffraction techniques could do a characterization of crystalline materials, including polymers, and their composites, identifying the phases present in samples from raw materials to finished products and to provide information on the physical state of the sample, such as grain size, texture, and crystal perfection. Most X-ray diffraction techniques are rapid and nondestructive [20, 23]. By X-rays diffraction method, the structure and inner tension changes occurring in the superficial layer have been evinced.

Wide angle X-ray diffractometry provides information on the crystal structure and the orientation. Low angle X-ray scattering offers information on the size and regularity of lamellar crystals' packing but the interpretation is often a difficult matter [23]. A systematic study on the tribological behaviour of polymers and their composites is hard to achieve during testing; thus many results are dealing with the analysis of after-tests.

After dry friction, the X-ray investigation of the structural changes in the superficial layer of PTFE, the volume of the hexagonal cell was found to be reduced, the crystallites were found to be enlarged and residual stresses were found to be introduced as a result of this transition [21, 40]. Figure 14 present diffractograms in a range of 30…45 degrees for the angle 2θ as the most important structural changes of this polymer occur in this angle range [20, 41]. Diffracted X-rays are mono-chromatised before being detected, this leading to avoid background noise.

After friction under lubricated regime (water), the amorphous structure is more consistent. The fragmentation of the molecular chains of PTFE is pointed out by the appearance of new diffraction peaks. This is caused by mechanical processes as a consequence that water film is discontinuous.

The same cause also provokes a forced orientation of the fragmented micro-volumes and chains of the polymer within the superficial layer, pointed out by the increase of peaks' intensities. For v=1.5 m/s, within the superficial layer, the fragmentation of the molecular chains is diminished as compared to that for v=0.7m/s, but the noticed fragments have a more accentuated orientation. This could be explained by the fact that there are conditions to generate a more stable lubricant film and on a greater part of the contact area.

For the composites PTFE + glass fibers, the same types of structural modifications are noticed (fragmentation and forced orientation of the molecular chains of the polymer) but they are less intense, and the modifications diminish as the glass fiber concentration increases.

As pointed out in [5, 33, 37, 39], the glass fibers play the part of an unorganized net that does not allow

for a too intense fragmentation and orientation of the polymer matrix within the superficial layers, also reducing the wear with one order or even more [6, 19, 39].

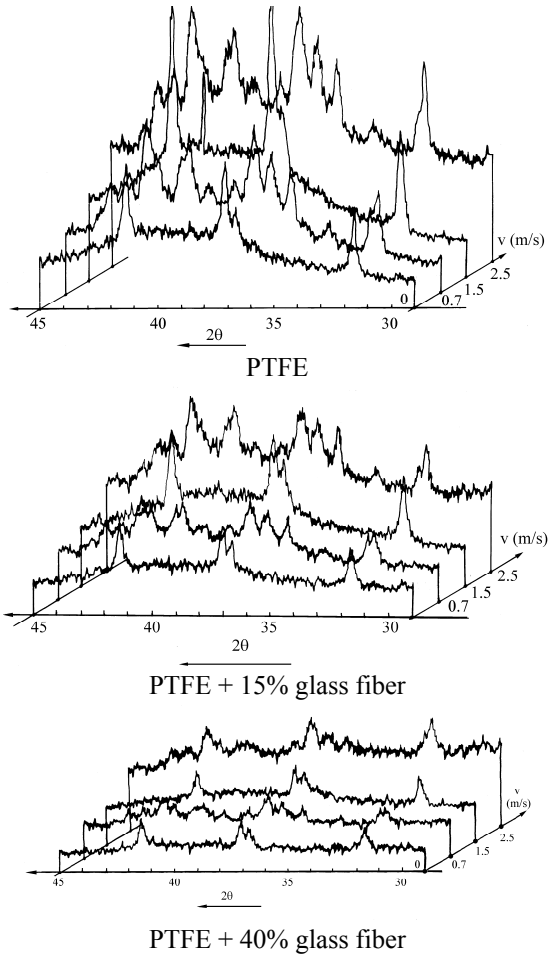

Fig. 14. *The parameters of the investigation were voltage U=34kV, current intensity I=30mA and there was investigated a range of 2θ between 25 and 45 degrees.*

After testing by sliding in water at constant speed and load, against steel, the new appeared structures in composites PTFE+ glass fiber are in a lower quantity as comparing to the pure PTFE sample. This change in the diffractograms may be explained as following:

- the presence of a smaller quantity of PTFE in the superficial layer due to adhesive or abrasive wear, supported especially by the polymeric matrix,
- the presence of glass fibers does not probably allow orientating the new structures.

Comparing after-testing diffractograms for PTFE +15% glass fiber to that for PTFE + 40% glass fiber, one may notice the presence of the same structures but lower fiber concentration. The PTFE peaks are very clear and the structure of the polymer is much more oriented as compared to the composites.

An increase of the peaks' heights for higher speeds may suggest a forced orientation of the polymer crystallites.

But for the highest value of sliding speed, the peak heights decrease and the basic level of the diffractograms is lifted, pointing out a decrease of the structure orientation and an increase of the amorphous phase. These aspects may be interpreted only making a correlation to wear values. The depth of the X-ray investigation is approximately 100…200 μm. If wear is considerable, the superficial layer investigated for extreme values of sliding speed is totally new, and very fragmented. It is important to point out that average pressure is not quite relevant for result interpretation.

It will be more useful to know the maximum contact pressure that could be several times greater than the average, closer to the flow limit of the polymer. For composites PTFE + glass fibers, the changes in diffractograms aspects are not so dramatic, suggesting that the fiber net makes the superficial layer more stable, including the structure orientation and the crystallinity degree. The higher level of the after-test diffractograms indicates the fragmentation of initial structures.

The appearance of new structural crystallites is not so evident for composites with higher fiber concentration.

Pointing out these aspects allows selecting the adding material related to their quality (fibers, powder, mechanical properties etc.) and their quantity in order to obtain a composite with a better tribological behaviour.

3.4. 3D profilometry

Due to modern softwares, the data recorded with the help of 3D contact or non-contact profilometers, make possible to calculate many roughness parameters [3, 42].

Comparing statistical data on these parameters, the tribologists could establish the surface quality after testing and the influence of several factors on the magnitude of parameters.

They are especially interested in studying the functional parameters (as given from the Abbot Firestone loading bearing area).

Virtual images as those in Figure 15 could be used for identifying the processes taking place into the superficial layers.

Figure 16 presents the influence of the micro glass spheres concentration on the amplitude parameters for two dry sliding regimes. The interpretation should be done carefully as the plots have a statistical character, and could be altered by the

number of measurements [12, 28]. In this figure, the plotted results are the average value from three measurements on 500 x 500 μm, equi-angularly on the wear track of the composite disk.

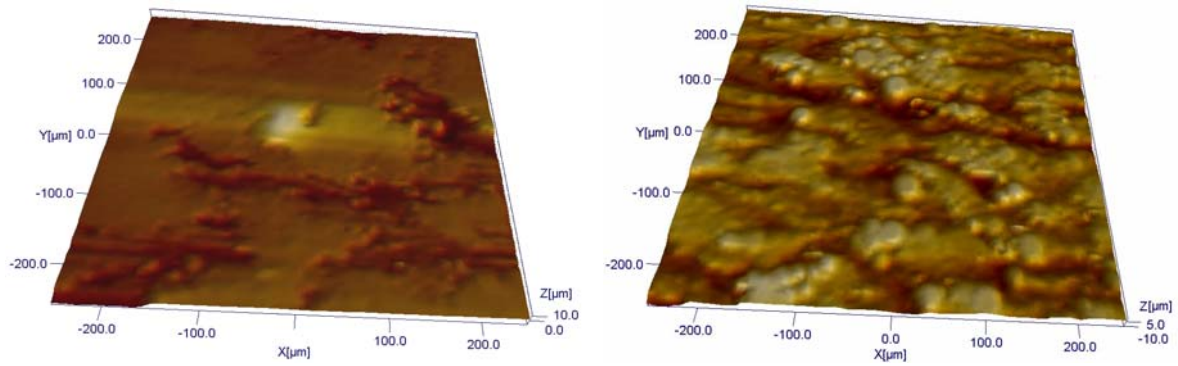

a) v=1 m/s, p=1 MPa *b) v=1.5 m/s, p=1 MPa*

Fig. 15. *Virtual images created from data obtained with the help of a dedicated soft [42] after data acquisition with the help of a 3D profilometer for the wear track on the composite with polyamide matrix and 50% micro glass spheres, after being tested under dry sliding (pin-on disk tribotester).*

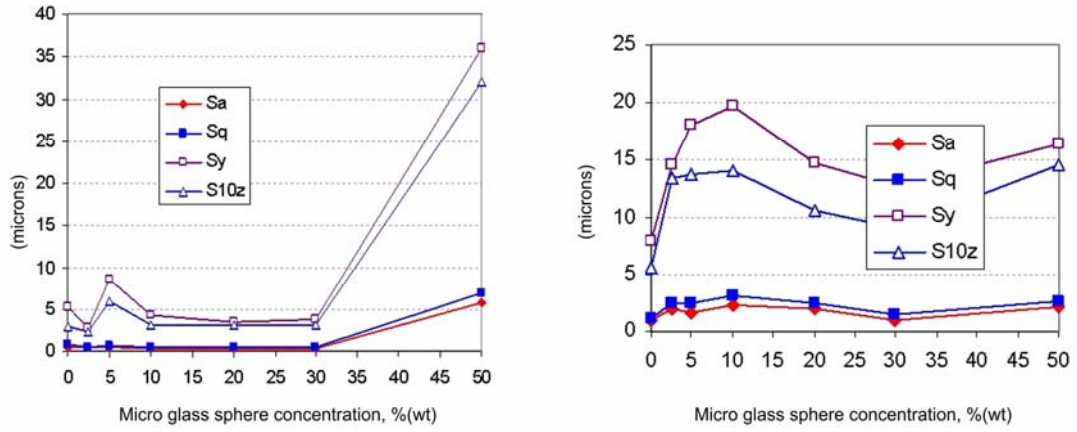

v = 0.5 m/s *v = 1.5 m/s*

Fig. 16. *Amplitude parameters as a function of concentration of micro glass spheres for two sliding speeds, at p=3 MPa (all symbols are defined in [3, 42]: Sa – roughness average, Sq – root mean square, Sy – the maximum height peak-valley, S10z – ten point heights.*

3.5. Thermal survey

This method of monitoring the contact during functioning is now easy to be done with the help of an accurate thermographic camera and a dedicated soft for obtaining the temperature evolution in time on different zones of the triboelements „exposed" to the camera.

Figure 17 presents a thermographic survey of a pin-on-disk contact for a composite PA+ micro glass sphere revealing that thermal field and the friction coefficient are interconnected.

Using analytical or numerical methods and knowing the temperature at the contact edge, one may calculate the maximum temperature in contact.

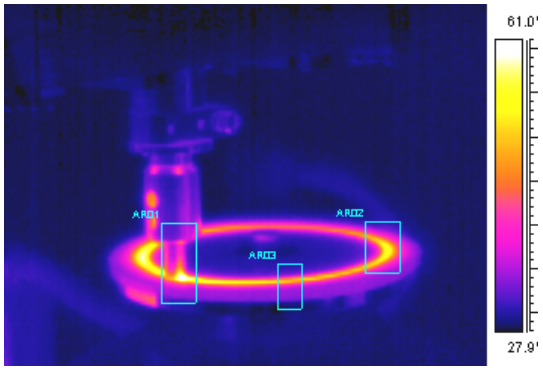

Fig. 17. *Points for temperature survey for a pin-on-disk test for a disk made of polyamide and pin made of steel.*

The temperature is very important for the polymeric composite [2, 5, 37], allowing a decrease of the friction coefficient when the temperature is high enough to generate a very thin viscous or melt polymer film. The monitoring of the temperature field was done with the help of a thermographic camera. Figure 18 gives the temperature evolution for three points on the pin-on-disk tribotester: AR01 – for the contact between pin and disk, AR02 – 90 degrees in back of the contact, on the wear track, AR03 – a point diameterlly opposed to the contact. Studying the friction coefficient one may notice that peaks of temperature evolution are accompanied by rises in the friction coefficient, meaning a change of the regime conditions.

A possible explanation is: a high temperature softens the polymer and for a time period, this viscous material help reducing the friction coefficient value and the process is dynamically repeated, with different time durations.

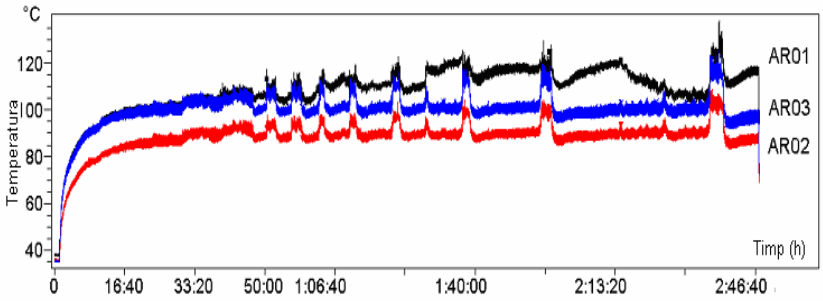

Fig. 18. *Temperature recorded in three points on the wear track of the disk made of composite with polyamide matrix and 20% micro glass spheres at v=1 m/s, p=1 MPa [28].*

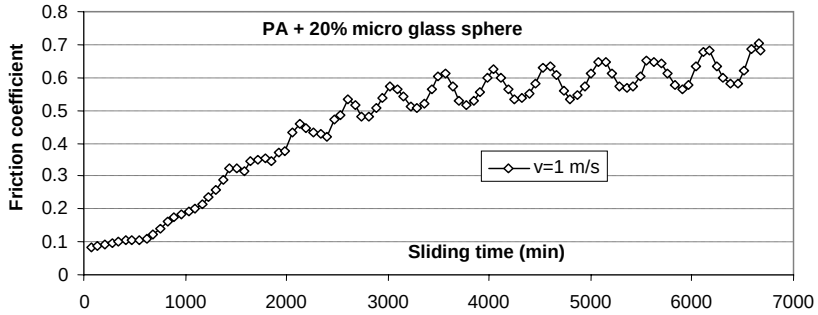

Fig. 19. *Evolution in time of the friction coefficient for the same test conditions as those in Figure 18 [28].*

4. Conclusion

The investigation of the superficial layers of the polymeric composites has to use several methods (some of them being exemplified in this paper) in order to identify the processes and the influencing factors.

Of course there are other investigation techniques that were not mentioned there (AFM microscopy, spectrometry etc.).

Specialists have to design the adequate set of investigation techniques, that could reveal the relevant processes for tribological applications.

References

[1]. **Becker W.T., Shipley R. J.** (editors) - *Failure Analysis and Prevention,* Volume 11, ASM International, 2002.

[2]. ***Bhushan B.*** - Micro/Nano Tribology*, Washington, D.C., USA, 1998.*

[3]. **Blunt De L., Jiang X. -** *Advanced techniques for assessment surface topography development of a basis for 3D surface texture standards "surfstand"*, London, Sterling, VA, Kogan Page Science, Elsevier, 2003.

[4]. **Bos J., Moes H.** - *Frictional Heating of Tribological Contacts*, Journal of Tribology, 117, pp. 171-177, 1995.

[5]. **Briscoe B.J., Sinha S.K.** - *Tribology of Polymeric Solids and Their Composites*, Stachowiack G. W. (editor), in *Wear – Materials, Mechanisms and Practice*, John Wiley & Sons Ltd, pp. 223-268, 2005.

[6]. **Burris D.L., Sawyer W.G.** - *Improved wear resistance in alumina-PTFE nano-composites with irregular shaped nanoparticles*, Wear, 260, pp. 915–918, 2006.
[7]. ***Cahn R.W., Haasen P., Kramer E.J.*** - Structure and Properties of Polymers*, vol. 12, Weinheim, 1993.*
[8]. **Chen Y.K., Kukureka S.N., Hooke C.J., Rao M.** - *Surface topography and wear mechanisms in polyamide 66 and its composites*, Journal of Materials Science, 35, pp. 1269-1281, 2000.
[9]. **Cho M.H., Bahadur S., Anderegg J.W.** - *Design of experiments approach to the study of tribological performance of Cu concentrate-filled PPS composites*, Tribology International, 39, pp. 1436-1446, 2006.
[10]. **Czikos H.** - *Tribology – A System Approach to the Science and Technology of Friction, Lubrication and Wear*, Elsevier Scientific Publishing Company, New-York, pp 73-81, 1978.
[11]. **Deleanu L., Andrei G., Başa A., Chiculiţă S., Cantaragiu A.** - *Tribological Behaviour of composites with PTFE matrix when sliding in water*, Journal of the Balkan Tribological Association Vol. 16, Tribomechanics, No 2, **ISSN** 13104772, pp. 180-188, 2010.
[12]. **Deleanu L., Andrei G., Maftei L.** - *Surface Characterization of Polymer Composite Using Bearing Area Curve*, Proceedings of the ASME 2010 10th Biennial Conf. on Engineering Systems Design and Analysis, ESDA 2010, July 12-14, 2010, Istanbul, Turkey, paper ESDA2010-25330, 2010.
[13]. **Deleanu L., Gabriel A., Bîrsan I.G., Răileanu I.** - *Particular aspects of tribological behaviour for composites with polyamide matrix and micro glass spheres*, 3rd European Conference on Tribology, Ecotrib 2011 and 4th Vienna International Conference on nano-Technology, Viennano'11, pp. 213-218, 2011
[14]. **Deleanu L., Maftei L., Andrei G.** - *Friction coefficient in dry regime for steel pin sliding on PA composites with micro glass spheres*, Intern. Conf. "Advances in Engineering and Management", University of Craiova, Faculty of Engineering and Management of Technological Systems, 19-21 May, Drobeta Turnu Severin, Romania, 2010.
[15]. **Endo H., Marui E.** - *Fundamental studies on friction and wear of engineering plastics*, Industrial Lubrication and Tribology, 56, no. 5, pp. 283-287, 2004.
[16]. **Friederich K., Schlarb A. K.** - *Tribology of Polymeric Nanocomposites*, Elsevier, pp. 403-438, 2008.
[17]. **Friedrich K.** - *Wear models for multi phases materials and synergic effects in polymeric hybrid composites*, in Advances in Composite Tribology, ed. Friedrich K., Elsevier, Amsterdam, 1993.
[18]. **Friedrich K., Zhang Z., Klein P.** - *Wear of Polymer Composites*, Stachowiack G. W. (editor), in *Wear – Materials, Mechanisms and Practice*, John Wiley & Sons Ltd, pp. 269-290, 2005.
[19]. **Friedrich K., Zhang Z., Schlarb A. K.** - *Effects of various fillers on the sliding wear of polymer composites*, Composites Science and Technology, 65, pp. 2329–2343, 2005.
[20]. ***Gheorghieş C.*** - Modificări structurale în procese de uzură şi oboseală *(*Structural changes characterising the wear and fatigue processes - *in Romanian), Editura Tehnică, Bucureşti, 1994.*
[21]. ***Gong D., Xue Q., Wang H.*** - ESCA Study on tribochemical characteristics of filled PTFE*, Wear, 148, pp. 161-169, 1991.*
[22]. **Haixia H., Sirong Y., Yaohui L., Yi L., Kaixin L.** - *Tribological Behavior of Polyamide 66-Based Ternary Nanocomposites Modified with Organoclay and SEBS-g-MA*, Tribology Letters, 32, pp. 23–29, 2008.
[23]. **Jenkins R.** - *Encyclopedia of American Chemistry, X-ray techniques: Overview*, John Wiley and Sons Ltd. Chicheste, pp. 13269-13288, 2000.
[24]. **Jia B.B., Li T.S., Liu X.J., Cong P.H.** - *Tribological behaviors of several polymer-polymer sliding combinations under dry friction and oil-lubricated conditions*, Wear, 262, pp. 1353-1359, 2007.
[25]. **Kato K.** - *Classification of Wear Mechanisms / Models*, Stachowiak G. W. (editor), *Wear – Materials, Mechanisms and Practice*, John Wiley & Sons Ltd, pp. 9-20, 2005
[26]. **Larsen T., Andersen T.L., Thorning B., Horsewell A., Vigild M.E.** - *Changes in tribological behavior of an epoxy resin by incorporating CuO nanoparticles and PTFE microparticles*, Wear, vol. 265, no1-2, pp. 203-213, 2008.
[27]. **Liu W., Huang C., Gao L., Wang J., Dang H.** - *Study of the friction and wear properties of MoS_2-filled nylon-6*, Wear, 151, pp. 111-118, 1991.
[28]. **Maftei L.** - *Contributions on Studying the Tribology of Composites with Polyamide and Micro Glass Spheres*, PhD Thesis (in Romanian), University "Dunarea de Jos" of Galati, 2010.
[29]. **McCook N.L., Hamilton M.A., Burris D.L., Sawyer W.G.** - *Tribological results of PEEK nanocomposites in dry sliding against 440C in various gas environments*, Wear, 262, pp. 1511–1515, 2007.
[30]. **Mimaroglu A., Unal H., T. Arda T.** - *Friction and wear performance of pure and glass fibre reinforced polyetherimide on polymer and steel counterface materials*, Wear, 262, 1407-1413, 2007.
[31]. **Mimaroglu A., Sen U., Unal H.** - *Abrasive Wear Volume Maps for PA6 and PA6 Composites Under Dry Working Condition*, Appl Compos Mater, 15, 13–25, 2008.
[32]. **Palabiyik M., Bahadur S.** - *Tribological studies of polyamide 6 and high-density polyethylene blends filled with PTFE and copper oxide and reinforced with short glass fibers*, Wear, 253, pp. 369–376, 2002.
[33]. **Sawyer G. W., Freudenberg K.D., Bhimaraj P., Schadler L.S.** - *A study on the friction and wear behavior of PTFE filled with alumina nano-particles*, Wear, 254, pp. 573–580, 2003.
[34]. **Sinha K.S., Briscoe J.B.** (editors) - *Polymer tribology*, Imperial College Press, UK, pp 38-71, pp 416-446, 2009.
[35]. **Srinath G., Gnanamoorthy R.** - *Effect of nanoclay reinforcement on tensile and tribo behaviour of Nylon 6*, Journal of Material Science, 40, pp 2897–2901, 2005.
[36]. **Srinath G., Gnanamoorthy R.** - *Effect of Short Fibre Reinforcement on the Friction and Wear Behaviour of Nylon 66*, Applied Composite Materials, 12, pp. 369-383, 2005.
[37]. **Stachowiak G.W.** *Wear - Materials, Mechanisms and Practice*, John Wiley & Sons, Ltd, pp 15-18, pp 269-286, 2006.
[38]. **Tanaka A., Umeda K., Takatsu S.** - *Friction and wear of diamond-containing polyimide composites in water and air*, Wear, 257, pp. 1096–1102, 2004.
[39]. ***Tomescu (Deleanu) L.*** - Contribution to study the superficial layers of the composites with PTFE matrix, using laboratory sliding tribosystems*, PhD, University "Dunarea de Jos" Galati, Romania, 1999.*
[40]. **Vijaian K., Biswas S.K.** - *Wear of polytetrafluorethylene: some crystallographic observations*, Wear, 150, pp 267, 1991.
[41]. **Whan R.E.** (volume coordinator) - *Volume 10, Material Characterization, ASM handbook*, Fifth printing, March 1998.
[42]. ***** *The Scanning Probe Image Processor SPIP*™, Version 4.7, 2008.

THE ANNALS OF "DUNAREA DE JOS" UNIVERSITY OF GALATI.
FASCICLE IX. METALLURGY AND MATERIALS SCIENCE
N^0. 4 – 2011, ISSN 1453 – 083X

EFFECT OF ACIDIC ENVIRONMENT ON Cu-Al_2O_3 CODEPOSITION*

Mihaela-Daniela GAVRIL (DONOSE)[1], Constantin GHEORGHIEŞ[2], Alina-Mihaela CANTARAGIU[1], Denys Cristina VLADU (RADU)[1], Sorin DONOSE[3]

[1]PhD students Faculty of Sciences and Environment, „Dunarea de Jos" University of Galati
[2]Faculty of Sciences and Environment, Chemistry, Physics and Environment Department, „Dunarea de Jos" University of Galati
[3]41 "Grigore Teologul" School, Galati

ABSTRACT

Electrocodeposition of alumina nanoparticles with copper onto nickel substrate was prepared through the potentiostatic method. The codeposited films were obtained at different nanoparticle concentrations: 5, 10, 15, 20 and 25 gL^{-1}. The corrosion behaviour of codeposited films has been observed by introducing them in different corrosive environments: 0.5 M H_2SO_4, HCl and HNO_3 solutions. The corrosion study has been realized using the linear polarization method. The corrosion rate and polarisation resistance values were obtained from the Tafel curves. The highest concentration of alumina nanoparticles had increased the corrosion resistance of Cu-Al_2O_3 codeposited films. Also, in order to confirm these results, the gravimetric parameter was calculated by means of the mass loss method.

KEYWORDS: electrocodeposition, cooper, alumina, corrosion, Tafel curves

1. Introduction

There are several methods and techniques for protecting the surface of metallic materials against the aggressive action of environment [1]. The alumina coatings have a protective function, being a physical barrier between the metal surface and the aggressive environment [2].

The corrosive process study is very important to prevent and control this spontaneous phenomenon. The corrosion study has been realized using the linear polarization method and performed in three different acid environments: 0.5 M H_2SO_4, HCl, and HNO_3 solutions.

The electrocodeposited films of the alumina nanoparticles with copper matrix on nickel substrate were obtained at different nanoparticle concentrations: 5, 10, 15, 20 and 25 gL^{-1} by means of the chronoamperometric method.

This paper presents the synthesis of the Cu-Al_2O_3 nanocomposite films by means of the potentiostatic electrochemical method and the corrosion behaviour is evaluated through the comparative analysis of the corrosion resistance values obtained for solid samples.

Some results concerning the behaviour into corrosive environment of nickel samples coated with Cu-Al_2O_3 films are reported [1].

2. Materials and methods

Copper films have been electrodeposited onto nickel substrate from an electrolyte solution having the following composition: 0.8 M $CuSO_4 \times 5H_2O$, 0.55 M H_2SO_4, 0.003 M HCl diluted in 100 mL volume solution [3]. A three electrode system with an electrochemical cell volume of 100 ml was used to perform the experiments.

*Paper presented at the Symposium ***"The Impact of Nanotechnologies and Nanomaterials on Industrial Development and Quality of Life",*** Galati, May 19, 2011, organized by the Center for Nanostructures and Functional Materials (CNMF), Faculty of Metallurgy, Materials Sciences and Environment, "Dunarea de Jos" University of Galati

The counter electrode was a platinum sheet and the reference electrode was an Ag/AgCl.

The working electrode was the nickel substrate which has an electroactive area of 2.5 cm^2.

Before each experiment, the working electrode was mechanically polished with abrasive silicon carbide paper, degreased in acetone and alcohol, etched with 1:10 HNO_3:H_2O, rinsed with distilled water and then, dried in air.

The process will occur without magnetic stirring. The electrolyte pH was recorded by means of the Consort C931 equipment.

The temperature was controlled with a thermostat. Also, before and after codeposition the samples, weight was measured using an electronic balance (model ESJ200-4).

The coatings preparation was carried out potentiostatically with a potentiostat/galvanostat VoltaLab10 interfaced with VoltaMaster4 software for data acquisition and analysis. After deposition, the samples were rinsed with bidistilled water to remove loosely adherent nanoparticles.

The composite coatings consisting of Al_2O_3 nanoparticles in a copper matrix have been electrocodeposited onto nickel substrate during 30 min. as deposition time at 50°C and pH of 1.7 [4]. Five different Al_2O_3 particle concentrations were used to obtain the composite films (5 , 10, 15, 20 and 25 gL^{-1}). The process starts at 450 rpm as stirring rate.

The corrosion behaviour was carried out with a VoltaLab10 potentiostat. Potentiodynamic polarisation curves of the codeposited films were measured from -1000 mV toward the anodic direction of 1000 mV with a scan rate of 50 mV/s. The corrosion behaviour of codeposited films has been observed by introducing them in different corrosive environments: 0.5 M H_2SO_4, HCl and HNO_3 solutions. The exposure corrosion time is 60 s.

The linear polarisation (Tafel curves) was used as method to study the corrosion behaviour. From the anodic and cathodic polarization potentiodynamic curves were obtained the main electrochemical parameters of the corrosion process: corrosion potential E_{corr}, corrosion current density i_{corr}, polarization resistance R_p and corrosion rate V_{corr}.

The corrosion rate is automatically calculated by specialized computer software using the Randles-Sevcik equation (1). Before and after each experiment, the weight of samples was measured by means of analytical balance. The mass losses (difference between the final and initial weight) are calculated by means of the gravimetric method and showed in Table 1. Also, the penetration index was calculated.

3. Results and discussion

The corrosion rates (Table 1) determination was achieved by means of the "mass loss method" [5] in static regime at room temperature and it is calculated based on the equation (1):

$$V_{corr} = \frac{\Delta m}{S \cdot t} \quad (1)$$

where: V_{corr} = gravimetric index [g/m^{2}s^1]; Δm = weight loss (before and after the corrosion test) by corrosion [g]; S = corroded surface area [m^2]; t = corrosion time [s]. The average depth of the composite corrosive destruction is calculated using the formula (2):

$$p = \frac{V_{corr}}{\rho} \cdot 8.76 \quad (2)$$

where: p = penetration index [mm/y]; V_{corr} = gravimetric index [g/m^{2}s]; ρ = composite film density [g/cm^3]. The results are presented in Table 1.

Table 1. *The Cu-Al_2O_3 electrocodeposition behaviour in various acid environments by means of the gravimetric method*

Acid	Al2O3 Conc. (g/l)	Weight difference (g)	v cor (g/m2s)	Penetration index (mm/y)	Δm (g)
	5	0.0044	0.924	0.63	0,6578
	10	0.0032	0.762	0.52	-0,0032
H_2SO_4	15	0.0015	0.325	0.22	-0,0015
	20	0.0031	0.651	0.44	-0,0031
	25	0.0030	0.630	0.43	-0,003
	5	0.0004	0.075	0.05	-0,0004
	10	0.0005	0.105	0.07	-0,0005
HCl	15	0.0008	0.147	0.1	-0,0008
	20	0.0008	0.196	0.13	-0,0008
	25	0.0008	0.168	0.11	-0,0008
	5	0.0008	0.196	0.13	-0,0008
	10	0.0039	0.382	0.26	-0,0039
HNO_3	15	0.0017	0.167	0.11	-0,0017
	20	0.0018	0.176	0.11	-0,0018
	25	0.0018	0.331	0.22	-0,0018

The results from Table 1 are indicated that the less aggressive environment is the HCl against the nanocomposite Cu-Al_2O_3 (5 gL^{-1}).

On the other hand, the codeposited films are highly corroded in the H_2SO_4 solution.

Fig. 1 shows the influence of the alumina nanoparticle concentrations on the composites corrosion rate measured during the polarisation studies. These data show that the Cu-Al_2O_3 codeposition has a real protection effect.

The Al_2O_3 nanoparticle concentrations increasing lead to the significant decrease of the corrosion rate in each acid environment. 15 gL^{-1} Al_2O_3 nanoparticles present the higher corrosion rate in HNO_3 and the nanocomposites with 5, respectively 25gL^{-1} are more resistant to corrosion.

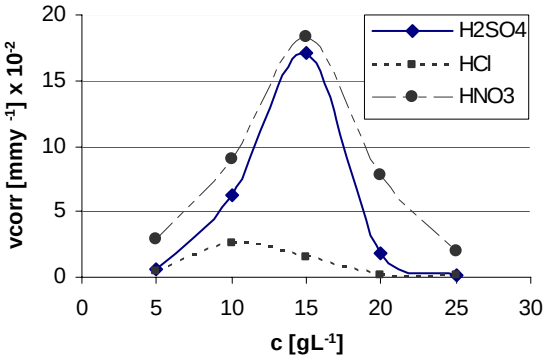

***Fig. 1**. The corrosion rate variation with the Al_2O_3 nanoparticle concentrations.*

In this case, the corrosion rate values are automatically calculated by the VoltaMaster4 software [6] based on the equation (3):

$$V_{corr} = \frac{0.051 \cdot i_{corr}}{\rho \cdot A} \qquad (3)$$

and according to the Stearn-Geary equation (4) [6,7]:

$$R_p = \left[\frac{1}{2.303 \cdot i_{corr}}\right] \cdot \left[\frac{\beta_a \cdot \beta_c}{\beta_a + \beta_c}\right] \qquad (4)$$

where: V_{corr} = corrosion rate [mm/y]; i_{corr} = corrosion current density [A/dm^2]; A = composite molecular weight [g/mol]; ρ = composite film density [g/cm^3]; R_p = polarisation resistance [Ωcm^2]; β_a = anodic Tafel slope [mV]; β_c = cathodic Tafel slope [mV].

The most aggressive environments are the 0.5M H_2SO_4 and HNO_3 solutions for which are recorded the highest corrosion values. Namely, the composites Cu-Al_2O_3 with 15 gL^{-1} nanoparticle concentrations are exposed to a very aggressive corrosion into acid environment. In the presence of 0.5 M HCl solution, almost all samples have a good behaviour by surface passivation process.

The effect of Al_2O_3 nanoparticle concentrations on the composite layer thickness was studied. The layer thickness was calculated using the formula (5):

$$d = \frac{\Delta m}{S \cdot \rho} \cdot 10^4 \qquad (5)$$

where: d = thickness [μm]; Δm = weight difference [g]; S = surface area [cm^2]; ρ = composite density [g/cm^3].

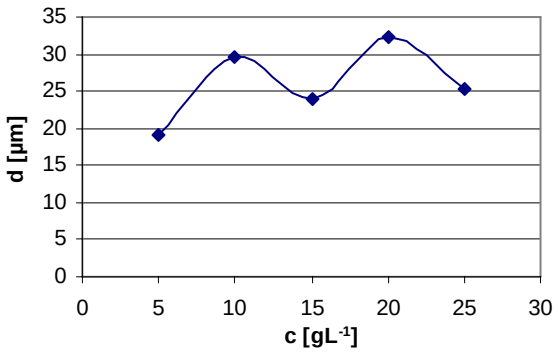

***Fig. 2.** The layer thickness variation with the Al_2O_3 nanoparticle concentrations.*

The layer thickness shows a non-linear increased tendency when increasing the Al_2O_3 nanoparticle concentrations due to the stirring effect on the electrolyte solutions. The degree of alumina nanoparticles included in copper matrix increases when increasing the nanoparticle concentrations. Thereby, the thickness has varied with concentration and the high values of thickness correspond to 10 and 20 gL^{-1} nanoparticles in electrolyte.

The composites were carefully cleaned and rinsed with bidistilled water before their immersion in the electrochemical cell with acid solution. Each measurement started after 60 s to access an equilibrium potential between composite films and acid solution, because of electronic interactions at the interface [7, 8, 9]. The point of intersection between the anodic and cathodic reactions establishes the corrosion potential (E_{corr}) of the composites and indicates the magnitude of the corrosion current (i_{corr}). The corrosion process at Cu-Al_2O_3 composite films surface was studied by means of the linear polarisation method [6].

Fig. 3-5 present the electrochemical behaviour of Cu-Al_2O_3 composite films tested in three acid environments. Fig. 3 shows the polarization curves in case of Cu-Al_2O_3 composite films immersed in 0.5M H_2SO_4 solution. The E_{corr} potential was shifted to high negative values when increasing nanoparticle concentrations.

The Cu-Al_2O_3 composite with 25 gL^{-1} has the most negative E_{corr} value potential, thus confirming the highest corrosion rate value. This fact can be due to the poor inclusion ability of alumina nanoparticles into a metallic matrix when the concentration is higher. More corrosion resistant could be Cu-Al_2O_3 composite film with 5 gL^{-1} nanoparticle concentrations. All cathodic branches are linearly shaped (no surfaces passivated) and the composite surfaces are more susceptible in the H_2SO_4 electrochemical solution.

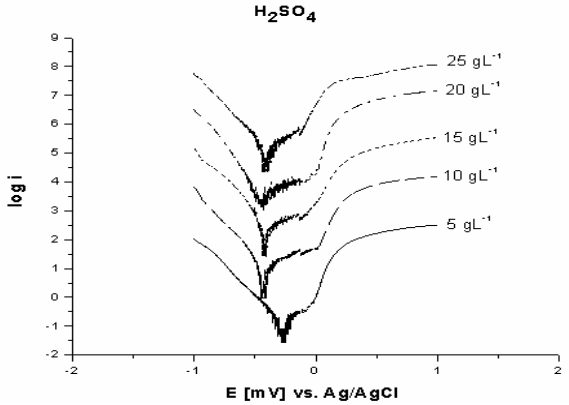

Fig. 3. *Tafel polarisation curves of Cu-Al_2O_3 composite films in 0.5 M H_2SO_4 environment.*

Fig. 4 shows the polarization curves in case of Cu-Al_2O_3 composite films immersed in 0.5 M HCl solution. The E_{corr} potential was shifted to less negative values (compared to the first corrosion test) when increasing nanoparticle concentrations [6].

The Cu-Al_2O_3 composite with 15 gL^{-1} has the most negative E_{corr} value potential, thus confirming the highest corrosion rate value. This fact can be due to the poor inclusion ability of alumina nanoparticles into a metallic matrix when the concentration increases. More corrosion resistant could be the Cu-Al_2O_3 composite film with 5 gL^{-1} nanoparticle concentrations due to the surface passivation process. However, all sample surfaces, are not stable in this solution due to the non-linear shape of the cathodic and anodic branches.

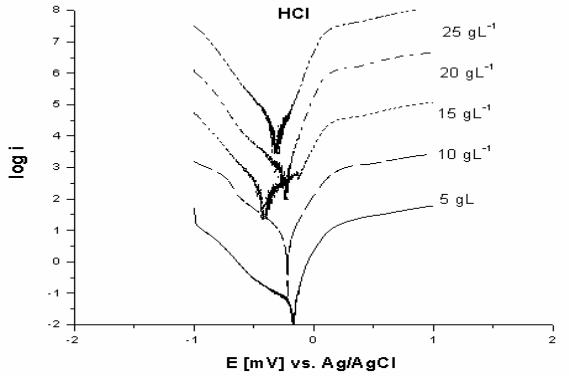

Fig. 4. *Tafel polarisation curves of Cu-Al_2O_3 composite films in 0.5 M HCl environment.*

Fig. 5 shows the polarization curves in case of Cu-Al_2O_3 composite films immersed in 0.5 M HNO_3 solution. The E_{corr} potential was shifted to most negative values.

The Cu-Al_2O_3 composite with 25 gL^{-1} has the most negative E_{corr} value potential, thus confirming the highest corrosion rate value. The cathodic branch appears linearly shape for 25 gL^{-1} nanoparticle concentrations, so there is no passivity reaction [6].

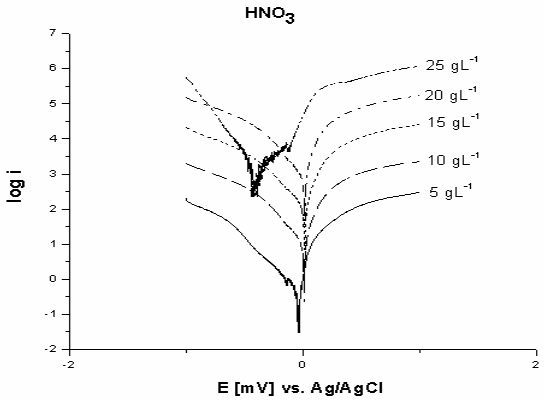

Fig. 5. *Tafel polarisation curves of Cu-Al_2O_3 composite films in 0.5 M HNO_3 environment.*

However, for the other concentration, the cathodic branches are non-linear due to the oxide layer formation. The most corrosion resistant could be the Cu-Al_2O_3 composite film with 5, 10, 15 and 20 gL^{-1} nanoparticle concentrations due to the surface passivation process (E_{corr} is shifted to zero value). The decreasing of nanoparticle concentrations in the electrolyte increases the electrochemical passivation from cathodic and anodic polarisation curves. This behaviour can be explained on the basis of the inert action of this environment against samples.

4. Conclusions

From the obtained results of the polarization measurement method (Tafel curves) of the Cu-Al_2O_3 composite films exposed to various acid environments it may be concluded that:

- Nanocomposite thin films which consist of Al_2O_3 nanoparticles in a copper metal matrix were deposited on a nickel substrate and synthesized using the electrocodeposition method.
- The corrosion process and electrochemical parameters depend on some factors: electrolyte type, exposure time, pH value, chemical composition of working electrode, applied scanning potential, nanoparticle concentrations and particles size.
- The increasing of Al_2O_3 nanoparticle concentrations led to the increasing corrosion resistance.

- The highest corrosive rate corresponds to H_2SO_4 atmospheres (for 25 gL^{-1} Al_2O_3).
- The 0.5 M HNO_3 solution is the least corrosive environment because this environment can limit the corrosion process by hydrogen ions evolution inhibition.
- The presence of Al_2O_3 nanoparticles led to quickly passivation into the 0.5 M HCl environment.
- The thickness layer increases non-linearly with the nanoparticle concentrations. The largest thickness corresponds to 20 gL^{-1} Al_2O_3.
- The destructive action shown in these experiments could be determined by the chemical reactions occurred as a result of electric currents passing through the liquid environment.

Acknowledgments

The work of Mihaela-Daniela Gavril (Donose) was supported by Project SOP HRD - TOP ACADEMIC 76822.

References

[1]. A. Vicenzo and P.L. Cavallotti - *Copper electrodeposition from a pH 3 sulfate electrolyte*, J. Appl. Electroch., 32: 743–753, 2002.

[2]. M. Palaniappa, M. Jayalakshmi, P. M. Prasad, K. Balasubramanian - *Chronopotentiometric studies on the passivation of industrial copper anode at varying current densities and electrolyte concentrations*, Int. J. Electrochem. Sci., 3, 452–461, 2008.

[3]. D. Grujicic and B. Pesic - *Electrodeposition of copper: the nucleation mechanisms,* Electrochimica Acta, 47, 2901-2912, 2002.

[4]. Z. Anđić, M. Korać, M. Tasić, Ž. Kamberović, K. Raić, *Synthesis and Sintering of Cu-Al_2O_3 Nanocomposite Powders Produced by a Thermochemical Route*, Metalurgija Journal of Metallurgy, 13(1), 71-81, 2007.

[5]. D. Popovici, E. Trimbitasu, O. Pantea, D. Bombos, L. Antonescu - *Determinarea eficientei inhibitorului de coroziune Aticamina OTM 2*, Buletinul Universităţii Petrol-Gaze din Ploieşti, LIV, Seria Tehnică, 4, 189-196, 2002.

[6]. A. M. Cantaragiu, G. Carac, C. Gheorghies - *Electrochemical study of AISI 316L Stainless Steel in different nanoparticle suspensions*, J. Optoel. Adv. Mater., 12(20), 12, 2391-2399, 2010, ISSN: 1454-4164.

[7]. W. Stephen Tait - *Ph.D. An introduction to electrochemical corrosion testing for practicing engineers and scientists*, Pair O Docs Pubns, ISBN 9780966020700, 1994.

[8]. H. Davy - *On some chemical agencies of electricity (Bakerian Lecture of 1807)*, Phil. Trans. Roy. Soc. (London), 97, 56, 1807.

[9]. K. Babic-Samardzija, K. F. Khaled and N. Hackerman - *heterocyclic amines and derivatives as corrosion inhibitors for iron in perchloric acid*, Anti-Corrosion Methods and Materials 52(1), 11-21, 2005.

[10]. VoltaMaster 4 - *Application Help Handbook*; www.radiometer-analytical.com/voltalab/en_ocp.asp.

[11]. M. Stoica, G. Cârâc, C. Apetrei, A.M. Cantaragiu - *Electrochemical study of stainless steel surfaces in biodegradable biocides,* J. Optoel. Adv. Mater., 12(35), 4, 919-922, 2010.

THE ANNALS OF "DUNAREA DE JOS" UNIVERSITY OF GALATI.
FASCICLE IX. METALLURGY AND MATERIALS SCIENCE
N^0. 4 – 2011, ISSN 1453 – 083X

MONITORING TECHNIQUES FOR INORGANIC AND ORGANIC POLLUTANTS IN SOILS AROUND AN INTEGRATED IRON AND STEEL PLANT*

Antoaneta ENE[1], Alina (BOSNEAGA) SION[1], Lucian P. GEORGESCU[1], Oleg BOGDEVICH[2]

[1]"Dunarea de Jos" University of Galati, Faculty of Sciences and Environment, Department of Chemistry, Physics and Environment, Romania
[2] Institute of Geology and Seismology, Laboratory of Geochemistry, Moldova

ABSTRACT

In this paper the analytical techniques of X-Ray Fluorescence (XRF) and Gas Chromatography with Electron Capture Detection (GC-ECD) and coupled with Mass Spectrometry (GC-MS) are used in order to assess the level of industrial and agricultural pollution of soils. The soil samples were collected from Galati County, near an industrial plant and near cultivated areas. In this study, it is investigated the way in which the anthropic activities influence the quality of the environment, due to the contribution of inorganic and organic elements enrichments.

KEYWORDS: XRF, GC-ECD, GC-MS, organic and inorganic pollutants, soil pollution

1. Introduction

The extent of anthropogenic environmental pollution did affect the quality of the environment, and also the human life. Polycyclic aromatic hydrocarbons, commonly referred to as PAHs, are classified as organic compounds of two or more fused aromatic rings of carbon and hydrogen [1].

One of the most important sources of PAHs is the incomplete and/or inefficient combustion of fossil fuels. The steel production is involving either the refining of molten iron made from ore or the refining of recycled scrap steel. The first way is involving a high consumption of energy, by burning fossil fuels, being a contributor to PAHs discharge into the environment.

The second way of production is more electric furnace dependent, discharging a much smaller amount of PAH into the environment [1].

In other studies, there have been used zucchini (*Cucurbita pepo L.*) and spinach (*Spinacia oleracea*) as bioaccumulators for persistent organic pollutants (POPs) and heavy metals [2].

The potential for negative impacts of these elements and compounds on humans and the environment is of major concern. The aim of this work is the determination of some heavy metals and POPs in soils from selected regions in Romania using the analytical techniques of X-Ray Fluorescence (XRF) and Gas Chromatography with electron capture detection (GC-ECD) and coupled with Mass Spectrometry (GC-MS).

2. Experimental results

2.1. Sample collection

Six representative locations were chosen for sample collection of the soils, in Galati and Constanta counties, Romania, including industrial suburban and rural zones. Usually the texture of the soil samples was a mixture of sand and clays. The soil was collected with proper instruments, labelled and stored before sample preparation and analysis. The samples were collected from different depths according to the characteristics of the sample locations presented in Table 1.

*Paper presented at the Symposium ***"The Impact of Nanotechnologies and Nanomaterials on Industrial Development and Quality of Life",*** Galati, May 19, 2011, organized by the Center for Nanostructures and Functional Materials (CNMF), Faculty of Metallurgy, Materials Sciences and Environment, "Dunarea de Jos" University of Galati

Table 1. *Characteristics of the sample locations*

Sample No.	Depth (cm)	Sample location (global position)		Other characteristics
		N:	W:	
1	5 20	45°56′23.14″	28^{0}06′54.91″	Oancea commune, Galati county, close to a cultivated zone, at 0.01 km from the Prut River
2	5 15	45°44′36. 3″	28^{0}04′37.73″	Foltesti commune, Galati county, near a stable, and a cultivated area, at 5.99 km from the Prut River and at 35 km from the industrial plant
3	5 30	44°5′56.5″	27°25′48.3″	Bugeac village, Ostrov commune, South of Romania (Dobruja region), Constanta county, unpolluted site, far from traffic
4	5 30	45°25′50.6″	27°55′24.3″	Sendreni commune, Galati county, near a cultivated zone, at 1 km from the steel complex of Galati
5	5 30	45°24′31.3″	27°58′36.3″	Movileni village, Sendreni commune, near the South gate of the steel complex of Galati
6	5 30	45°27′19.4″	27°58′22.5″	Smardan commune, near the North gate of the steel complex of Galati
7	5 30	46°01′27.90″	27°43′45.55″	Adam village, Draguseni commune, Galati county, unpolluted site

2.2. Sample preparation

For the XRF analysis, the soil samples were dried, the foreign objects were removed, and then the samples were crushed into a fine powder using a mortar and pestle. The soil was encapsulated in specially made capsules to be used for the quantitative and qualitative determination of 20-22 elements.

For GC-ECD and GC-MS determination, 1 g of soil sample is used, treated consequently with internal standard solutions and a mixture of hexane-acetone. This procedure is named Soxlet method [2].

2.3. Instrumentation

The XRF determinations were performed using a Niton XLT analyzer from 700 series. It is a portable device that offers reliable results, at low costs, in a short time, according to a non-destructive method, and a very simple sample preparation. These analyses were done at the European Center of Excellence, from the Faculty of Sciences, "Dunarea de Jos" University of Galati, Romania.

GC is an established and well accepted analytical method for trace organic compounds [3].

The GC-ECD and GC-MS were employed for the determination of pesticides and PAHs.

The determination of pesticides is accomplished using an Agilent 6890 gas chromatograph equipped with ^{63}Ni μECD detector and PAHs concentrations were obtained by using an Agilent 6890 gas chromatograph equipped with Agilent 5973 Network mass spectrometer (GC/MS 6890/5973).

These analyses were performed at Institute of Geology and Seismology, Laboratory of Geochemistry (GEOLAB) from Chisinau, Moldova.

3. Results and discussion

3.1. XRF results

For the XRF results, the soil sample is measured for five times, only the average value is in Table 2. The results indicate that the elements such as As, Cr and Ni are in all the cases above the normal values. For Pb, the normal values were exceeded at site 3, 5 and 6. In the case of sites 5 and 6, the values are indicating an anthropic pollution.

Zinc is an element that did not exceed in any place the normal values established by the Romanian legislation [4].

3.2. GC-ECD and GC-MS results

The concentrations of the organic pollutants are presented in Table 3. Phenanthrene in this case is representing 94.69%, from the PAHs concentration. In the case of pesticides b_BHC is representing 47% from the entire concentration. According to the Romanian legal norms [4] under normal conditions the total amount of PAHs should not exceed 0.1 mg kg^{-1}.

In this case the total amount is 3.831 mg kg^{-1}, value found between the normal values and the alert threshold for sensitive areas.

Table 2. *Heavy metals concentration obtained by the XRF technique*

Sample No.	As (mg kg^{-1})	Cr (mg kg^{-1})	Cu (mg kg^{-1})	Ni (mg kg^{-1})	Pb (mg kg^{-1})	Zn (mg kg^{-1})
1 /5 cm	9.9	90.09	29.7	60.71	17.22	73.11
1/20 cm	10.51	83.4	26.63	51.25	15.3	65.38
2/5 cm	5.99	57.1	19.34	38.05	15.21	52.29
2/ 15 cm	8.01	55.13	17.04	41.7	12.16	42.58
3/5 cm	9.62	102.34	22.66	59.11	20.67	68.546
3/30 cm	11.06	124.72	n.d.	58.15	23.82	82.03
4/5 cm	9.5	83.728	23.68	51.64	18.9	51.404
4/30 cm	10.29	73.01	27.47	63.86	16.51	46.397
5/5 cm	10.3	52.906	29.89	65.55	30.37	71.484
5/30 cm	10.21	71.43	34.2	63.73	29.74	77.168
6/5 cm	9.813	99.194	25.13	62.67	25.63	61.62
6/30 cm	10.55	83.752	24.82	59.45	21.4	61.19
7/5 cm	7.19	69.322	18.38	44.71	11.02	34.072
7/30 cm	6.24	96.155	n.d.	36	11.15	19.51

Table 3. *Organic compounds concentration obtained by GC and GC-MS technique*

Sample No.	**PAHs** (mg kg^{-1})				**Pesticides** (mg kg^{-1})			
	Naphtalene	Fluorene	Phenanthrene	Antracene	a_BHC	b_BHC	Heptachlor	Trifluralin
1 /5 cm	0.001	0.007	0.027	<0.001	<0.002	<0.002	<0.003	<0.002
1/20 cm	0.002	0.021	0.045	0.002	<0.002	<0.002	<0.003	<0.002
2/5 cm	<0.004	0.033	1.345	0.194	0.027	0.019	0.108	0.231
2/ 15 cm	<0.004	0.023	0.876	0.125	<0.002	<0.002	<0.003	<0.002
3/5 cm	0.001	0.007	0.067	0.004	<0.002	<0.002	0.346	<0.002
3/30 cm	<0.004	<0.001	0.029	<0.001	<0.002	<0.002	<0.003	<0.002
4/5 cm	<0.004	<0.001	0.006	<0.001	2.159	4.273	<0.003	0.152
4/30 cm	<0.004	<0.001	<0.001	<0.001	0.065	0.053	0.260	<0.002
5/5 cm	0.001	0.006	<0.001	0.043	<0.002	<0.002	0.524	<0.002
5/30 cm	<0.004	0.010	<0.001	0.038	0.062	<0.002	<0.003	<0.002
6/5 cm	0.010	0.008	0.008	0.010	0.022	<0.002	<0.003	<0.002
6/30 cm	<0.004	<0.001	<0.001	0.004	0.373	0.203	0.333	<0.002
7/5 cm	0.007	0.006	0.044	<0.001	0.074	<0.002	<0.003	<0.002
7/30 cm	<0.004	<0.001	<0.001	<0.001	<0.002	<0.002	<0.003	<0.002

4. Conclusions

The highest concentration of pesticides is found at location 4, which is an agricultural area.

The highest concentration of PAH is found for location 2, which is close to a stable and to an agricultural area.

The high amount of PAHs can be explained by the waste incineration and also by its closeness to a main industrial point.

The heavy metal concentration is maximum at site 3 and minimum at site 2. Site 3 exhibits the highest amounts of Cr.

This metal is also found in pesticides and this can be the most probable source, because the site is close to a cultivated area.

Acknowledgements

This paper was supported in part by *Project TIPSARMER 72-172/1.10.2008* funded by the National Plan of Research, Developing and Innovation, of implementation of high precision and sensibility methods for the bio-monitoring of the environmental pollution in South, South-East and Central regions of Romania.

The work of Alina Sion (Bosneaga) was supported *by Project SOP HRD - SIMBAD 6853, 1.5/S/15 - 01.10.2008.*

Ene Antoaneta would like to acknowledge the support provided by the European Union, Romanian Government and Dunarea de Jos University of Galati, through the project POSDRU 21/1.5/G/19524.

References

[1]. S. Almaula, (2005), Polycyclic Aromatic Hydrocarbons from Steelmaking, Environmental Forensics, 6, 143–150.

[2]. Mattina, M.I., Lannucci-Berger, W., Musante, C., White, J.C., (2003), Concurrent plant uptake of heavy metals and persistent organic pollutants from soil, Environ Pollution, 124, 375-378.

[3]. D. Pilla, A.K.M. Kavadi, P. Gurijala, S. Masuram, M.S. Delaney, M.E. Merchant, J. Sneddon, (2009), Determination of selected chlorohydrocarbons and polyaromatic hydrocarbons by gas chromatography-mass spectrometry in soils in Southwest Louisiana, Microchemical Journal, 91, 13-15.

[4]. ***Reference Values for Trace Elements in Soil***, Monitorul Oficial al Romaniei, No. 303 bis/ 6 XII 1997.

THE ANNALS OF "DUNAREA DE JOS" UNIVERSITY OF GALATI.
FASCICLE IX. METALLURGY AND MATERIALS SCIENCE
N^0. 4 – 2011, ISSN 1453 – 083X

TITANIA NANOSTRUCTURES PREPARATION FOR GAS SENSOR APPLICATIONS*

Violeta NECHITA* and Viorica MUSAT
Centre of Nanostructures and Functional Materials-CNMF,
"Dunărea de Jos" University of Galati
*Corresponding author
email: nekitta_vio@yahoo.com

ABSTRACT

The preparation and structural characterization of titanium oxide nanowires as functional materials for the development of chemical sensors is presented in this work. The new types of materials for sensorics, aspects of material preparation relevant for gas sensing applications is presented .The functional characterization is focused on the detection of alcohols. Titanium oxide thin films prepared by solvotermalthermal method in highly alkaline conditions and the performance of 1D nanostructure is compared with mesoporous thin film prepared by sol-gel method.

KEYWORDS: TiO_2, conductometric gas sensor, nanostructures, mesoporous materials

1. Introduction

Many fields of nanotechnology are based on physical and chemical interactions, involving nanoparticles of particular size and shape. In order to use the nanomaterials as sensors it is fundamental to understand the aspects involved in the synthesis and also in interaction mechanism during the sensing act. The ability to systematically manipulate the size and shape of metal oxide nanoparticles is a major scientific breakthrough in opening new ways for production of materials capable of sensing.

It has been known that the electrical resistance of the semiconductor material (like TiO_2, which is n-type) is sensitive to the presence of gases at elevated temperatures (200-600˚C). As an example, reducing gases (CO, H_2, CH_4, etc.) lead to an increase of the conductivity, whereas the effect of oxidizing gases (O_3, etc.) is vice versa.

The model most frequently mentioned in the literature is based on the fact that oxygen atoms absorbed or adsorbed at the surface form negative ions resulting in a decrease in the surface conductivity.

Three different types of ionic species have been observed on the surface in addition to adsorbed O_2 molecules: O_2^-, O^-, and O^{2-}, which are desorbed at characteristic temperatures [1]. The presence of a reactive gas (oxidant or reducer) in the atmosphere, its adsorption at the surface and its reaction with the oxygen atoms will result in a decrease or an increase in surface electrons and, hence, in the conductivity. Typically, the value measured is the resistance of the semiconductors, *Rs:*

$$R_S = KC_S^{-\alpha} \quad (1)$$

where C_s is the concentration of gas in air, K the sensitivity coefficient, and α is the dimensional power exponent between 0 and 1. In most cases however, the value given is the sensitivity value, that is, the ability of a sensor to detect a given concentration of a test gas (analyte), is usually estimated as the ratio of the metal oxide electrical resistance (conductivity) ($S = R_{gas}/R_{air}$, or R_{air}/R_{gas}) measured in air and in an atmosphere containing the target gas.

A typical sensor element (Fig. 1) comprises the following parts:

- *Sensitive layer* deposited over a
- *Substrate* (glass, Si, SiO_2, ceramics) provided

*Paper presented at the Symposium ***"The Impact of Nanotechnologies and Nanomaterials on Industrial Development and Quality of Life",*** Galati, May 19, 2011, organized by the Center for Nanostructures and Functional Materials (CNMF), Faculty of Metallurgy, Materials Sciences and Environment, "Dunarea de Jos" University of Galati

with

• *Electrodes* (Pt, Pd, Au, etc.) for the measurement of the electrical characteristics. The device is generally heated by its own

• *Heater*; this one is separated from the *sensing layer* and the *electrodes* by an electrical insulating layer [2].

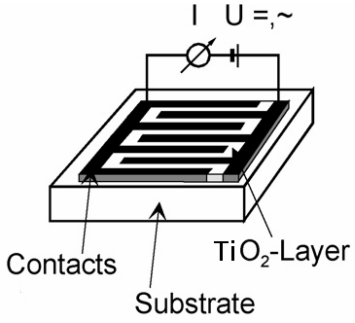

Fig. 1. *Representation of a sensor element.*

Conductometric (resistive) metal oxide sensors comprise a significant part of the gas sensor component market. While many different approaches to gas detection are available, metal oxide sensors remain a widely used choice for a range of gas species. These devices offer low cost, high sensitivity, fast response and relative simplicity. Also, these sensors possessed a number of unwanted characteristics, such as high cross-sensitivity, sensitivity to humidity and long-term drift. In order to improve their performance a series of various metal-oxide semiconductors have been tested such as: SnO_2, ZnO, TiO_2, WO_3 etc.

It was settled that the sensor characteristics can be changed by varying the crystal structure, dopants, preparation technology, operation temperature, etc. Nonetheless, highly specific metal-oxide sensors were still not available. In recent years, the interest of researchers to gas-sensitive materials has grown substantially due to the progress in nanotechnology. This interest is primarily related to the promising electronic properties of nanomaterials, their size dependence and ability to control the material structure by new experimental techniques. More and more materials and devices are produced every year with the use of nanotechnology. This paper discusses several synthetic strategies for preparation of nanostructured materials for gas sensor applications.

2. Nanostructured materials obtained used for new generation sensors

Up to now a large number of publications reported the capability of nanosized TiO_2 to detect gas molecules of organic compounds (alcohol, methanol, n-propanol, acetone, benzene) [3-6], oxidants (NO_2, CO, O_2) [7–10], and reductants (H_2, NH_3) [11–13] have been reported for nanosized TiO_2.

The metal oxide film can take a number of forms, generally determined by the deposition method.

Films deposited using chemical vapor deposition or sputtering tend to be thin and compact. Films deposited by casting of sol–gels and colloidal dispersions, tend to be thicker and porous with nanostuctured features.

2.1. Porous nanostructured materials obtained by sol–gel methods

Sol-gel processing is a low temperature, high versatile synthesis route that is particularly suitable for the deposition of thin nanostructured films from a liquid phase. It is efficacious way to control the dimensions of the grains. By reducing the particles sizes, the conduction of the sample may be controlled either by the grain boundaries, necks, or by the grains. The latter case is the most desirable, since it allows achieving the highest resistance change.

In the synthesis, the precursors, which are usually inorganic metal salts or metal organic compounds such as metal alkoxides, undergo hydrolyze followed by condensation and polymerization reactions. Complete polymerization and loss of solvent leads to a solid gel phase [14]. In case of titania, as precursors can also be used titanium halides.

Several factors are known to affect the hydrolysis reaction:

(a) the nature of the precursor;

(b) the nature of the solvent;

(c) the concentration of each species in the solvent;

(d) the temperature;

(e) the water to precursor molar ratio;

(f) the presence of acid or base catalysts.

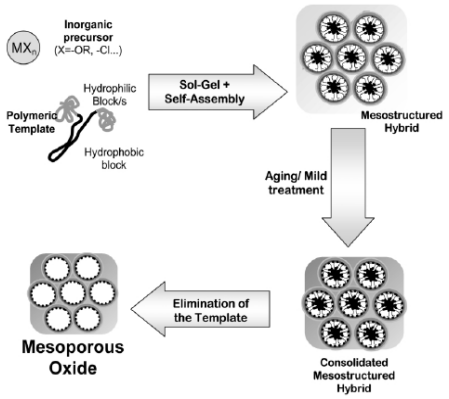

Fig. 2. *Schematic view of the steps leading from a solution to a mesoporous oxide network [21].*

The properties of sol-gel materials can be enhanced by increasing their surface area by making them porous materials. In such material the volume of the layer is accessible to the gases and therefore the active surface is much higher than the geometric area and the sensor response is higher. Thus, mesoporous TiO_2, fabricated using a self-assembly of a surfactant (Fig. 2) exhibit higher sensor performance than corresponding metal-oxide materials, having lower specific surface area.

Depending on the required pore size, block copolymers, latex spheres, water-in-oil emulsions, polystyrene particles, colloidal crystals, and bioskeletons have been used as templates [15-18]. The most commonly used organic templates were amphiphilic poly (alkylene oxide) block copolymers, such as $HO(CH_2CH_2O)_{20}$-$(CH_2CH(CH_3)O)_{70}$ $(CH_2CH_2O)_{20}H$ (called Pluronic P-123) and $HO(CH_2CH_2O)_{106}(CH_2CH(CH_3)O)_{70}$-$(CH_2CH_2O)_{106}H$ (called Pluronic F-127). Carbon nanotubes [19] and mesoporous SBA-15 [20] have also been used as the skeleton for mesoporous TiO_2. A disadvantage of using a template is that the dominant length scale of the resulting porous structure is fixed by the template size.

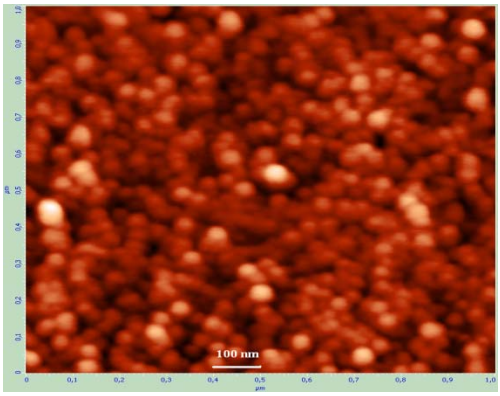

Fig. 3. *AFM image of TiO_2 thin mesoporous film [25].*

Recently, Sanchez and co-workers showed the formation of highly organized mesoporous titania thin films [21-24]. Our group obtained TiO_2 mesoporous thin film (Fig. 3) with average roughness 0.9969 nm, grains 27-40 nm, and average pores' diameter 17 nm [25].

M.M. Yusuf and coworkers [26] prepared a porous anatase film by the surfactant-templeting method having the porosity of about 64% and grain size of 30 nm. The grains are columnar as a result of surfactant micelles shape before annealing process.

Yu et al. prepared three-dimensional and thermally stable mesoporous TiO_2 without the use of any surfactants [27]. Briefly, monodispersed TiO_2 nanoparticles were formed initially by ultrasound-assisted hydrolysis of acetic acid modified titanium isopropoxide. Mesoporous spherical or globular particles were then produced by controlled condensation and agglomeration of these sol nanoparticles under high-intensity ultrasound radiation.

The mesoporous TiO_2 had a wormhole-like structure consisting of TiO_2 nanoparticles and a lack of long-range order [27].

2.2. Porous doped nanostructured materials

The application of nanotechnology in preparation of gas sensors is not limited by production of nanostructured semiconducting thin films only. It is known that by dispersing a low concentration of metallic nanoparticles (such as Pd, Pt, Nb, La, Cu, W, Cr, Sn, etc.) on the TiO_2 grains, the sensitivity and selectivity can be improved [28-33]. Carney et al. found that sensors based on SnO_2-TiO_2 with higher surface areas were more sensitive to H_2 [34]. Devi et al. found that ordered mesoporous TiO_2 exhibited higher H_2 and CO sensitivities than sensors made from common TiO_2 powders due to increased surface area, and the sensitivity could be further improved by loading the sensor with 0.5 mol % Nb2O5 [35].It has been observed that TiO_2 doped with Nb and Pt sensors have a good performance in detecting ethanol vapor [36-40], while Cu- or Co- doped TiO_2 nanoparticles were good candidates for CO sensing [41].

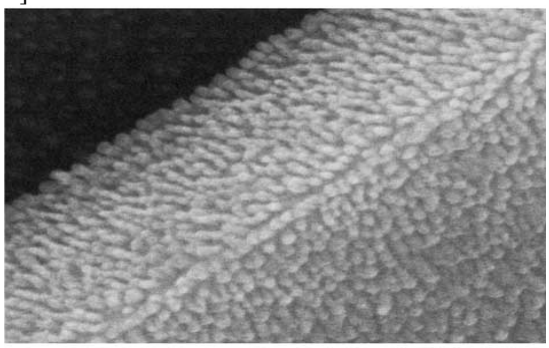

Fig. 4. *SEM image of TiO_2 film [26].*

Also, one of the most popular nanomaterials nowadays, carbon nanotube (CNT), was used as dopant to improve the gas detection. It was found that CNTs can be added to TiO_2 substrate to form alcohols-sensitive material. The doping increases the sensitivity in comparison with pure TiO_2 sensor. Hybrid SWCNTs/Nb-Pt co-doped TiO_2 thin films were prepared by the sol–gel spin-coating process [42]. The SWCNTs were well embedded in the TiO_2 matrix and did not affect the morphology of the TiO_2 thin film and the particle size. Experimental results revealed that the responses to ethanol of Nb–Pt co-doped TiO_2 sensors with SWNCTs inclusion increase by factors of 2–5, compared to that of the sensor

without SWCNTs. Moreover, all hybrid sensors can operate with high sensitivity and stability at relatively low operating temperature (<335 ˚C).

Titania (usually in the rutile phase) is widely used bulk conductivity sensors for oxygen [43-44]. The detection mechanism implies the diffusion of oxygen ions in the bulk of the material, at high temperatures (700–1000 ˚C).

For anatase titania, oxygen detection can be associated to a surface reaction, which takes place at lower temperatures (400–500 ˚C). Llobet et al. [45] achieved at significantly lower operating temperature (350 ˚C), a response more than four times higher than the one found for titania not containing carbon nanotubes.

Pt addition in TiO_2 promoted the structural transformation of the starting anatase phase to rutile, with a more enhanced effect with increasing the Pt concentration. H_2 gas-sensing tests evidenced that the anatase phase was much more sensitive than the rutile one. The presence of Pt further enhanced the gas-sensing properties, lowering the optimum sensor operation temperature to about 330 ˚C [46].

In our work [25] we obtained an Nb doped TiO_2 mesoporous thin film with average roughness of 0,594704 nm, grain size: 19-26 nm and pore diameter: 16 nm (Fig. 5).

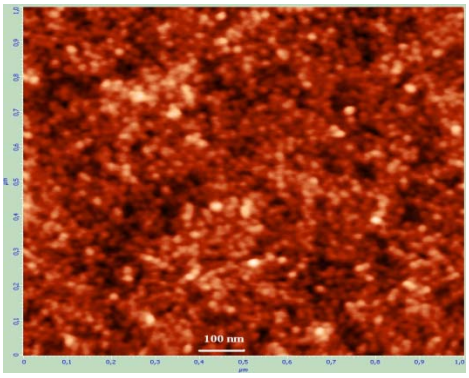

Fig. 5. *Nb (1wt.%)-TiO_2 mesoporous thin film [25].*

2.3. 1D nanostructured materials for new generation of gas-sensors

Nowadays, most of the commercial metal-oxide gas sensors are manufactured using the screen-printing method on small and thin ceramic substrates. The power consumption of this kind of sensor can be as high as 1 W, which makes it impossible to use in battery-driven devices. Also they face problems with thermal isolation between sensor element and housing. These shortcomings promote the development of substrate technology and strong research in sensitive layer preparation. Concerning the substrate issue, one way to solve it is the integration of sensing layer in standard microelectronic processing.

At present, the efforts are focused on the sensing layer. This layer can be compact or porous, depending on the preparation technique used. Typically, porous layers possess higher active surface than the geometric one. The most common sensor preparation techniques are presented in Table 1.

Table 1. *Deposition techniques used for the preparation of metal oxides [49]*

Paste/slurry deposition	CVD	PVD	
		Sputtering	Evaporation
Screen-printing	Thermal	Sputtering	Molecular beam epitaxy
Drop deposition	Plasma activated	Reactive sputtering	Thermal evaporation
Dip coating	Laser induced	Cathode sputtering	Reactive evaporation
Spray deposition	Electroless plating	With bias voltage	Ion plating
			Reactive ion plating
			Arc evaporation
			Laser evaporation

Nanotechnology provided the new tools to control the microstructure of sensitive layer, allowing to obtain materials with narrow grain size distribution, this meaning a greater stability in time. The studies of thin films of TiO_2 have shown the strong increase of sensitivity with the reduction of the oxide particle size to nanometer scale. Systematic analysis of grain size dependence of TiO_2 sensitivity was reported in literature. [47-48]

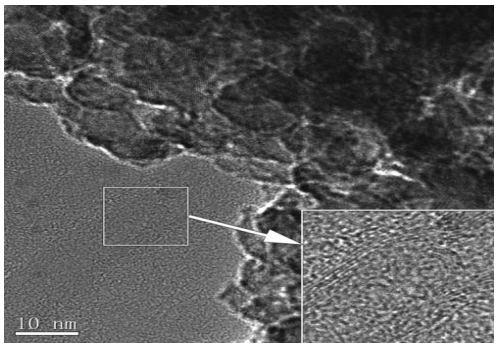

Fig. 6. *Nb (3wt.%), CNT(0.002wt.%) -codoped TiO_2 [45].*

New promising methods are based on deposition of metal on a substrate followed by oxidation. Controlling the oxidation parameters the stoichiometry of the oxide can be varied. After annealing, the particles can be oxidized (totally or partly) to form the highly porous sensitive layer.

Among these techniques there are Rheotaxial Growth and Thermal Oxidation (RGTO), Low Temperature Physical Vapor Deposition (LTPVD) and sputtering-oxidation method.

Other methods, based on modified sol–gel, solvothermal method and CVD techniques are also used to improve the gas sensor performance of nanostructured metal-oxide materials.

2.3.1. One-dimensional metal oxide structures

Semiconducting one-dimension metal oxide structures with well defined geometry and perfect crystallinity represent a material family for systematic experimental study and theoretical understanding of the gas-sensing mechanisms in semiconducting metal oxides. In analyzing the opportunities of one-dimensional structures of various types for their practical application in gas sensors, nano-belts (nano-ribbons) probably could be the most promising one-dimensional structure to exploit for gas-sensing applications. Nano-belts are thin and plain belt-type structures with rectangular cross-section. At present, nano-belts have been obtained for nearly all oxides used in gas sensors. There is considerable data pertaining to the synthesis of nano-belts for SnO_2, TiO_2, In_2O_3, ZnO, Ga_2O_3, etc.. Typical nano-belts have widths of 20–300 nm, and lengths from several mm to hundreds, or even some thousands of mm.

The typical width-to-thickness ratio for nano-belts ranges from 5 to 10 and for nanowires (or nanorods) this ratio equals 2–5. Synthesis of 1D nanostructures could be done through various methods. Nano-belts, for example, have structural homogeneity and crystallographic perfection. It is well known that crystallographic defects may destroy quantum-size effects. It is necessary to emphasize that that suitable geometry (see Fig. 7), high homogeneity of the structure, and long length are important advantages of nano-belts for mass manufacturing of gas sensors.

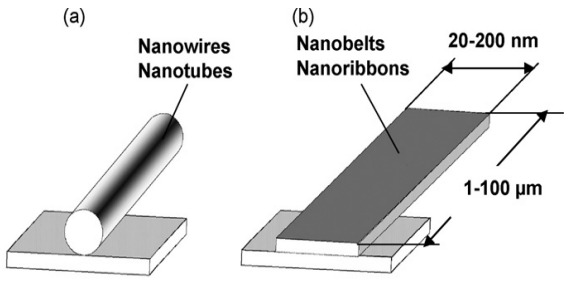

Fig. 7. *Nanowires (a) and nano-belts (b) position on bonding pad and typical sizes of nano-belts used in gas sensor design.*

It is necessary to note that many parameters used for characterizing polycrystalline materials aimed for gas sensor design lose meaning for one-dimensional structures, because they are single crystalline materials.

These parameters include the following: film thickness, porosity, grain size, grain network, grain boundary, agglomeration, and texturing, i.e. all the parameters that it is considered to influence the metal oxide sensor response. The main structural and morphologic parameters that characterize one-dimensional structures would become geometric sizes, characterizing the profile of one-dimensional structures, and crystallographic planes, framing these one-dimensional structures. At that, the minimal distance between faceting planes in one-dimensional structures would play in gas-sensing effects the same role as grain size plays in polycrystalline material. It should be noted that one-dimensional structures have better crystallinity (i.e. less concentration of point defects), and thus possibly a lower concentration of free charge carriers, in comparison with polycrystalline materials. On the other hand, in one-dimensional gas sensors the role of contacts increases because of their small area and therefore greater specific resistance.

With regard to the sensors on the base of nanowire arrays, there are the same regulations for them as for the ones on the base of the usual nanoparticle films. Impedance spectroscopy studies have showed that the gas-sensing mechanism for sensors on the base of networked nanowire thin films involves changes in both the nanowire and the inter-nanowire boundary resistances [49].

For gas sensor design the thin films, containing nanowires in a highly networked fashion, are promising. A study, carried in [49] has shown that the sensors on the base of those films had a behavior, similar to that of single nanowire devices without much post-processing effort. According to Ref. [50] this is possible only when the individual nanowires within the gas-sensing matrix are bonded to each other and form two- and three-dimensional networks of nanowires.

Solvothermal method involves a reaction of a hot solution within or on the surface of a substance, proceeds in a sealed pressure vessel (autoclave) at temperatures above the boiling point of the solvent.

Fig. 8. *The general scheme for 1D TiO_2 nanostructures synthesis.*

Solvothermal synthesis is a ''soft solution chemical processing'' which provides an easy route to prepare a well crystalline oxide under the moderate reaction condition, i.e. low temperature and short reaction time (Fig. 8).

When the solvent is water, the method is called hydrothermal. The solvothermal method normally has better control than hydrothermal methods of the size and shape distributions and the crystallinity of the TiO_2 nanoparticles.

The hydrothermal method has been widely used to prepare TiO_2 nanotubes since it was introduced by Kasuga et al. [51] in 1998, also is very simple and inexpensive. Over the years, they carried out many research on 1D titania, for example supported nanowires [52]. Grimes et al. conducted a series of excellent studies on sensing using TiO_2 nanotubes [53-58]. They found that TiO_2 nanotubes were excellent room-temperature hydrogen sensors not only with a high sensitivity but also with ability to self-clean photo actively after environmental contamination.

Many other groups have synthesized and investigated the properties of 1D TiO_2 nanomaterials for different applications [59-63]. Lee and coworkers [59] developed a low temperature synthesis of TiO_2 nanowires directly synthesized on fluorine-doped tin oxide (F:SnO_2 or FTO)-coated soda-lime glass substrates (Fig.9). They use successfully these nanowires in photovoltaic cells.

Figure 10 shows rutile nanorods obtained through a combined sol-gel and solvothermal method. C. Su and co.[60] demonstrated that these particles have a good photocatalytic activity and , modifying the synthesis parameters can be obtained particles with different shapes and properties.

The solvothermal method can be associated with different techniques. Porous single-crystalline TiO_2 nanorods have been prepared though a solution aggregation-based growth process followed by the calcination treatment.

The morphology of the resulting nanorods can be tuned with different surfactants [64] or by changing the solvent compositions [65]. TiO_2 nanorods with narrow size distributions can also be developed with the solvothermal method. For example, in a typical synthesis from Kim et al. [66], TTIP was dissolved in anhydrous toluene with OA as a surfactant and kept at 250℃ for 20 h in an autoclave without stirring.

Long dumbbell-shaped nanorods were formed when a sufficient amount of TTIP or surfactant was added to the solution, due to the oriented growth of particles along the [001] axis.

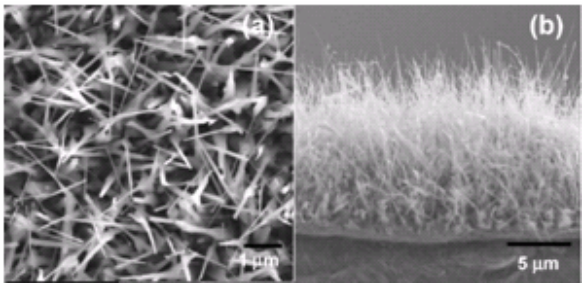

Fig. 9. *Images of TiO_2 nanowires (a) (top view) and (b) cross-sectional SEM [52].*

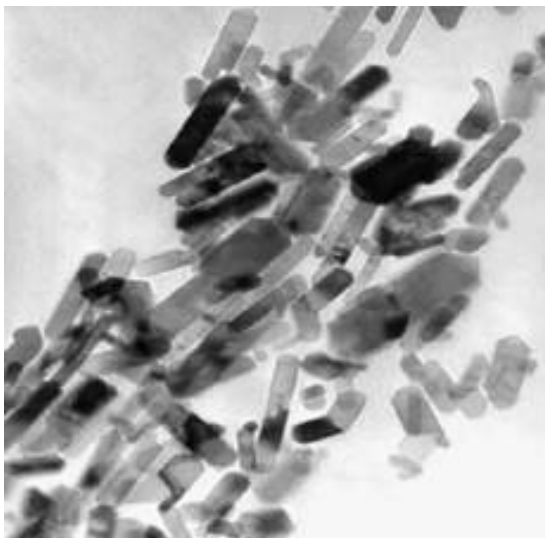

Fig. 10. *The TEM micrographs of TiO_2 nanorods [60].*

The average particle size was smaller and the size distribution was narrower than is the case for particles synthesized without surfactant.

The crystalline phase, diameter, and length of these nanorods are largely influenced by the precursor/surfactant/solvent weight ratio.

The diameter and length of these nanorods were in the ranges of 3-5 nm and 18-25 nm, respectively.

Concerning the 3D → 2D → 1D formation mechanism various hypotheses have been proposed. In case of TiO_2 nanotubes, Wang and co-workers [67] stated that the raw TiO_2 was first transformed into lamellar structures and then bent and rolled to form the nanotubes and the two-dimensional lamellar TiO_2 was essential.

Also, the doping of 1D nanostructures with ions was used to improve their sensitivity. Proton-exchange was carried out by suspending the TiO_2 nanotubes (Fig. 11) [68] in the corresponding aqueous solutions of the metal (Cu^{2+}, Co^{2+} and Ca^{2+}) nitrate or chloride at room temperature].

The exchange reactions were demonstrated to be an option for chemically modifying TiO_2 nanotubes. Additionally, the analysis of the products of thermal decomposition allowed to get information about the composition and structure of the nanotubes.

Despite the fact that the doping technique has been used for a long time in commercial and industrial sensors, the working principle of additive-modified metal-oxide materials is still not well understood.

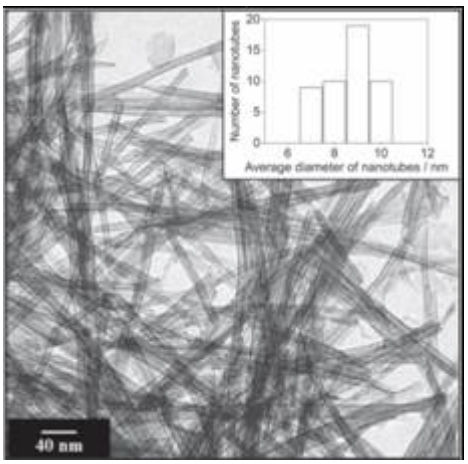

Fig. 11. *TEM image of titanium oxide nanotubes. The inset is a distribution of the average external diameter [68].*

In the chemical scheme the reaction takes place at the oxide surface. The role of the additive nanoparticles is considered within a spillover process, increasing the metal-oxide surface coverage of the gas involved in the sensing scheme. In the electronic mechanism the reaction involves the additive atoms and the oxide material has to transduce the electrochemical changes into a detectable output signal. Moreover, the introduction of additives can create new donor or acceptor levels, or influence the grain size and growth mechanism.

3. Conclusions and future prospects

The optimization of the structural parameters of metal oxides, such as grain size, porosity, texture, faceting, grain network, etc., is an important factor for improving gas-sensing characteristics of conductometric type sensors. For example, it was shown that grain size and porosity control are the best ways for the improvement of metal oxide sensor response to oxidizing gases.

For reducing gas detection the requirements are more ambiguous and depend on both the sensor material and the nature of the detected gas.

Nanotechnology is very promising for the preparation of clean, structurally pure perfectly ordered materials for the new gas sensors generation. Beside this, it helps researchers to understand the sensing mechanism at atomistic level, which undoubtedly will promote fast progress in this field.

New nanomaterials that appear today, such as highly ordered arrays of metal/semiconductor core–shell nanoparticles, may be soon used in gas sensor applications. At the same time, the creation of new materials for gas sensor applications is necessary to solve a number of basic problems of nanochemistry. Among them we consider the following ones as the most important:

a) Management of the size, structure and stability of metal, semiconductor and hybrid nanomaterials by controlled conditions of synthesis, in particular, with the use of low temperature synthesis.

b) Understanding of kinetics and thermodynamics of self organization processes, which take place at the surface of nanoparticles, and extension of the working temperature interval.

c) Determination of the influence of shape of nanoparticles, particularly for nanowires and nanotubes of different materials, on their chemiresistive properties.

The solution of these tasks in combination with the search of new nanosystems will allow the preparation of new sensor materials. The nanotechnology opens the new possibilities for the production of gas-sensitive materials of new types and also allows controlling the structure of conventional semiconducting metal-oxide materials on nanoscale level.

References

[1]. D. Kohl - Sens. Actuators B**,** 18 (1989) 71.
[2]. N. Barsan,l D. Koziej, U. Weimar - Sens. Actuators B 121 (2007) 18.
[3]. A.M. Taurino, S. Capone, A. Boschetti, T. Toccoli, R. Verucchi, A. Pallaoro, P. Siciliano, S. Iannotta - Sens. Actuators B 100 (2004) 177.
[4]. S.H. Si, Y.S. Fung, D.R. Zhu - Sens. Actuators B 108 (2005) 165.
[5]. L. Sun, L. Huo, H. Zhao, S. Gao, J. Zhao - Sens. Actuators B 114 (2006) 387.
[6]. A. Teleki, S.E. Pratsinis, K. Kalyanasundaram, P.I. Gouma - Sens. Actuators B 119 (2006) 683.
[7]. L. Francioso, D.S. Presicce, A.M. Taurino, R. Rella, P. Siciliano, A. Ficarella - Sens. Actuators B 95 (2003) 66.
[8]. L. Francioso, D.S. Presicce, M. Epifani, P. Siciliano, A. Ficarella - Sens. Actuators B 107 (2005) 563.
[9]. A.M. Ruiz, A. Cornet, J.R. Morante - Sens. Actuators B 100 (2004) 256.
[10]. Y.-K. Jun, H.-S. Kim, J.-H. Lee, S.-H. Hong - Sens. Actuators B 120 (2006) 69.
[11]. G.K. Mor, M.A. Carvalho, O.K. Varghese, M.V. Pishko, C.A. Grimes - J. Mater. Res. 19 (2004) 628.
[12]. H.-S. Kim, W.-T. Moon, Y.-K. Jun, S.-H. Hong - Sens Actuators B 120 (2006) 63.

[13]. C.M. Carney, S. Yoo, S.A. Akbar, - Sens. Actuators B 108 (2005) 29.
[14]. S.C. Tjong, H. Chen - *Nanocrystalline materials and coatings*, Mater. Sci. Eng. R 45 (2004) 1–88.
[15]. Beyers, E.; Cool, P.; Vansant, E. F. - J. Phys. Chem. B 109 (2005) 10081.
[16]. Peng, T.; Zhao, D.; Dai, K.; Shi, W.; Hirao, K. - J. Phys. Chem. B 109 (2005) 4947.
[17]. Lyu, Y. Y.; Yi, S. H.; Shon, J. K.; Chang, S.; Pu, L. S.; Lee, S. Y. Yie, J. E.; Char, K.; Stucky, G. D.; Kim, J. M. - J. Am. Chem. Soc. 126 (2004) 2310.
[18]. **Wang, Y.; Zhang, S.; Wu, X. -** Nanotechnology 15 (2004) 1162.
[19]. Yu, Y.; Yu, J. C.; Yu, J. G.; Kwok, Y. C.; Che, Y. K.; Zhao, J. C.;Ding, L.; Ge, W. K.; Wong, P. K. - Appl. Catal. A 289 (2005) 186.
[20]. Ding, H.; Sun, H.; Shan, Y. - J. Photochem. Photobiol. A 169 (2004) 101.
[21]. Galo J. de A.A. Soler-Illia, E.L. Crepaldi, D. Grosso, C. Sanchez - Current Opinion in Colloid and Interface Science 8 (2003) 109–126.
[22]. D. Grosso, F Cagnol, A.A. Soler-Illia, E.L. Crepaldi, and C Sanchez - Adv.Funct. Mater.14 (2004) 309.
[23]. Eduardo L. Crepaldi, Galo J. de A. A. Soler-Illia, D. Grosso, F. Cagnol, F. Ribot, and C. Sanchez - J. AM. CHEM. SOC. 125 (2003) 9770.
[24]. A. B. Dros, D. Grosso, C.Boissiere, G.J. de A.A. Soler-Illia,P.-A. Albouy, H. Amenitsch, C.Sanchez - Microporous Mesoporous Mater. 94 (2006) 208–213.
[25]. V.Nechita, V. Musat, Phys Status Solidi A, DOI:10.1002/pssa.201127057(2011)
[26]. M.M. Yusuf, H Imai, H Hirashima - J. Non-Cryst. Solids, 285 (2001) 90-95.
[27]. Liu, S.; Huang, K. - Sol. Energy Mater. Sol. Cells 85 (2004), 125.
[28]. A.M. Ruiz, G. Saka, A. Cornet, K. Shimanoe, J. Morante, N. Yamazoe - Sens. Actuators B 103 (2004) 312.
[29]. L. Francioso, D.S. Presicce, P. Siciliano, A. Ficarella - Sens. Actuators B 123 (2007) 516.
[30]. E. Comini, G. Faglia, G. Sberveglieri, Y.X. Li, W. Wlodarski, M.K. Ghantasala - Sens. Actuators B 64 (2000) 169.
[31]. **K. Zakrzeka,M. Radecka,M. Rekas -** Thin Solid Films 310 (1997) 161.
[**32]. R.K. Sharma, M.C. Bhatnagar, G.L. Sharma** - Sens. Actuators B 45 (1997) 209.
[33]. R.K. Sharma, M.C. Bhatnagar, G.L. Sharma - Sens. Actuators B 46 (1998) 194.
[34]. C.M.Carney, S. Yoo, S.A. Akbar - Sens. Actuators B 108 (2005) 29.
[35]. G. S. Devi,T. Hyodo, Y. Shimizu,M. Egashira - Sens. Actuators B 87 (2002) 122.
[36]. G. Sberveglieri, E. Comini, G. Faglia, M.Z. Atashbar, W. Wlodarski - Sens. Actuators B 66 (2000) 139.
[37]. A.M. Ruiz, A. Cornet, J.R. Morante - Sens. Actuators B 111–112 (2005) 7.
[38]. D.T.T. Le, D.D. Vuong, N.V. Hieu, N.D. Chien - Proceedings of the Eighth German–Vietnamese Seminar on Physics and Engineering(2005) 122.
[39]. D.T.T. Le, N.V. Hieu, N.D. Chien - Proceedings of the Ninth Asia Pacific Physics Conference (9th APPC), 2004, p. 391.
[40]. E. Comini, G. Faglia, G. Sberveglieri, Y.X. Li, W. Wlodarski, M.K. Ghantasala - Sens. Actuators B 64 (2000) 169.
[41]. A.M. Ruiz, A. Cornet, K. Shimanoe, J.R. Morante, N. Yamazoe - Sens. Actuators B 109 (2005) 7.
[42]. N.V. Hieu, N. V. Duya, P. T. Huya, N. D. Chienb - Physica E 40 (2008) 2950–2958.
[43]. Kirner U, Schierbaum K D, Gopel W, Leibold B, Nicoloso N, Weppner W, Fischer D and Chu W - Sens. Actuators B 1 (1990)103–7.
[44]. Sheng J, Yoshida N, Karasawa J and Fukami - Sens. Actuators B 41 (1997) 131.
[45]. E Llobet, E H Espinosa, E Sotter, R Ionescu, X Vilanova, J Torres, A Felten, J J Pireaux, X Ke, G Van Tendeloo, F Renaux, Y Paint, M Hecq and C Bittencourt - Nanotechnology 19 (2008) 375501.
[46]. M. Epifani , A. Helwig, J. Arbiol, R. Dıaz, L. Francioso, P. Siciliano, G. Mueller, J.R. Morante - Sens. Actuators B 130 (2008) 599.
[47]. G. Korotcencov - Mater. Sci. Eng., R 61 (2008) 1.
[48]. G. Korotcencov - Sens. Actuators, B 107 (2005) 209.
[49]. Sberveglieri G. - *Classical and novel techniques for the preparation of SnO_2 thin-film sensors*. Sens Actuators B 6 (1992) 239 – 47.
[50]. B. Deb, S. Desai, G.U. Sumanasekera, M.K. Sunkara - *Gas sensing behaviour of mat-like networked tungsten oxide nanowire thin films*, Nanotechnology 18 (2007) 7, 285501.
[51]. Kasuga, T.; Hiramatsu, M.; Hoson, A.; Sekino, T.; Niihara, K. - *Formation of Titanium Oxide Nanotube***,** Langmuir 14 (1998) 3160–3163.
[52]. T. Kasuga, M. Hiramatsu, A. Hoson, T. Sekino, K. Niihara - *Titania Nanotubes Prepared by Chemical Processing*, Adv. Mater 15.(1999) 11.
[53]. Mor, G. K.; Carvalho, M. A.; Varghese, O. K.; Pishko, M. V.; Grimes, C. A. - J. Mater. Res. 19 (2004) 628.
[54]. Mor, G. K.; Varghese, O. K.; Paulose, M.; Grimes, C. A. - Sens. Lett. 1 (2003) 42.
[55]. Varghese, O. K.; Gong, D.; Paulose, M.; Ong, K. G.; Grimes, C. A. - Sens. Actuators, B 93 (2003) 338.
[56]. Varghese, O. K.; Grimes, C. A., J. Nanosci. Nanotechnol. 3. (2003) 277.
[57]. Varghese, O. K.; Gong, D.; Paulose, M.; Ong, K. G.; Dickey, E. C.; Grimes, C. A - AdV. Mater. 15 (2003) 624.
[58]. Varghese, O. K.; Gong, D.; Dreschel, W. R.; Ong, K. G.; Grimes, C. A - Sens. Actuators, B 94 (2003) 27.
[59]. J-C Lee, T. G. Kim, W. Lee, S.-H. Han, and Y.-M Sung - *Growth of CdS Nanorod-Coated TiO_2 Nanowires on Conductive Glass for Photovoltaic Applications,* Crystal Growth & Design, Vol. 9, No. 10, 2009
[60]. C. Su, C.-M. Tseng, L.-F. Chen, B.-H. You, B.-C. Hsu, S.-S. Chen - *Sol–hydrothermal preparation and photocatalysis of titanium dioxide*, Thin Solid Films 498 (2006) 259 – 265.
[61]. K. Pan, Q. Zhang, Q. Wang, Z. Liu, D. Wang, J. Li, Y. Bai - Thin Solid Films 515 (2007) 4085–4091.
[62]. Zhang, Q.;Gao, L. - Langmuir 19 (2003) 967.
[63]. S. Yang, L. Gao - *Synthesis and Characterization of Porous Single-Crystalline Titanium Dioxide Nanorods*, J. Am. Ceram. Soc., 89 [2] (2006) 720–723.
[64]. S. Yang, L.Gao - Chem. Lett. 34 (2005) 964.
[65]. S. Yang, L. Gao - Chem. Lett. 34 (2005) 1044.
[66]. C. S Kim, B. K. Moon, J. H. Park, B. C.Choi, J H Seo -. J. Cryst. Growth 257 (2003) 309.
[67]. Y. Q Wang, G. Q Hu, X. F Duan, H. L Sun, Q. K. Xue -. Chem. Phys. Lett. 365 (2002) 427.
[68]. O.P. Ferreira, A. G. Souza Filho, J. Mendes Filho and O.L. Alves - *Unveiling the Structure and Composition of Titanium Oxide Nanotubes through IonExchange Chemical Reactions and Thermal Decomposition Processes* J. Braz. Chem. Soc. 17 [2] (2006) 393-402.

THE ANNALS OF "DUNAREA DE JOS" UNIVERSITY OF GALATI.
FASCICLE IX. METALLURGY AND MATERIALS SCIENCE
N^0. 4 – 2011, ISSN 1453 – 083X

GROWTH OF ZnO 1-D NANOSTRUCTURES BY CHEMICAL BATH DEPOSITION METHOD USING TEXTURED ZnO SEEDS*

M. MAZILU[1], V. MUSAT[1], N. TIGAU[2], P. MUNIZER[3], F. COMANESCU[3]

[1]Centre of Nanostructures and Functional Materials-CNMF, Dunărea de Jos University of Galaţi,
[2]Faculty of Sciences, Chemistry, Physics and Environment Department,
„Dunarea de Jos" University of Galati,
[3]IMT-Bucharest, National Institute for Research and Development in Microtechnologies Bucharest
email: viorica.musat@ugal.ro

ABSTRACT

A simple method has been developed to synthesize ZnO one-dimensional nanostructures on glass substrates from aqueous solution. The solution-based synthesis of oxide 1D nanostructures enables the fabrication of the next-generation of nano-devices at low temperature.

ZnO 1D nanostructures were grown on seeded glass substrates using zinc nitrate hexahydrate as the source of Zn, at temperatures up to 90℃. The morphology, crystalline structure and optical properties of the obtained nanostructures were characterized by scanning electron microscopy (SEM), X-ray diffraction (XRD), and optical spectra.

KEYWORDS: ZnO, chemical bath deposition, 1D nanostructures, seed layer, morphology, optical properties

1. Introduction

Zinc oxide (ZnO) is an interesting II–VI semiconductor because of its wide direct band gap of ~ 3.3 eV and large free-exciton binding energy of ~ 60 meV. On account of its various remarkable properties, such as excellent chemical and thermal stability, high-transparency in the visible region, near-UV emission, biocompatibility, and wide electrical conductivity range, ZnO is an excellent candidate for various electronic and optoelectronic devices [1, 2, 3].

Also, a lot of ZnO nanostructures have been reported, such as nanobelts (NBs), nanotubes (NTs), nanorods (NRs) or nanowires (NWs), and so forth [4]. One-dimensional semiconductor nanorod /nanowire structures have been widely used recently because of their special properties of quantum confinement, high surface-to-volume ratio, higher optical gain, faster response, and specific crystalline orientation [5].

ZnO nanorod/nanowire structures, in particular, have attracted a great attention in the last years due to their applications in sensors, cantilevers as well as in optoelectronic devices such as light-emitting diodes and excitonic solar cells [6].

Over the past few years, ZnO nanorods and nanowires have been synthesized with various methods including vapor-liquid-solid (VLS) epitaxy, chemical vapor deposition (CVD), pulse laser deposition (PLD), deposition within anodic alumina membrane channels, aqueous solution method, and so on. Aqueous solution approaches for the growth of ZnO nanostructures are considered advantageous, compared with other methods, mainly due to low growth temperature and good potential for large-scale production [7, 6].

In the present paper, we report the two steps synthesis of zinc oxide nanorod/nanowire arrays by a spin-coating method followed by a simple chemical bath deposition.

The effects of process parameters, seeded substrates and solution concentration, on the morphology, microstructure and optical properties of ZnO were investigated in details.

*Paper presented at the Symposium ***"The Impact of Nanotechnologies and Nanomaterials on Industrial Development and Quality of Life",*** Galati, May 19, 2011, organized by the Center for Nanostructures and Functional Materials (CNMF), Faculty of Metallurgy, Materials Sciences and Environment, "Dunarea de Jos" University of Galati

2. Experimental procedure

All the reagents (analytical grade purity) were purchased from Sigma Aldrich. They were used as received without any further purification.

The growth of ZnO nanorods/nanowires was carried out from aqueous solution of zinc nitrate ($Zn(NO_3)_2 \cdot 6H_2O$) and hexamethylenetetramine (HMT, $C_6H_{12}N_4$), by chemical bath deposition (CBD) method. Before coating, the glass substrates were cleaned with acetone in an ultrasonic bath and etched by piranha solution (2:1 mixture of concentrated H_2SO_4/30% H_2O_2). The as-grown ZnO nanowires were rinsed in deionized water and dried for 30 min at 90^{o}C for further characterization.

The *morphology* of obtained zinc oxide nanostructures were examined by scanning electron microscopy using a FEI Nova NanoSEM 630 - (SEM, Hitachi S-4200 and FE-SEM JEOL JSM-7000F). *The crystalline structure and orientation* of the 1D nanostructures were recorded at room temperature using a Rigaku SmartLab diffractometer, with Cu Kα radiation. *The optical transmission spectra* of the films were acquired at room temperature with a Perkin Elmer Lambda 35 spectrometer, operated in air, at normal incidence, in the 300 nm – 1100 nm spectral range. From the optical measurements, *the optical energy gap*, Eg, was calculated assuming a direct transition between the edges of the valence and the conduction bands, for which the variation in the absorption coefficient, α, with photon energy, hν, is given by the equation:

$$(\alpha h\nu)^2 = B(h\nu - Eg) \quad (1)$$

By plotting $(\alpha h\nu)^2$ versus hν and extrapolating the linear region of the resulting curves, Eg was obtained.

Raman spectra measurements were carried out on Raman spectrometer (LabRAM HR 800 Raman Spectrometer). The He-Ne laser with wavelenght 633 was used as a source of excitation.

3. Results and discussion

In the reaction for growing the zinc oxide nanoarrays, the HMT plays an important role. It decomposes to formaldehyde and ammonia, which acts as a *p*H buffer and supply of OH^- ion slowly [3, 4, 8-10].

The main chemical reaction process can be described as follows:

$$(CH_2)_6N_4 + 6H_2O \rightarrow 6HCHO + 4NH_3 \quad (2)$$
$$NH_3 + H_2O \leftrightarrow NH_4^+ + OH^- \quad (3)$$
$$2OH^- + Zn^{2+} \rightarrow Zn(OH)_2 \quad (4)$$
$$Zn(OH)_2 \rightarrow ZnO + H_2O \quad (5)$$

Figure 1 shows that higher solution concentration leads to larger diameter of zinc oxide nanowires. The average diameters of the as-prepared samples grown from solutions of 0.01 M, and 0.025 M are 14 nm (Fig. 1a) and 25 nm (Fig. 1b), respectively.

In addition, it can be observed an increase of the density of ZnO NWs on the substrate when the concentration of aqueous solution increases.

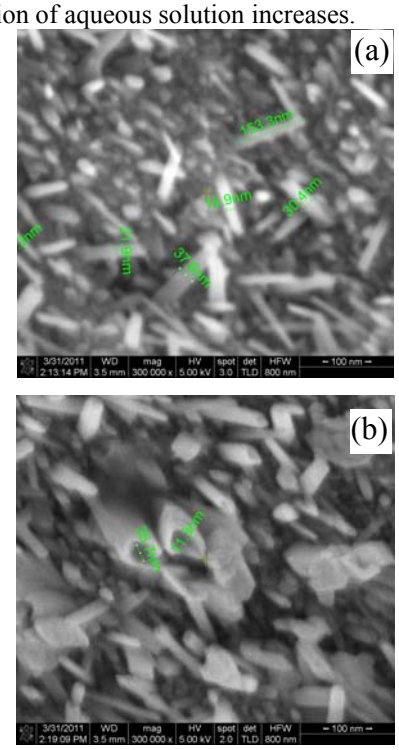

Fig 1. *SEM imagines of ZnO 1D nanomaterials grown aqueous solution of (a) 0.01M and (b) 0.025M.*

Figure 2 presents the XRD patterns of the grown ZnO nanowires.

These patterns show, in the 2θ range 25-50, the most important three peaks of hexagonal wurtzite type of ZnO structure. One can notice from the XRD data that all samples are polycrystalline and exhibit single phase ZnO hexagonal wurtzite structure with *c*-axis (002) oriented.

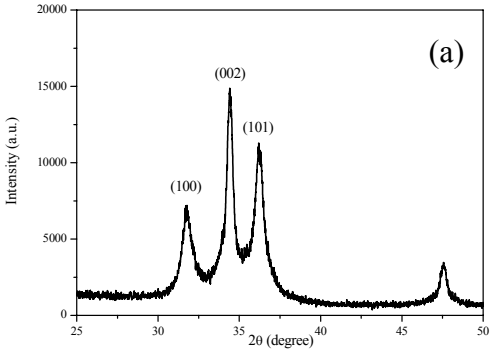

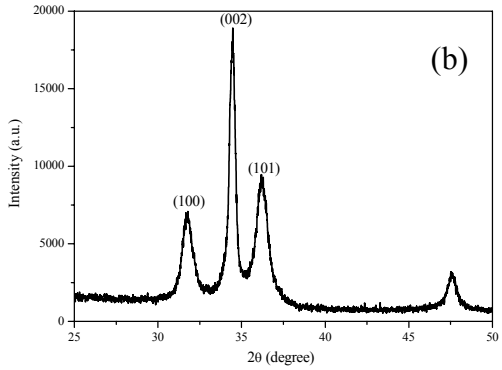

Fig.2. *XRD patterns of ZnO 1D nanomaterials grown from solution of (a) 0.01M and (b) 0.025M.*

The intensity of (002) diffraction peak is higher than the intensity of other peaks, which indicates the nanowires are highly *c*-axis oriented and normal to the substrate surface. The intensity of (002) plane increases when the molarity of aqueous solutions of $Zn(NO_3)_2$ and $C_6H_{12}N_4$ increases. Figure 3 shows the optical transmittance spectra of the films in the wavelength region range from 300 to 1100 nm. Transmittance in the visible and near-infrared regions exceeds 50% for all samples with a sharp ultraviolet absorption edge around 374 nm.

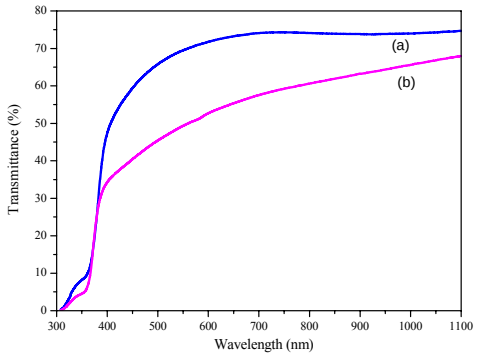

Fig. 3. *Optical transmittance spectra of samples obtained from solution of 0.01M (a) and 0.025M (b).*

In addition, the ZnO 1D nanostructures grown from the precursor concentrations of 0.025M presents a decrease in transmittance and shows a red-shift of absorption edge, which may be attributed to the increase of grain size.

The optical transmittance data have been used for the calculation of direct optical energy gap (Figure 4), according to the equation (1).

The band gap values decrease from 3.80 to 3.77 eV when the concentration solution increases from 0.01 to 0.025 M, respectively.

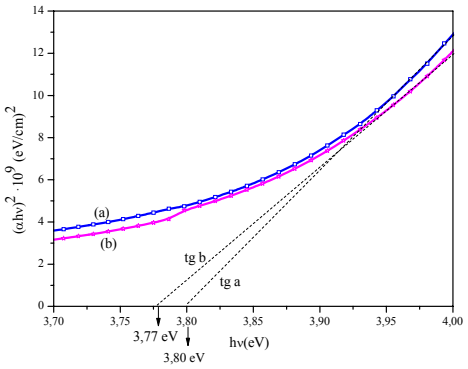

Fig. 4. *The plots of $(\alpha h\upsilon)^2$ vs. photon energy ($h\upsilon$) for samples obtained from solution of 0.01M (a) and 0.025M (b).*

The decrease of *Eg* can be attributed to the increase of grain size with increasing concentration. The band gap energy, a constant of bulk materials, varies in thin films due to particle size effect [10].

4. Conclusions

ZnO 1D nanostructures have been successfully synthesized on glass substrates by chemical bath deposition method.

The influence of the concentration of the precursor solution on the morphology, microstructure and optical properties of the obtained 1D nanostructres was studied.

The morphology is sensitive to the conditions of the preparation. X-ray diffraction data reveal that the as-grown 1D nanostructures has wirtzite structure with preferential orientation along the (002).

The optical transmittance decreases when the concentration increases. The optical band gap of the samples ranges from 3.79 to 3.77 eV when the precursor solution decreases.

Acknowledgements

This work was supported by NMT ERA-NET-MULTINANOWIRES Grant (Contract NMT7-029-2010).

References

[1]. D. Byrne, E. McGlynn, M.O. Henry, K. Kumar, G. Hughes - Thin Solid Films 518 (2010) 4489–4492

[2]. Y. M. Lee, H. W. Yang, Journal of Solid State Chemistry 184 (2011) 615–623

[3]. Y. L. Sun., J. M. Bian, Q. W. Li, Y. M. Luo - Journal of Inorganic Materials, Vol. 25 No. 10 (2010), 115-1120

[4]. K. Yuan, X. Yin, J. Li, J. Wu, Y. Wang, F. Huang - Journal of Alloys and Compounds, Vol. 489, Issue 2 (2010), 694-699

[5]. J.J. Hassan, Z. Hassan, H. Abu-Hassan - Journal of Alloys and Compounds (2010), doi:10.1016/j.jallcom.2011.03.153
[6]. G. Kenanakis, D. Vernardou, E. Koudoumas, N. Katsarakis - J. Crystal Growth, Volume 311, Issues 23-24 (2009), 4799-4804
[7]. J. S. Huang, C. F. Lin - Nanotechnology, NANO '08. 8th IEEE Conference on Issue Date: 18-21 Aug. 2008, on page(s): 135 – 138, Arlington
[8]. M. Wang, C. H. Ye, Y. Zhang, H. X. Wang, X. Y. Zeng, L. D. Zhang - J. Phys. Chem. B, Vol. 110, No.50 (2006), 25229-25239
[9]. C. H. Ku, J. J. Wu - J. Phys. Chem. B, Vol 110, No. 26 (2006), 12981-12985
[10]. A. Sakthivelu, V. Saravanan, M. Anusuya, J.J. Prince - Journal of Ovonic Research, Vol. 7, No. 1(2011), 1-7.

THE ANNALS OF "DUNAREA DE JOS" UNIVERSITY OF GALATI.
FASCICLE IX. METALLURGY AND MATERIALS SCIENCE
N^0. 4 – 2011, ISSN 1453 – 083X

IMPROVEMENT OF PHOTOVOLTAIC CELLS EFFICIENCY BY REDUCING CONTAMINATION IN SINGLE CHAMBER PECVD SYSTEM BY PASSIVATION WITH a-Si:H AND μc-Si:H THIN FILMS*

B. DIACONU[1], A. VICENTE[2], V. MUSAT[1] AND R. MARTINS[2]
[1]Centre of Nanostructures and Functional Materials-CNMF, "Dunărea de Jos" University of Galaţi, Romania
[2]CENIMAT-I3N, Departamento de Ciência dos Materiais, and CEMOP-UNINOVA,
Faculdade de Ciências e Tecnologia da Universidade Nova de Lisboa, Portugal

ABSTRACT

High performance solar cells, deposited in a single chamber, can be obtained when low levels of contamination exists for the p-,i-,n- layers. This is a recurrent problem not only in the laboratories, but also in the industrial single chamber plasma enhanced chemical vapour deposition (PECVD) systems. In this paper an effective method of reducing the impurities, through the passivation with amorphous and nano/microcrystalline silicon thin film of the PECVD chamber walls, before and during the deposition of the solar cell layers is described.

KEYWORDS: a-Si:H, μc-Si:H, PECVD, contamination, solar cell

1. Introduction

The economically advantage of depositing solar cells in a single chamber PECVD system is obvious comparing to the multi-chamber system. The problem is the contamination during the deposition of different doped layers and this must be very seriously taken in consideration [1]. There are several causes which can lead to contamination and they can be related not only to cross contamination of p-, i-layer [2], but also due to impurities that are on the chamber walls from previous depositions or as a result of technical issues [3]. Even if the layers of the solar cells are optimized and theoretically they should lead to an efficiently working device, the contamination is a factor that can drastically reduce the performance of the solar cell. There are different methods of passivating the chamber, using different types of gases, but there is still a lot of potential for reducing the level of contamination.

Hydrogenated amorphous silicon (a-Si:H) and hydrogenated microcrystalline silicon (μc-Si:H) are intrinsic materials which bring their separate advantages for using as passivation layers [4].

2. Experimental results

The experiments took place in a single chamber PECVD system [5]. The configuration of the solar cell used for comparing the pasivation methods was glass/ZnO NW/GZO/p/i/n/Al. The passivating materials, hydrogenated amorphous silicon (a-Si:H) and hydrogenated microcrystalline silicon (μc-Si:H), were deposited using SiH_4 and H_2 gases. The choosed conditions for pasivating the PECVD chamber walls were at low pressure and low power, using hydrogen diluted silane, for the intrinsic a-Si:H material and at high pressure and high power using highly diluted silane with hydrogen, for the μc-Si:H material, to have stable materials. The intrinsic materials were deposited using VHF (27 MHz) at a substrate temperature of 200^{o}C. The deposited layers were characterized by spectroscopic ellipsometry (SE), using a Jobin Yvon UVISEL DH 10 ellipsometer and the data was simulated using Tauc-Lorentz dispersion model [6] and BEMA. The solar cells were characterized with current density versus voltage (J-V) measurements under an AM1.5 solar simulator at room temperature.

*Paper presented at the Symposium ***"The Impact of Nanotechnologies and Nanomaterials on Industrial Development and Quality of Life",*** Galati, May 19, 2011, organized by the Center for Nanostructures and Functional Materials (CNMF), Faculty of Metallurgy, Materials Sciences and Environment, "Dunarea de Jos" University of Galati

3. Results and discussion

Intrinsic a-Si:H layers deposited by pure silane SiH_4 in PECVD show high defect densities due to the short-range order at the atomic length scale[7]. These defects can be reduced to some extent if SiH4 is diluted with an optimum level of hydrogen (H_2).
An important objective is to have short passivation time deposition of intrinsic layer material, therefore is needed to obtain deposition conditions with high deposition rate while maintaining the quality of the films. It becomes difficult to achieve this objective due to the large number of parameters (pressure, substrate temperature, VHF power, frequency, etc.) that have to be optimized to obtain such conditions.

Figure 1 shows the experimental data of the growth rate for the a-Si:H films deposited using VHF SiH_4/H_2 discharges as a function of H_2 dilution.

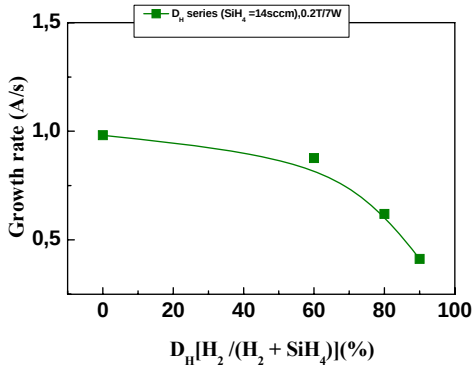

Fig 1. *The growth rate of thin films vs H_2 dilution.*

It is observable that by keeping the pressure and power constant, the growth rate predictably decreases with an increase in the H_2 dilution. This fact can be explained by the following reasons. First, the increase in H_2 leads to the displacement of plasma chemistry in favour of more atomic hydrogen as compared to reactive silicon precursors, and decreased formation of a-Si:H. Secondly, the higher amount of available H-ions creates an etching effect on the film surface. Lastly, a higher H dilution leads to lowering of electron temperature, decreasing the formation of a-Si:H. Thus, it is desirable to keep the dilution ratio at an optimum level.

The optical parameters obtained by SE provide information about the physical structure of the material [8]. The Tauc-Lorentz model was fitted to the experimental data ($\chi^2 < 1$) using a layer sample model, the AF45 glass, the bulk layer (pure a-Si:H film) and a surface layer (x% a-Si:H + y% voids). The effect of hydrogen dilution on the optical parameters for all the D_H series of samples are shown in Figure 2.

In Figure 2 one can see the evolution of the physical density parameter (A) with the D_H. This parameter A relates to the film density, thus higher the value of A, the denser (or less porous) is the material. The D_H series depicted in this plot shows a smooth increase in the A value with increasing D_H up to a certain level, while at higher dilutions (~90%), A decreases.

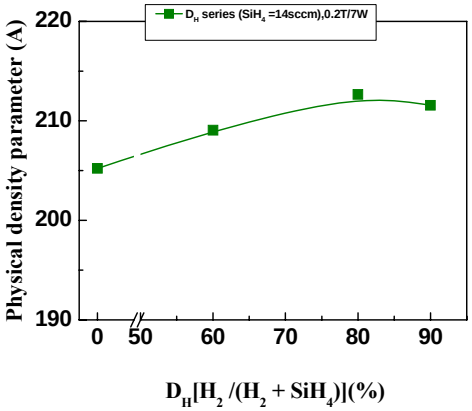

Fig 2. *Physical density parameter (A) as a function of D_H for the deposited silicon films.*

The disorder parameter in Figure 3 shows that it does not vary significantly with rise in power. For the majority of the depositions conditions, the C value stays ranges within 2.1 – 2.2, which corresponds to pure amorphous material.

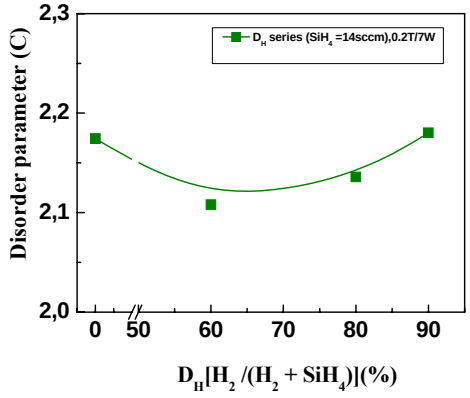

Fig 3. *The disorder parameter (C) as a function of D_H for all the deposited samples.*

µc-Si:H is a versatile material having a complex microstructure given by the effect of hydrogen dilution on the growth of microcrystalline network which is of prime importance.

In the deposition of µc-Si:H using silane diluted by H_2, a certain threshold value of the dilution ratio exists, where µc-Si:H nucleation occurs [9].

Lowering the partial pressure of silane leads to an increase in the atomic hydrogen flux density on the growing surface.

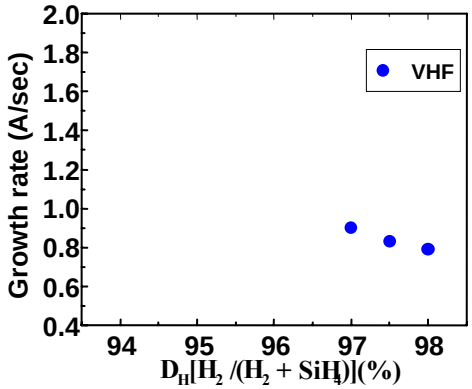

Fig 4. *Experimental results of the growth rate as a function of H_2 dilution of the films deposited from VHF at 97%, 97.5% and 98% deposition of µc-Si:H intrinsic layer.*

Thus, high hydrogen dilution or silane depletion enhances micro or nano crystalline growth. The consumption of silane exceeds the silane supply in the high power regime, and silane depletion leads to µc-Si:H growth. Thus, the atomic hydrogen density is the most crucial factor for the deposition of µc-Si:H, the optimization of which allows rapid optimization of the microstructure of the µc-Si:H material.

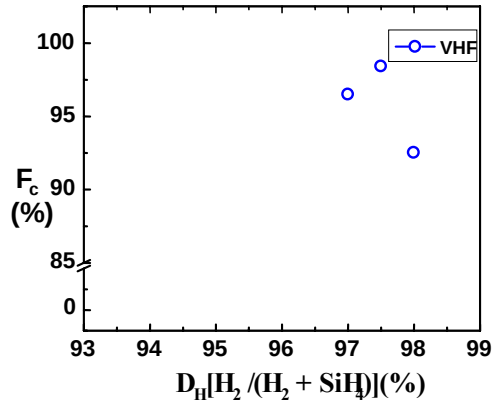

Fig 5. *Experimental results of the crystalline fraction (F_C) as a function of H_2 dilution of the films deposited from VHF.*

The chosen conditions for passivation process where:

- Intrinsic a-Si:H film was deposited using VHF (27.12 MHz) plasma decomposition of SiH_4, at a substrate temperature (Ts) of 200˚C, Pressure (P_{gas}) of 0.2 Torr, H_2 dilution (D_H=H_2/(H_2 +SiH_4) of 0% and Power (P_{vhf}) of 7 W.

- Intrinsic µc-Si:H film was deposited at P_{gas} of 2 Torr, D_H of 98% and P_{VHF} of 50W.

The growth rates of the a-Si:H and µc-Si:H layer are 0.982 Å/s and 0.792 Å/s respectively, so the time for obtaining the desired passivation thickness is comparable.

The layers deposited for passivation were a-Si:H and µc-Si:H with different thicknesses, depending on the growth time. To estimate the passivation effect of these layers on the efficiency of photovoltaic cell, two groups of cells were deposited. For the first solar cells group, the passivation was done depositing first 10 minutes of a-Si:H and then 10 minutes of µc-Si:H thin films. For the second solar cells group, the depositing time for a-Si:H was 30 minutes and for µc-Si:H was 30 minutes. All solar cells have been deposited with a pre-hydrogen glow [10], using the same p-i-n configuration with the same layers compositions. The other parameters were kept constant.

The functional characteristics for two of the deposited photovoltaic cells, belonging to each group, were measured after an annealing treatment at 150^{o}C, and the results are shown in Figures 6-7.

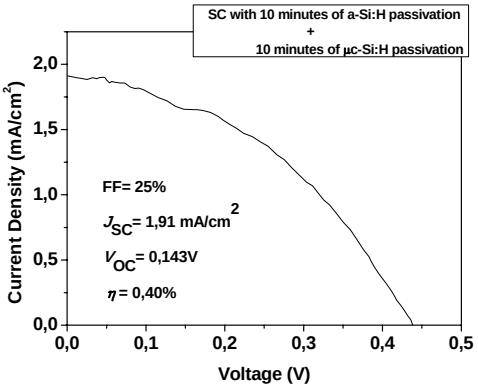

Fig 6. *I-V Curve of the photovoltaic solar cell obtained with 10 minutes a-Si:H + 10 minutes µc-Si:H passivation (first group).*

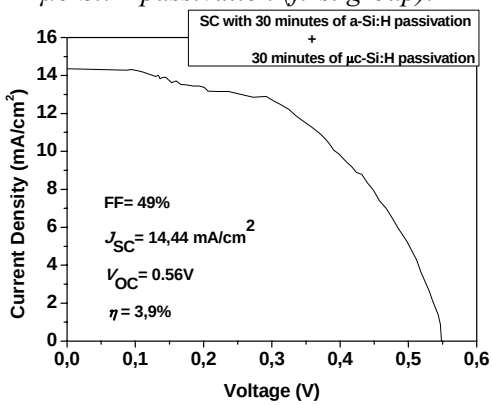

Fig 7. *I-V Curve of the photovoltaic solar cell obtained with 30 minutes a-Si:H + 30 minutes µc-Si:H passivation (second group).*

The cell obtained after the total passivation of 60 minutes (second group) has an efficiency of 3.9%, which is much better than the solar cell obtained with only a total passivation of 20 minutes. The variations of filling factor (FF), the short-circuit current (J_{SC}) and the open-circuit voltage (V_{OC}) follow the same improvement in the case of the cells deposited according to the second passivation procedure. This shows that one of the key factors for improving the efficiencies of the solar cells is the thickness of passivation layers, a-Si:H and μc-Si:H, correlated with the quality of these layers given by C (disorder) and A (compactness) parameters.

4. Conclusions

Hydrogenated amorphous silicon and hydrogenated microcrystalline silicon materials, with good stability related to growth rates, have been obtain and used as passivation layers.

The thickness of the passivation layer is an important factor for isolating the impurities that are on the walls of the single chamber PECVD system.

Photovoltaic cells with good efficiency have been developed, due to reducing contamination of PECVD chamber.

References

[1]. R. Martins, I. Ferreira, H. Águas, V. Silva, E. Fortunato, L. Guimarães - *Engineering of a-Si:H device stability by suitable design of interfaces*, Solar Energy Materials and Solar Cells, Volume 73, Issue 1, May 2002, Pages 39-49, 10.1016/S0927-0248(01)00109-X.

[2]. L. Raniero, S. Zhang, H. Águas, I. Ferreira, R. Igreja, E. Fortunato, R. Martins - *Role of buffer layer on the performances of amorphous silicon solar cells with incorporated nanoparticles produced by plasma enhanced chemical vapor deposition at 27.12 MHz*, Thin Solid Films, Volume 487, Issues 1-2, 1 September 2005, Pages 170-173, 10.1016/j.tsf.2005.01.059.

[3]. X. D. Zhang, F. H. Sun, G. H. Wang, S. Z. Xu, C. C. Wei, G. F. Hou, J. Sun, S. Z. Xiong, X. H. Geng,and Y. Zhao - *Effect of high crystalline p/i interface layer on the performance of microcrystalline silicon solar cells deposited in a single chamber system*, Phys. Status Solidi C 7, No. 3–4, 1116–1119 (2010) / DOI 10.1002/pssc.200982764.

[4]. Wang Guang-Hong, Zhang Xiao-Dan, Xu Sheng-Zhi, Zheng Xin-Xia, Wei Chang-Chun, Sun Jian, Xiong Shao-Zhen, Geng Xin-Hua, and Zhao Ying, *Reduction of the phosphorus contamination for plasma deposition of p i n microcrystalline silicon solar cells in a single chamber*, Chin. Phys. B Vol. 19, No. 9 (2010) 098102.

[5]. L. Raniero - *Produção e caracterização de células fotovoltaicas de silício nano-estruturado produzido por plasma de 27,12 MHz*, Pages 92-94 PhD thesis, Universidade Nova de Lisboa, Faculdade de Ciências e Tecnologia, Lisboa (2006).

[6]. Hiroyuki Fujiwara - *Spectroscopic Ellipsometry Principles and Applications*, Pages 170-172, John Wiley & Sons Ltd, The Atrium, Southern Gate, Chichester, West Sussex PO19 8SQ, England (2007)

[7]. R. C. Chittick, J. H. Alexander, and H. F. Sterling - The Preparation and Properties of Amorphous Silicon, J. Electrochem. Soc. 116, 77 (1969).

[8]. J. Müllerová, P. Šutta, G. van Elzakker, M. Zeman, M. Mikula - *Microstructure of hydrogenated silicon thin films prepared from silane diluted with hydrogen,* Applied Surface Science, Volume 254, Issue 12, 15 April 2008, Pages 3690-3695, 10.1016/j.apsusc.2007.10.069.

[9]. R.E.I. Schropp, J.K. Rath, H. Li - *Growth mechanism of nanocrystalline silicon at the phase transition and its application in thin film solar cells*, Journal of Crystal Growth, Volume 311, Issue 3, 15 January 2009, Pages 760-764, 10.1016/j.jcrysgro.2008.09.155.

[10]. Xiaodan Zhang, Guanghong Wang, Xinxia Zheng, Changchun Wei, Xinhua Geng, Shaozhen Xiong, Ying Zhao - *A pre-hydrogen glow method to improve the reproducibility of intrinsic microcrystalline silicon thin film depositions in a single-chamber system*, Solar Energy Materials and Solar Cells, Volume 95, Issue 8, August 2011, Pages 2448-2453.

THE ANNALS OF "DUNAREA DE JOS" UNIVERSITY OF GALATI.
FASCICLE IX. METALLURGY AND MATERIALS SCIENCE
N^0. 4 – 2011, ISSN 1453 – 083X

RELATIVE PERFORMANCE OF Ca, Ba-FeSi INOCULANTS TO CHILL CONTROL IN LOW-S GREY CAST IRONS

Costin Bogdan ALBU, Iulian RIPOSAN*
Politehnica University of Bucharest
*Corresponding Author
email: riposan@foundry.pub.ro

ABSTRACT

Low sulphur irons (< 0.05%S) production is more and more promoted in many parts of the world, as small and less efficient cupolas were replaced by the new generation of induction furnaces, while a single low sulphur base iron is very attractive for grey/ductile/compacted irons production. The problem is that at low S-levels, grey irons usually solidify with high eutectic undercooling, favorable for carbides formation, especially in thin wall castings (automotive industry). Relative performance of different Ca, Ba and Al bearing FeSi alloys was calculated to evaluate their efficiency to control chill tendency, in critical base irons [< 0.035%S, (%Mn) x (%S) < 0.02, 0.002%Al]. Relative clear/mottled/total chill measurement criteria were applied, for chill wedges with different cooling modulus (CM = 0.11 – 0.35 cm). The results showed that some inoculants performed better than the other alloys bearing the same base inoculating elements and have different positions for different chill evaluation criteria and wedge size (cooling modulus) parameters reference. An optimum association of Ca, Ba and Al contents at a proper Ba/Ca ratio is more efficient comparing to the increasing of the inoculating elements leveling FeSi-based alloys for inoculation of lower sulphur, electrically melted irons.

KEYWORDS: Grey iron, Low S, Cooling rate, Inoculation, Ca, Ba, Al, Structure, Carbides, Graphite

1. Introduction

Inoculation is a treatment of the molten iron to control the structure and properties of castings by promotion of active nucleation sites available for the growth of graphite flakes in grey irons at lower eutectic undercooling, thereby minimizing the risk of forming chill (hard iron carbides) and/or un-favourable graphite morphologies, such as D-type (undercooled) graphite, particularly in thin sections.

Chilled structures are typically for high eutectic undercooling and are hard and brittle and interfere with machining, necessitate additional heat treatment operations, resulting in non-conformance with specifications and, in general, increase the total cost of production.

Lowering the eutectic undercooling may lead to avoiding of carbides, but, if it is still high, the promoted graphite will branch, forming abnormally patterns, such as Types B, D and E graphite.

At enough lower eutectic undercooling level, random graphite flakes form uniformly in the iron matrix, which is known as Type A graphite.

The most effective inoculants are FeSi alloys containing small amounts of one or more of the elements such as Ca, Ba, Sr, generally at concentrations above 0.5wt.% each one. It is considered that inoculating elements contents above 1.5wt.% give improved inoculation under some conditions but may also give a greater tendency to produce slag [1, 2].

Recent research results have identified three groups of elements with important contributions in formation of graphite nucleation sites as (Mn,X)S - type in commercial grey cast iron: (a) oxide forming elements (Mn, Si, Al, Zr etc) to produce small oxide base sites (usually less than 3μm) in the first stage; (b) Mn and S to sustain MnS-compounds (generally up to 10 μm size) nucleated by stage one particles; (c) inoculating elements, such as Ca, Ba, Sr, Ce, La etc which act in the first stage or/and in the second stage

of graphite formation, to improve the capability of (Mn,X)S compounds to nucleate graphite [3-5].

The nucleation of graphite flakes on MnS particles was also confirmed by microstructure simulations [6, 7].

Traditionally, the sulphur level in grey iron was above 0.05%, as the cupola was the typical melting furnace in the cast iron foundries, where the metallurgical coke acts as an efficient re-sulphurizer of the iron melt, but with excessive contribution in many cases.

The new generation of coreless induction furnaces replaced cupolas in the iron melting shops (no metallurgical coke), the expensive pig iron was replaced by steel scrap (lower sulphur), while the high quality carbon riser (lower sulphur) is more and more used, inclusively in grey iron production.

Consequently, less than 0.05%S content is typically now for the base iron in high performance grey iron castings production. The re-sulphurization of the iron melt to attend a control factor at (%Mn) x (%S) = 0.03-0.05 level [8] is necessary, but in some cases this is not possible, as ecology limitation or for the necessity to use the same base iron for grey/compacted/ductile irons castings production.

The problem is that at low S-levels, grey irons usually solidify with high eutectic undercooling, favourable for carbides and / or undercooled graphite morphologies, especially in thin wall castings (automotive industry) [9-13]. Lower residual aluminium content in the iron melt (less than 0.004%Al), also typically for the acid lining coreless induction furnaces melting increases the difficulty of (Mn,X)S compounds formation [3-5, 10, 13].

Grey irons with sulphur contents below about 0.05% may only respond to certain specialized inoculants, or necessitate the increasing of the inoculant addition rate, but promoting some detrimental effects, such as the increasing of slag defects. Recently, a strong research activity was recorded, to improve the chemical composition of FeSi-based inoculants, in order to increase their inoculation capability according to low sulphur grey iron characteristics.

New inoculating elements were considered, especially from rare earth (RE) group (Ce, La), or some elements were associated with traditionally inoculating elements, such as Zr + Sr, Zr + Ca or RE + Ca. The review of the conventional inoculants composition was also considered, in order to optimize inoculant's chemistry according to the new conditions of the grey iron melt.

The current experimental investigation in the paper was designed to evaluate the relative performance of the Ca, Ba and Al bearing FeSi alloys at different association of inoculating elements as efficiency in chill control of grey iron; a critical iron chemistry [< 0.035%S, (%Mn) x (%S) < 0.02, 0.002%Al] for graphite nucleation was also considered, for solidification in different cooling rate conditions.

2. Experimental procedure

Experimental heats at low sulphur level (0.030-0.035%S) and very low residual aluminium content (0.002%Al) were produced in an acid lined coreless induction furnace (100kg, 2400Hz). Un-inoculated and ladle inoculated (0.15wt.% Ca,Ba,Al-FeSi alloys) were considered, at the following final chemical compositions (wt.%): 3.25-3.35C, 1.60-1.65Si, 0.55-0.56Mn, 0.08-0.11P, 0.09-0.10Cu, 0.03-0.04Ni, 0.08-0.09Cr, 0.01Mo, 0.005V, 0.005-0.006Ti, for carbon equivalent (CE) 3.75-3.85, and (%Mn) x (%S) = 0.017-0.020 as control factor.

Different Ca, Ba, Al-FeSi alloys were used, for the 70-75wt.%Si range and appropriate aluminium contents (0.7-0.9wt.%), typically for foundry grade ferrosilicon, but at different inoculating elements (Ca, Ba) levels. The traditionally Ca and Ba inoculating elements were included in the usual range for the commercial inoculants (up to 4wt.% each one), but varied as Ba/Ca ratio (0.8-4) and content associations, for Ca + Ba = 1.7-6.2wt.% in the inoculants chemistry.

The iron melt was heated up to 1530-1540^{o}C for 10 minutes, and then was tapped into the inoculation ladle (10 kg). Inoculants were added, at 0.2-0.7 mm grain size during tapping into the pouring ladle. Inoculated irons were poured (furan resin moulds) at a strong controlled temperature (1350^{o}C) after a 2.0-2.5 min holding time.

The very narrow chemistries range of the tested irons and very low minor (trace) elements contents, the strong control on the thermal regime and treated iron melt volume, and controlled compositions and grain sizes of the inoculants led to an accurate evaluation of the inoculants effect, inclusively as the Ba/Ca ratio influences. Wedge W_1, W_2 and W_3 samples according to ASTM A367, were used (furan resin mould) as "Test Method A-Wedge". Standard wedges are characterized by size and cooling modulus (CM), which involved different solidification cooling rates, for the same pouring practice and moulding media. For the three considered wedges, representative for thin-medium wall thickness castings, the main characteristics are the follows: W_1 (B=5.1mm base width, 25.4mm height, CM=0.11cm cooling modulus), W_2 (10.2mm base width, 31.8mm height, CM=0.21cm) and W_3 (18.6mm base width, 38.1mm height, CM=0.35cm). Cooling modulus (CM) is defined as the ratio between volume and the total external casting surface and is an expression of the capacity to transfer a given quantity of heat

through an existing surface to the mould. Higher cooling modulus equates to slower cooling rate and lower undercooling during eutectic solidification.

3. Results and discussion

The measurement of chill was recorded according to a controlled procedure, to avoid hot shaking effect on the solid state transformation. Later the wedges were fractured and their fractures analyzed. That portion nearest the apex, entirely free of grey (graphite) areas, is designated as the clear chill zone (W_c), including only carbides in the structure ***(Fig. 1)***.

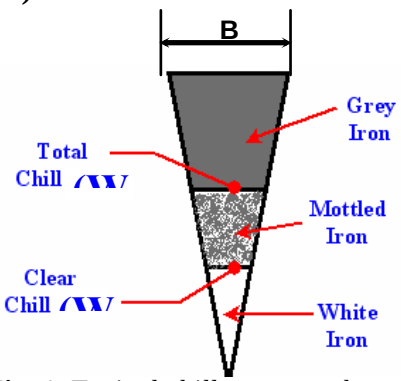

Fig. 1. *Typical chill zones on the wedge test samples [B-base width].*

The portion from the end of the clear chill zone to the location where the last presence of cementite, or white iron is visible, is designated the mottled zone (W_m), including both carbides and graphite. The region from the junction of grey fracture (no carbides, only graphite) to the first appearance of chilled iron (apex) is designated the total chill (W_t).

The parameters relative clear chill (RCC), relative total chill (RTC) and relative average mottled chill (RMC) were also considered:

$$RCC = 100\ [W_c / B]\ (\%) \quad (1)$$
$$RTC = 100\ [W_t / B]\ (\%) \quad (2)$$
$$RMC = 100\ [0.5\ (W_c + W_t) / B]\ (\%) \quad (3)$$

where B is the maximum width of the test wedge.

Table 1 summarized the obtained results for the three chill evaluation criteria (RCC, RMC, RTC), of un-inoculated and different inoculated irons (A….I inoculants).

The increasing of the cooling modulus (CM) from W_1 (CM=0.11cm) through W_2 (0.21cm) up to the W_3 (0.35cm) led to the decreasing of the cooling rate, and, normally, also of the chill tendency of both un-inoculated and inoculated irons. Un-inoculated irons are characterized by having high chilling tendency. It could be considered as excessive for 3.75-3.85%CE irons.

Table 1*. Relative clear (RCC), mottled (RMC) and total (RTC) chill*

Alloy	Ca+Ba (%)	Ba/Ca	W_1 [B=5.3mm; CM=0.11cm]			W_2 [B=10.2mm; CM=0.21cm]			W_3 [B=18.6mm; CM=0.35cm]		
			RCC (%)	RMC (%)	RTC (%)	RCC (%)	RMC (%)	RTC (%)	RCC (%)	RMC (%)	RTC (%)
U.I	-	-	100	100	100	100	99.0	98.0	51.5	75.8	100
A	1.70	0.89	55.5	77.8	100	34.0	66.0	98.0	20.0	34.0	48.0
B	2.01	0.62	64.5	82.3	100	36.0	67.0	98.0	24.0	39.3	54.5
C	2.22	1.00	50.5	75.3	100	30.5	64.3	98.0	20.0	35.0	50.0
D	2.40	1.40	52.0	76.0	100	30.5	64.3	98.0	18.5	33.5	48.5
E	2.97	2.06	48.5	74.3	100	33.0	65.5	98.0	20.0	36.0	52.0
F	3.85	3.53	62.5	81.3	100	37.0	50.5	64.0	20.0	33.5	47.0
G	3.85	1.08	55.5	77.8	100	29.0	63.5	98.0	18.7	33.9	49.0
H	4.55	1.76	54.5	77.3	100	34.0	51.8	69.5	17.0	31.5	46.0
I	6.20	1.82	59.5	79.8	100	35.0	52.3	69.5	19.5	33.8	48.0
Average	CL_K		**55.9**	**78.0**	**100.0**	**33.2**	**60.6**	**87.9**	**19.7**	**34.5**	**49.2**
St. Dev.	S_K		**5.38**	**2.70**	**0.00**	**2.72**	**6.88**	**15.25**	**1.89**	**2.17**	**2.62**

High furnace superheating (1540^{o}C), low Al content (0.002%) and less than 0.02 as (%Mn) x (%S) control factor led to difficulties in complex (Mn,X)S compounds formation, as graphite nucleation sites, and, consequently, to excessive chill. Inoculation gave, as expected, overall lower iron chill than with no inoculation, even at lower inoculant (0.15wt.%) in-ladle additions. A 0.15wt.% inoculant addition had a very big influence on chill tendency compared to un-inoculated irons, especially at the higher cooling rate (or lower cooling modulus of wedge samples). At low cooling modulus (CM=0.11cm, W_1 samples), typically for thin wall castings (4.4mm corresponding diameter for a bar sample), an important inoculation

effect was obtained for relative clear chill (RCC) evaluation, as RCC decreased from 100% to 50-65%, much more than for relative mottled chill RMC (from 100% to 75-85%), while the relative total chill RTC was not affected. W_2 type wedges are representative for 8.4 mm diameter bars castings, large used in mechanical engineering. Inoculation was more effective for these castings as relative clear chill evaluation, comparing to relative mottled chill and especially to relative total chill evaluation, where only some inoculants were efficient. The largest considered wedge sample (W_3), correspondent to 14mm diameter bar castings is visible affected by inoculation for all of chill evaluation criteria and inoculants used.

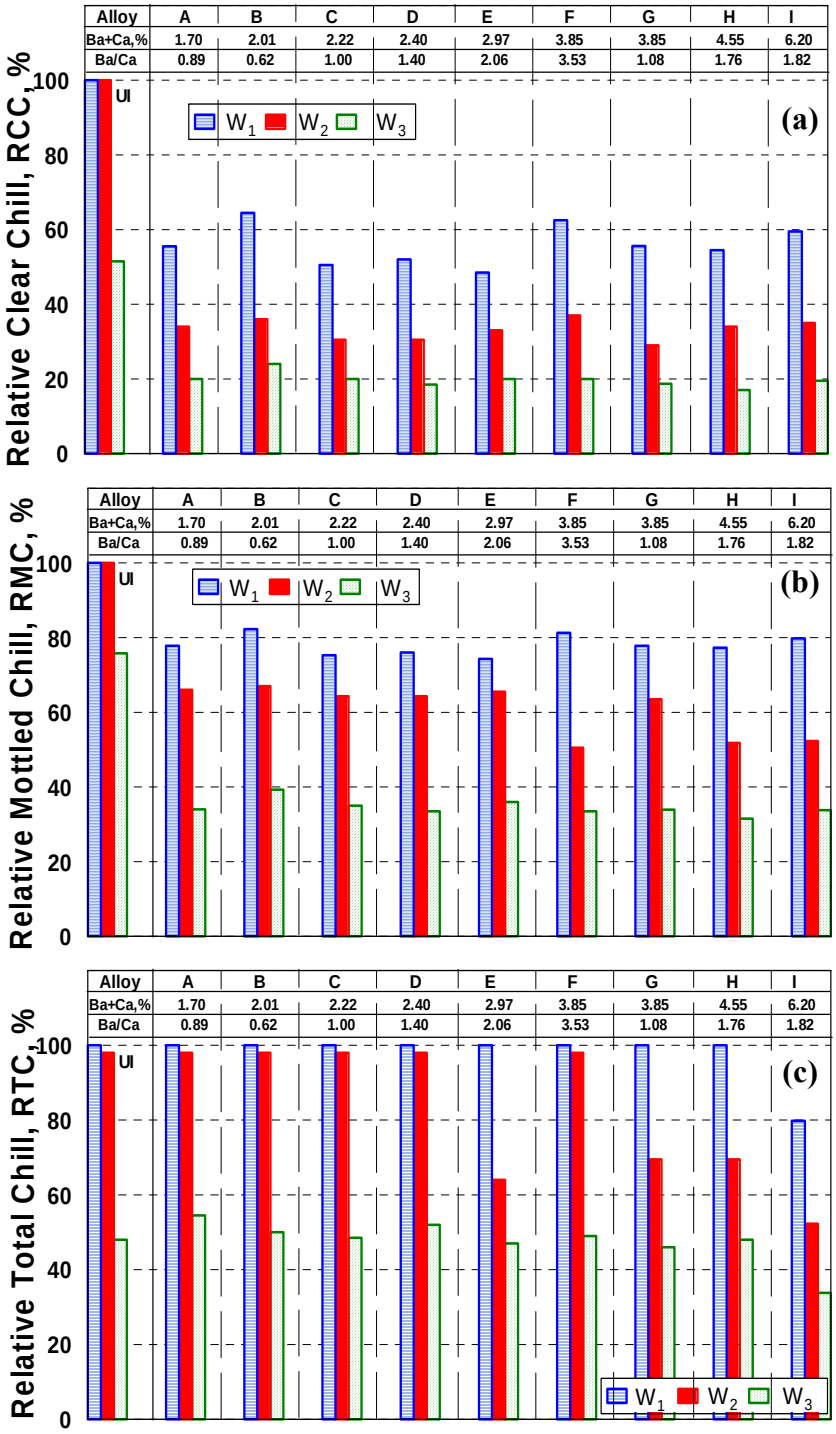

Fig. 2. *Relative clear chill (RCC) (a), relative mottled chill (RMC) (b) and relative total chill (RTC) (c) of un-inoculated (UI) and inoculated (A….I) irons, for W_1, W_2 and W_3 samples.*

A number of trends in chill sensitivity could be identified, as the influence of inoculating elements (Ca, Ba) total sum and especially as ratio, specific content of each element and their associations (***Fig. 2***).

Generally, the increasing of the total content of inoculating elements (Ca + Ba sum) in the compositions of Ca,Ba,Al-FeSi alloys does not appear to have an important beneficial influence as chill tendency decreasing of the low sulphur and low aluminium, electrically melted grey irons, with some peculiar exceptions.

It is more visible for intermediary solidification conditions, such as for W_2 (CM=0.21cm) samples and for relative mottled chill (RMC) evaluation criteria, respectively. The relative performance of inoculants to control representative chill tendency parameters was calculated to determine the efficiency of the experimental alloys [14].

The relative performance (RPi) of inoculants –i- is estimated as:

$$RPi = \frac{\sum_k (X_{ik} - CL_k)}{S_k} \quad (4)$$

where X_{ik} is measured value of property –k- using inoculants –i-;

CL_k is average value for property set –k-;

S_k is standard deviation from the set.

The reducing of chill tendency performance is averaged and used as one parameter –*k*-, for each chill evaluation criteria (RCC, RMC, RTC) and each wedge samples (W_1, W_2, W_3). Average performance has level 0%.

The performances of inoculants increase as chill tendency decreases, so positive values for relative performance ***(Tables 2 and 3, Figures 3 and 4)*** means a lower chill comparing to the average level for the group of considered alloys. This tool was used to determine and distinct the close performance of the alloys in all the analyses carried out in this work.

The results showed that some inoculants performed better than the other alloys bearing the same base inoculating element (Ca and Ba), depending on the total Ca + Ba content and the ratio of the two inoculating elements (Ba / Ca), respectively. Inoculants have different positions for different chill evaluation criteria (RCC, RMC, RTC) and wedge size (cooling modulus) parameters.

Thin wall castings (< 5mm wall thickness), represented here by W_1 wedge sample (0.11cm cooling modulus and corresponding to 4.4mm diameter bars), are the most affected by different alloys chemistries.

Table 2. *Relative performances of Ca,Ba-FeSi alloys to reduce chill tendency*

Alloy	Ca+Ba (%)	Ba/Ca	W_1 [B=5.3mm; CM=0.11cm]			W_2 [B=10.2mm; CM=0.21cm]			W_3 [B=18.6mm; CM=0.35cm]		
			RCC (%)	RMC (%)	RTC (%)	RCC (%)	RMC (%)	RTC (%)	RCC (%)	RMC (%)	RTC (%)
A	1.70	0.89	+7.2	+7.0	0.0	-28.6	-78.9	-66.3	-13.5	+23.1	+46.6
B	2.01	0.62	-159.9	-159.9	0.0	-102.2	-93.4	-66.3	-225.1	-221.3	-201.2
C	2.22	1.00	+100.1	+99.7	0.0	+100.2	-54.1	-66.3	-13.5	-23.1	-29.6
D	2.40	1.40	+72.2	+73.8	0.0	+100.2	-54.1	-66.3	+65.8	+46.1	+27.5
E	2.97	2.06	+137.2	+136.8	0.0	+8.2	-71.6	-66.3	-13.5	-69.2	-105.9
F	3.85	3.53	-122.8	-122.8	0.0	-139.0	+146.6	+156.7	-13.5	+46.1	+84.7
G	3.85	1.08	+7.2	+7.0	0.0	+155.4	-42.5	-66.3	+55.2	+27.7	+8.5
H	4.55	1.76	+25.8	+25.5	0.0	-28.6	+127.7	+120.6	+145.1	+138.3	+122.8
I	6.20	1.82	-67.1	-67.2	0.0	-65.4	+120.4	+120.6	+12.9	+32.3	+46.6

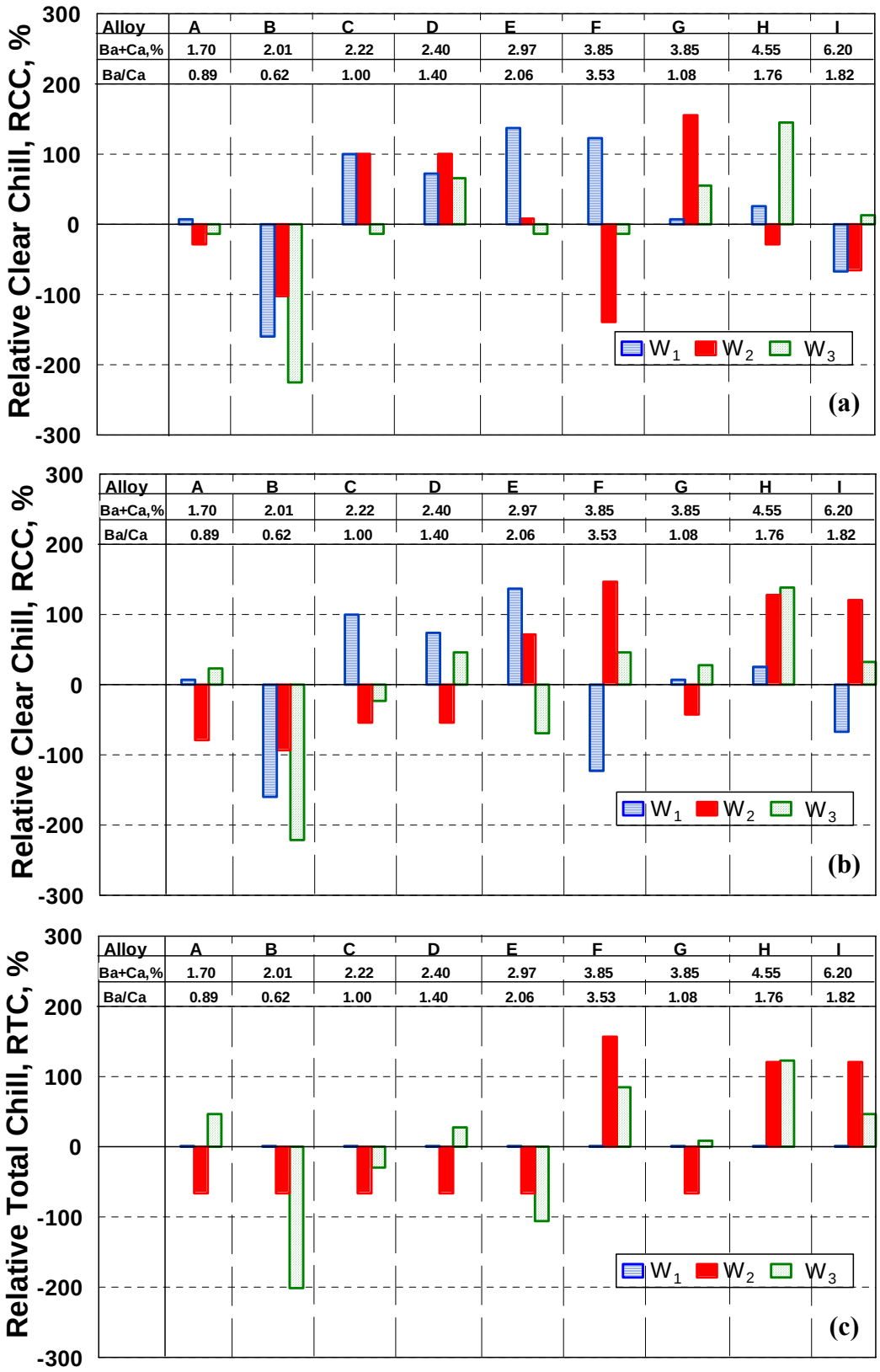

Fig. 3. *Relative performance as chill tendency decreasing of Ca,Ba-FeSi alloys for W_1, W_2 and W_3 wedge samples, as relative clear chill (RCC) (a), relative mottled chill (RMC) (b) and relative total chill (RTC) (c) evaluation criteria.*

Table 3. *Relative performances of inoculants as chill evaluation criteria and wedge size*

Alloy	Ca+Ba (%)	Ba/Ca	Chill evaluation criteria				Wedge samples			
			RCC	RMC	RTC	Total	W_1	W_2	W_3	Total
A	1.70	0.89	-11.6	-16.3	-6.6	-11.5	+4.7	-57.9	+18.7	-11.5
B	2.01	0.62	-162.4	-158.2	-89.2	-136.6	-106.6	-87.3	-215.9	-136.6
C	2.22	1.00	+62.3	+7.5	-32.0	+12.6	+66.6	-6.7	-22.1	+12.6
D	2.40	1.40	+79.4	+21.9	-12.9	+29.5	+48.7	-6.7	+46.5	+29.5
E	2.97	2.06	+44.0	-1.33	-57.4	-4.9	+91.33	-43.2	-62.9	-4.9
F	3.85	3.53	-91.8	+23.3	+80.5	+4.0	-81.9	+54.8	+39.1	+4.0
G	3.85	1.08	+72.6	-2.6	-19.3	+16.9	+4.7	+15.5	+30.5	+16.9
H	4.55	1.76	+47.4	+97.2	+81.1	+75.2	+17.1	+73.2	+135.4	+75.2
I	6.20	1.82	-39.9	+28.5	+55.7	+14.8	-44.8	+58.5	+30.6	+14.8

In clear chill (white iron structure, no graphite presence) control, the highest performance characterized Ca,Ba,Al-FeSi alloys at medium inoculating elements content [2-3% (Ca + Ba)] and Ba/Ca = 1 - 2 ratio.

The increasing of the inoculating elements content does not appear to be an economical solution for these irons, independently of their ratio in the chemical composition of these complex alloys. The same behaviour appears in relative mottled chill evaluation (mixture of carbide and graphite zone size), while for total chill control (RTC) these inoculants have not enough power in tested conditions.

Thin to medium size wall thickness castings characterized by W_2 wedge sample (0.21cm cooling modulus, corresponding to 8.4mm diameter bars) present different requirements for Ca,Ba,Al-FeSi alloys as chill control, depending on the chill evaluation criteria.

As clear chill approach, the ratio of the two inoculating elements appears to be the most important parameter. The best performance characterized inoculants with Ca and Ba in a relative equilibrium (Ba/Ca = 1.0-1.5), at medium (2.2-2.5%) or high (3.85%) total content of Ca and Ba. In the both chemistry ranges, lower or higher Ba/Ca ratio visible decreased the performance of these inoculants. Mottled and total chill control in these castings required inoculants with higher content of inoculating elements, generally more than 4%.

W_3 wedge sample usually characterizes medium size (more than 10mm wall thickness) castings. Also in this case the ratio of the two inoculating elements is important, as the higher performance inoculants are generally characterized by Ba/Ca = 1.5-2.0 ratio, mainly at more than 4% total content.

Generally, in low sulphur grey cast irons, the higher is the wall thickness (cooling modulus) of castings, the higher is the content of inoculating elements necessary for higher performance of inoculants in Ca-Ba system.

In critical solidification condition, such as thin wall castings, the performance of Ca-Ba bearing FeSi alloys is better for an equilibrium of Ca and Ba contents, the best position is typically for 3% (Ca + Ba) and Ba/Ca = 2 ratio alloy, which performed better than the other alloys, inclusively at higher content of inoculating elements. The high calcium and barium bearing inoculants did not perform well during fast casting of small samples under the conditions in this trial.

Independently of wedge size and chill evaluation criteria, less than 2% (Ca + Ba) and Ba/Ca < 1.0 ratio are not recommended in low sulphur grey cast irons, with critical conditions for graphite nucleation at lower eutectic undercooling.

As iron castings are usually complex parts, at a large range of wall thickness, including from thin (some millimeters) up to thick (hundreds millimeters) walls, it is very difficult to select a performance inoculant to control the structure in so different solidification conditions.

Figure 4 shows the total relative performance of the tested alloys, for a large range of cooling modulus (0.11-0.35cm) and different chill evaluation criteria.

The best performance inoculant to produce a high quality complex grey iron castings (large wall thickness variation) is characterized by 4.5% (Ca + Ba) total content at 1.75 specific Ba/Ca ratio, while the second variant refers to an alloy at lower but controlled content of the two representative inoculating elements: Ca + Ba = 2.4% and Ba/Ca = 1.4.

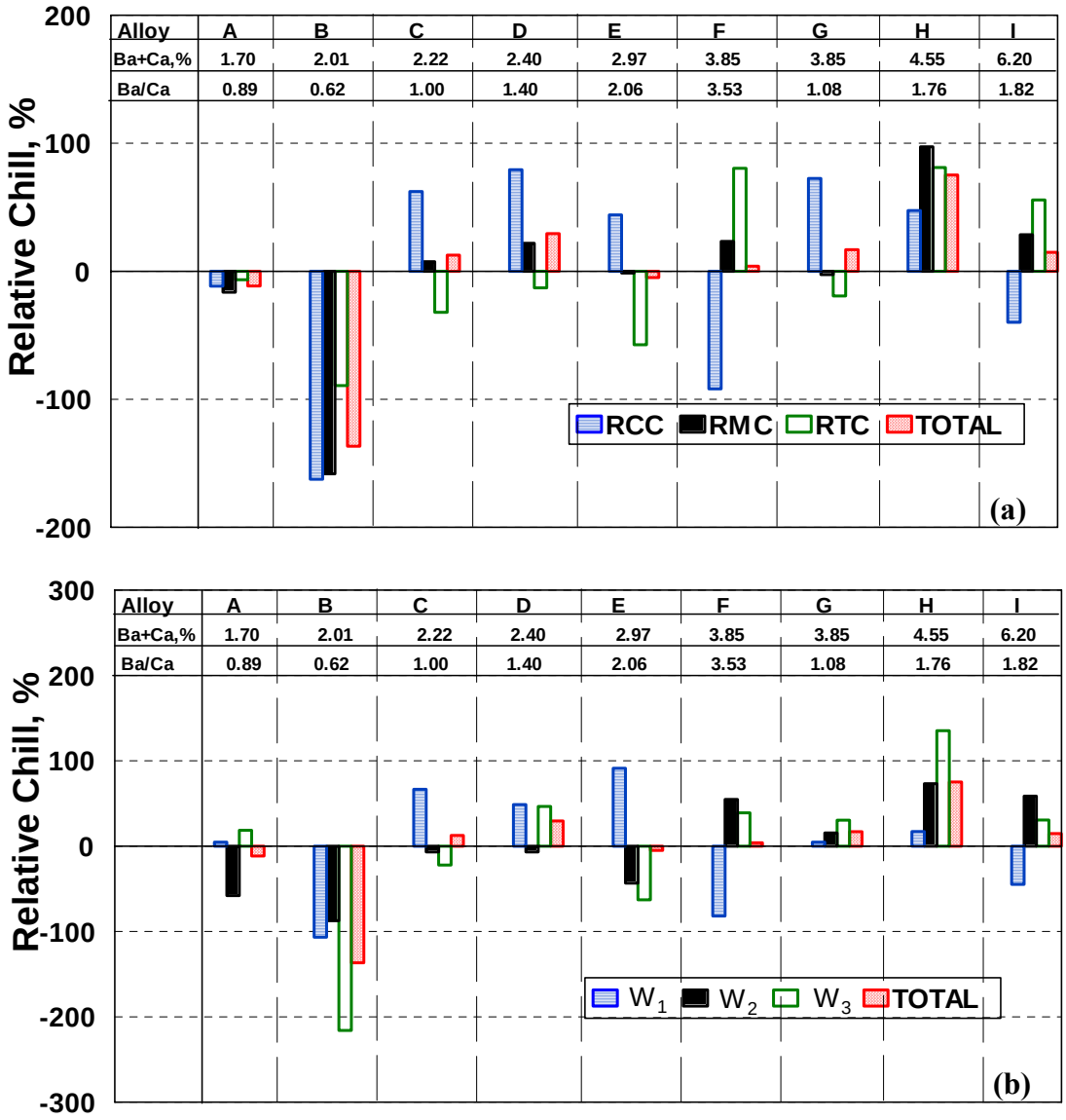

Fig. 4. *Relative performance as chill tendency decreasing of Ca, Ba, Al-FeSi alloys for different chill evaluation criteria (a) and different wedge sample size (b).*

4. Summary

The relative performance of Ca,Ba,Al-FeSi alloys, at different association of inoculating elements (Ca, Ba), was tested in chill control in low S grey irons (< 0.035%S) for different solidification cooling rates (W_1, W_2 and W_3 wedges, ASTM A 367) and chill evaluation criteria (RCC, RMC, RTC). Based on this work the following main conclusions can be drawn.

- Chill tendency of electrically melted base iron having 3.75%CE, 0.03%S, (%Mn) x (%S) < 0.02 control factor and 0.002%Al residual is excessively high, demonstrating a relatively high need for inoculation power.
- The results showed that some inoculants performed better than the other alloys bearing the same base inoculating element (Ca and Ba), depending on the total Ca + Ba content and the ratio of the two inoculating elements (Ba/Ca), respectively.
- Un-favourable chemical composition of the inoculated irons as Mn, S and Al contents for (Mn,X)S compounds formation to act as graphite nucleation sites is difficult to be covered by increasing of inoculating elements (Ca, Ba) content, especially for high cooling rate solidification and clear chill parameter control.

- Inoculants have different positions for different chill evaluation criteria (RCC, RMC, RTC) and wedge size (cooling modulus) parameters reference.
- Independently of wedge size and chill evaluation criteria, less than 2% (Ca + Ba) and Ba/Ca < 1.0 ratio are not recommended in low sulphur grey cast irons, with critical conditions for graphite nucleation at lower eutectic undercooling.
- In thin wall castings production, the performance of Ca-Ba bearing FeSi alloys is better for an equilibrium of Ca and Ba contents, the best position is typically for 3% (Ca + Ba) and Ba/Ca = 2 ratio alloy, which performed better than the other alloys, inclusively at higher content of inoculating elements.
- The best performance inoculant to produce a complex grey iron castings (large wall thickness variation) is characterized by 4.5% (Ca + Ba) total content at 1.75 specific Ba/Ca ratio, while the second variant refers to an alloy at lower but controlled content of the two representative inoculating elements: Ca + Ba = 2.4% and Ba/Ca = 1.4.
- The use of relative performance of inoculants is a tested tool to determine and distinct the close performance of the alloys in all the analyses carried out in this work.

References

[1]. ****Cast iron inoculation* - The Technology of Graphite Shape Control Brochure, www.foundry.elkem.com, May 2009.

[2]. ****ELKEM Technical Information 3*, ELKEM ASA, Foundry Products, www.foundry.elkem.com, 2004.

[3]. I. Riposan, M. Chisamera, S. Stan, T. Skaland, M.I. Onsoien - *Analyses of Possible Nucleation Sites in Ca/Sr Overinoculated Grey Irons.* AFS Trans., 2001, Vol. 109, pp. 1151-1162.

[4]. I. Riposan, M. Chisamera, S. Stan, T. Skaland - *Graphite Nucleants (Microinclusions) Characterization in Ca/Sr Inoculated Grey Irons.* Int. J. Cast Met. Res., 2003, Vol. 16, No. 1-3, pp.105-111.

[5]. I. Riposan, M. Chisamera, S. Stan, C. Hartung, D. White - *Three-Stage Model for the Nucleation of Graphite in Grey Cast Iron.* Mater. Sci. Techn., 2010, Vol. 26, No. 12, pp. 1439-1447.

[6]. A. Sommerfeld, B. Bottger, B. Tonn - *Graphite Nucleation in Cast Iron Melts Based on Solidification Experiments and Microstructure Simulation.* J. Mater. Sci. Techn., 2008, Vol. 24 (3), pp. 321-324.

[7]. A. Sommerfeld, B. Tonn - *Nucleation of Graphite in Cast Iron Melts Depending on Manganese, Sulphur and Oxygen.* Int. J. Cast Metal Res., 2008, Vol. 21 (1-4), pp. 23-26.

[8]. R. Gundlach - *Observations on Structure Control to Improve the Properties of Cast Irons*. The 2008 Honorary Cast Iron Lecture, Div. 5, AFS Metalcasting Congress, Atlanta, Georgia, USA, Paper 08-158.

[9]. R.L. Naro, J.F. Walace - *Trace elements in cast irons*. AFS Trans., 1969, Vol. 77, p. 311; 1970, Vol. 78, p.229 ; AFS Cast Met. Res. J., Sept. 1970, p.131.

[10]. M. Chisamera, S. Stan, I. Riposan, G. Costache, M. Barstow - *Solidification Pattern of In-Mold and Ladle Inoculated Low Sulfur Hypoeutectic Gray Irons.* AFS Trans., 2008, Vol. 116, pp. 641- 652.

[11]. C.R. Loper Jr. *Inoculation of Cast Iron-Summary of Current Understanding*. AFS Trans., 1999, Vol. 107, pp. 523-528.

[12]. M. Chisamera, I. Riposan, S. Stan, T. Skaland - *Undercooling, Chill Size, Structure Relationship in Ca/Sr Inoculated Grey Irons under Sulphur/Oxygen Influence*. 64th World Foundry Congress, Paris, France, Sept. 11-14, 2000, Paper RO-62.

[13]. M. Chisamera, I. Riposan, S. Stan, D. White, G. Grasmo - *Graphite Nucleation Control in Grey Cast Iron.* Int. J. Cast Metal Res., 2008, *Vol.* 21 (1-4), pp. 39-44.

[14]. I. Riposan, M. Chisamera, S. Stan, P.Toboc, D. White, C. Ecob, C. Hartung - *Al Benefits in Ductile Iron Production.* J. Mater. Eng. Perform., 2011, Vol. 20 (1), pp.57 – 64.

THE ANNALS OF "DUNAREA DE JOS" UNIVERSITY OF GALATI.
FASCICLE IX. METALLURGY AND MATERIALS SCIENCE
N^0. 4 – 2011, ISSN 1453 – 083X

MATHEMATICAL MODELLING OF THE MAIN CARBURIZING THERMOCHEMICAL TREATMENT PARAMETERS INFLUENCE ON THE SURFACE HARDNESS PARTS MADE IN AMS 6265 (SAE 9310) STEEL

Dorin PĂUN
S.C.Turbomecanica S.A. Bucharest
email: dorin.paun@turbomecanica.ro

ABSTRACT

This work is a part of broader experimental research study on the influence of the main process parameters (thermal, temporal and chemical of carburizing thermochemical treatment on the level of the main microstructural features, chemical and physical-mechanical properties values, resulted to the carbon hardening process of the AMS 6265 (SAE 9310) steel parts used in the aeronautical industry. This paper treats only those aspects concerning the influence of these three key parameters temperature, T_K, maintaining time, t_K, and carbon potential, C_{potK} on the surface hardness parts, HRC_{SUP}. The originality of this work lie in the approach of the experimental study using the active experiment scheduled method with the second order of noncompositional programming.

KEYWORDS**:** carburizing; surface hardness; the active experiment scheduled method; programming matrix

1. Introduction

The complexity of the phenomena involved in the thermochemical treatments excludes to study these processes with the classical experimental methods, which are characterized by major difficulties in implementation and in most cases, do not lead to reliable results. The solving problems in the experimental researching processes, which are based on diffusion phenomena using experimental method, required to apply the scheduled experimental methods which permit to realize the empirical mathematical models which can be obtained either by passive or by active experiment methods [1].

The most information that are presented in the literature, concerning the AMS 6265 steel, used in aeronautical industry, characterize it more in terms of its performance of mechanical characteristics that can be obtained by using it to implement the execution of parts hardened by thermochemical treatment using the carbon as cement , without making reference on the concrete ways in which these performances can be obtained, often spectacular.

The majority of the works in the field of thermochemical treatments research present the information concerning the relatively modest performance of carbon hardened AISI 8620 steel, with low alloying elements [2, 3]. This is why the present work, detached from a broader study on the carburizing treatment of components made from this steel, aim to fill some of these goals information about the specific aspects of the carburizing process of the AMS 6265 steel parts, respectively, how the main process parameters influence the actual Rockwell hardness surface parts.

For carburized AMS 6265 parts steel, used in aeronautical industry are imposed the high wear and toughness features because they are used to perform components for gears who must face in terms of accidental demands (overload).

2. Experimental conditions

2.1. The study of the thermal, temporal and chemical parameters influence on the surface hardness parts using the active experimental scheduled method and the second order noncompositional programming

Existing knowledge about the processes that are based on the diffusion phenomena generally required that, for explicit the interactions between process parameters (independents parameters) and their

effects on the level variation of structural features and the respective values of physical and mechanical characteristics (dependent parameters), to resort to use the second order noncompositional programming [4] The reason for using this type of programs consists on one side in the fact that the processes underlying the formation of diffusion layers can not be mathematically defined using linear models [5, 6] and on the other side, there are sufficient knowledge concerning the range where can be found the interest values.

In order to solve this type of problem it is necessary to explicit the experimental data using the second-order nonlinear equations of the form:

$$Y = b_0 + \sum_{\substack{i=1 \\ 1\le i\le k}}^{k} b_i x_i + \sum_{\substack{i=1, j=1, i\neq j \\ 1\le i<j\le k}} b_{ij} x_i x_j + \sum_{i=1}^{k} b_{ii} x^2 + \cdots \quad (1)$$

where: Y is the dependent parameter investigated and x_i, x_j the independent parameters that influence the dependent parameter taken in the analysis.

Independent variables (x_i…) taken in the analysis were those related to carbon enrichment phase: isothermal temperature, $T_K(x_1)$, the maintaining time, $t_K(x_2)$ at carburizing temperature and carbon potential, $C_{potK}(x_3)$.

In context of second order of noncompositional programming was imposed to vary the three independent variables at three levels of value, -1, 0 and +1. The noncompositional second order programming plan is itself a selected segment of the factorial experiment 3k (k is the number of factors or independent variables). As the dependent variables of the process (Y_1….Y_n), were selected those features that allow a more complete characterisation of the effects of surface enrichment in carbon due to maintenance of the AMS 6265 steel parts in the enriched gaseous saturated hydrocarbon (methane) atmosphere. The programming noncompositional matrix of the second order, for k=3, the basic level of the independent parameters, their range of variation and the results of the surface hardness measurements parts are presented in the Table 1.

Table 1. *Noncompositional programming matrix of the second order (k=3)*

-	F.V.	Independent parameters			$[HRC]_{SUP.}$
		1*	2*	3*	[HRC]
Code	X_0	X_1	X_2	X_3	Y
Basic level, (Z_{i0})	-	925	6	0,9	-
Range variation, (ΔZ_i)	-	25	3	0,2	-
Higher level, ($Z_{i0}+\Delta Z_i$)	-	950	9	1,1	-
Lower level, ($Z_{i0}-\Delta Z_i$)	-	900	3	0,7	-
EXP.nr.1	+1	+1	+1	0	62
EXP.nr.2	+1	+1	-1	0	62
EXP.nr.3	+1	-1	+1	0	63
EXP.nr.4	+1	-1	-1	0	62
EXP.nr.5	+1	+1	0	+1	63
EXP.nr.6	+1	+1	0	-1	60
EXP.nr.7	+1	-1	0	+1	63.5
EXP.nr.8	+1	-1	0	-1	60
EXP.nr.9	+1	0	+1	+1	63.5
EXP.nr.10	+1	0	+1	-1	61.5
EXP.nr.11	+1	0	-1	+1	63
EXP.nr.12	+1	0	-1	-1	62.5
EXP.nr.13	+1	0	0	0	63
EXP.nr.14	+1	0	0	0	63
EXP.nr.15	+1	0	0	0	62

Notes:
- F.V. – a fictive variable
- *1 - the carburizing temperature, T_K [ºC], Z_1;
- *2 – the maintaining time at carburizing temperature, t_K, [hours], Z_2;
- *3 – the carbon potential for carburizing process, C_{potK}, [%C], Z_3.

This paper has taken in analysis (as dependent variable) one of the most important mechanical characteristic variable of carbon hardened case, the surface hardness part, expressed in Rockwell (HRC) units, which together with other characteristics, that the effective case depth, ($\delta_{ef.}$), expressed in [mm], the subsurface carbon content, ($C_{0.1mm}$), the retained austenite, ($\%RA_{0.1mm}$), the subsurface microhardness, ($HV_{0.1mm}$), all of these measured to the 0.1mm distance from the workpiece surface and the case depth affected by internal oxidation, characterize the quality of the carburizing process.

To establish the algorithm for determining the particular forms of nonlinear models for the dependent variable which was taken in discussions it is necessary to be covered the following steps of the processing experimental results obtained:

- Calculation of non linear model coefficients (b_0, b_i, b_{ij}…);
- The statistical verification of nonlinear model coefficients;
- Calculation of the reproducibility results dispersion;
- Verification the concordance of nonlinear model adopted

2.2. The actual development of experimental batches and modalities for determining and evaluating experimental results

The experiments were conducted in a batch furnace type using endogas atmosphere enriched with methane gas. The chemical composition of the samples used (AMS 6265 steel) is presented in Table 2.

In order to study the influence of the independent parameters (temperature, maintaining time and carbon potential) on the mechanical characteristic (surface hardness part) as dependent parameter, fifteen carburizing batches were carried out, of which the last three batches have been performed under the same conditions of temperature, time and carbon potential. For each experimental batch were recorded temperature, carbon potential and real changes in their values.

Table 2. *Chemical composition of AMS 6265 steel*

Alloy (steel)	**Elements content, %**						
AMS 6265	**C**	**Si**	**Mn**	**Cr**	**Mo**	**Ni**	**Cu**
min.	0.07	0.15	0.4	1.00	0.08	3.0	max. 0.35
max.	0.13	0.35	0.7	1.40	0.15	3.5	
actual	0.11	0.33	0.57	1.14	0.13	3.26	0.09

In Table 1 are presented the parameters (thermal, temporal and chemical) adopted in the developing the fifteen experiments.

All actual cycles show the same general aspects of which the most significant features are the following two (see Figure 1):

1) The batches loading were performed in the preheated furnace to the carburizing temperature process. During the batches loading the furnace temperature down to about 50÷60ºC below to the initial setting point temperature. After 12÷16 minutes, batch temperature reached the prescribed value, specific to the each experimental cycle. For this reason the effective thermal cycles are easily moved to the right (recovery time) with a period of time which account the time for batch loading, batch reheating to the process temperature and time for achieving in the furnace the atmosphere carbon potential prescribed.

2) The real chemical cycles show a certain delay in the same initial period (recovery time) until achieving in the furnace the atmosphere carbon potential prescribed, whose duration varies according to the prescribed value of carbon potential.

Taking into consideration that chemical and thermal cycles are systematic, uniform and proportional with the carbon potential and carburizing temperature in all experimental batches, the displacements have not altered the types and degrees of influence of independent variables (process parameters) on the dependent variables (features), respectively on the experimental results obtained. The specimens (ø 18.5 mm x 30 mm) on which were made the HRC surface parts measurements were taken from the carbon hardened samples final heat treated which were used for the metallographic evaluations.

In Table 1 are presented the values obtained for the surface HRC parts measurements.

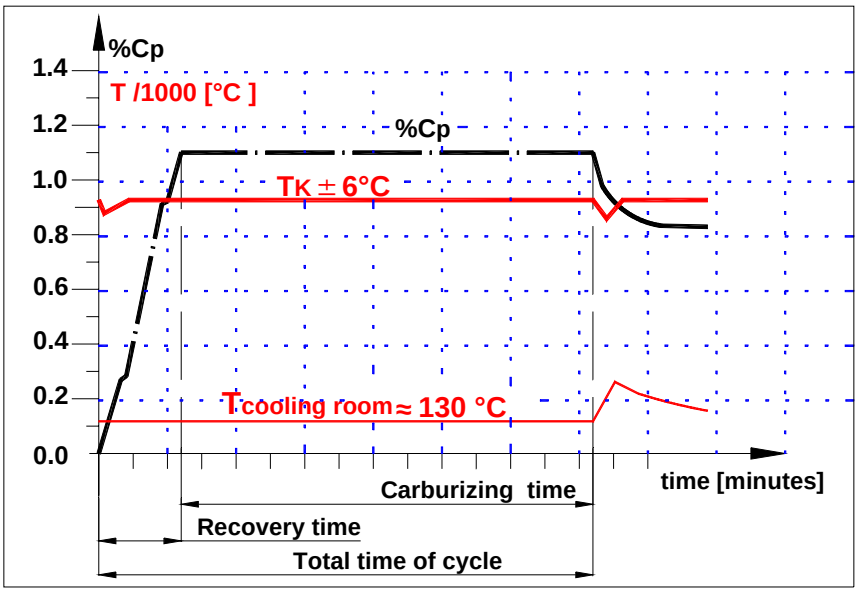

Fig.1. *Thermal and chemical cycles used in the experimental study, general characteristics.*

3. Experimental research results

The mathematical model was accomplished by determining the regression equations, able to allow the prediction performance which can be obtained by choosing the concrete conditions of the carburizing process on the AMS 6265 steel parts for the aeronautical industry.

After the stages calculating of the coefficients and statistical verifications specific to the programming method chosen, the following particular forms of the regression equations, specific to the steel taken in the analysis have resulted:

$$Y = 62.666 + 1.125X_3 - 0.708X_1X_2 \quad (2)$$

$$[HRC]_{SUP} = 5.1875 + 0.0566T_K + 8.73t_K + 5.62C_{potK} - 0.00942T_K \cdot t_K \quad (3)$$

The equations (2) and (3) represent the encoded respectively decoded forms of the mathematical model of the surface hardness parts, expressed in HRC units.

3.1. Numerical processing, analysis and interpretation of experimental research results

The comparative analysis of the two equations show that the terms with the greatest influence is the term of the first order degree (X_3, respectively C_{potK}) and the second degree term of the form X_1X_2 (T_Kt_K) has a significant influence in the both equations.

Based on this finding it can be concluded that the mathematical model deduced is predominantly linear, fact also confirmed by the aspects of response surfaces and by the positions of the certain isoproperties areas of the HRC surface hardness (see Figure 2 and Figure 3).

By analysis the encoded equation (2) shows that the coefficient for independent variable X_3 (first order degree term) is positive, which leads to the conclusion that the value of Y (HRC) increases with the increasing value of this independent process parameter.

The coefficient of the second - degree term in X_1X_2 ($-0.708X_1X_2$) is negative which leads to the conclusion that the value of Y (HRC) decreases with increasing values of X_1 and X_2 independent parameters.

Regarding the numerical value and sign of the influence coefficients which determine the degree and the direction of the influence of independent variables, these may be more strongly evident in the case of the decoded equation, in which the b_ix_i, $b_{ij}x_{ij}$, products, are terms whose by algebraically summing permit to obtain the dependent parameter value (see Table 3).

Table 3. *Detailed calculation of the surface HEC hardness in the concrete case (the base level of independent parameters): T_K = 925ºC, t_K = 6 hours, C_{potK} = 0.9%C*

Characteristic	b_0	b_1T_K	b_2t_K	$b_3C_{pot\,K}$	$b_{12}\,T_K\,t_K$	$Y_{calculated}$
$[HRC]_{SUP}$	5.1875	52.416	52.4025	5.0625	-52.2856	**62.7829**

In the regression decoded equation on observe that:

- the first - degree term in C_{potK} ($5.62C_{potK}$) is positive (5.0625) which leads to the conclusion that the value of Y(HRC) increases with the increasing of C_{potK} value in all range of variation of independent parameters X_1, X_2, X_3 (-1, 0, +1) respectively:
- process temperature, T_K: 900ºC, 925 ºC and 950ºC;
- maintain time process t_K: 3 hours, 6 hours and 9 hours;
- carbon potentials C_{potK}: 0.7 %C, 0.9 %C and 1.1 %C.

- the first - degree terms in T_K ($0.0566T_K$) and in t_K ($8.73t_K$) are positive (52.416 respectively 52.4025) which leads that these parameters have a positive influence on the variation of Y(HRC) value.

- the second-degree term in $T_K \cdot t_K$, ($-0.00942T_K \cdot t_K$), has a negative value (-52.2856) which leads to the conclusion that the combination of these parameters have a negative influence on the variation of Y(HRC) value.

In order to determine practical how the variation of the three technological parameters affects the surface hardness value of carburized parts made from the studied steel, the decoded equation (2) was introduced into a numerical simulation program for determining the numerical values ranges of temperature and maintaining time for which these parameters have the most significant influences. In

Table 4. *Influence of the maintaining time (t_K) on the surface hardness at T_K = 900ºC, 925 ºC and 950 ºC*

T_K = 900ºC (X_1 = -1)			
C_{potK} [%C]	Maintaining time [hours]		
	3	**6**	**9**
0.7	60.8175	61.5735	62.3295
0.9	61.9415	62.6975	63.4535
1.1	63.0655	63.8215	64.5775
T_K = 925ºC (X_1 = 0)			
C_{potK} [%C]	Maintaining time [hours]		
	3	**6**	**9**
0.7	61.526	61.5755	61.625
0.9	62.65	62.6995	62.749
1.1	63.774	63.8235	63.873
T_K = 950ºC(X_1 = +1)			
C_{potK} [%C]	Maintaining time [hours]		
	3	**6**	**9**
0.7	62.2345	61.5775	60.9205
0.9	63.3585	62.7015	62.0445
1.1	64.4825	63.8255	63.1685

Table 4 are presented the hardness values results, after numerical processing, concerning the influence of the maintaining time on the variation value of the hardness surface, by modification the temperature value at the three levels adopted in the experimental program.

In Table 5 are presented the hardness values results, after numerical processing, concerning the influence of the temperature on the variation values of the hardness surface, by modification the maintaining time value at the three levels adopted in the experimental program.

By analysis the results presented in Table 4 on observe that, at the same carbon potential and at constant temperature value T_K = ct.= 900ºC (the inferior level) the surface hardness value increases with the increasing of the maintaining time in all the range of variation of the time values (3h ≤ t_K ≤ 9h). At T_K = 925ºC (the base level) on observe that the increasing value of the maintaining time, in the same range of values of the time, (3h ≤ tK ≤ 9h), affects in very slight the surface hardness value (it remain practically constant). When the temperature value is T_K = ct. = 950ºC (the superior level), the increasing value of the maintaining time affects negative, respectively decreases the surface hardness value.

Table 5. *Influence of the temperature (T_K) on the surface hardness at t_K = 3 hours, 6 hours and 9 hours*

t_K = 3 hours (X_2 = -1)			
C_{potK} [%C]	Maintaining time [hours]		
	900	925	950
0.7	60.8175	61.526	62.2345
0.9	61.9415	62.65	63.3585
1.1	63.0655	63.774	64.4825
t_K = 6 hours (X_2 = 0)			
C_{potK} [%C]	Maintaining time [hours]		
	900	925	950
0.7	61.5735	61.5755	61.5775
0.9	62.6975	62.6995	62.7015
1.1	63.8215	63.8235	63.8255
t_K = 9 hours (X_2 = +1)			
C_{potK} [%C]	Maintaining time [hours]		
	900	925	950
0.7	62.3295	61.625	60.9205
0.9	63.4535	62.749	62.0445
1.1	64.5775	63.873	63.1685

In Table 5 on observe that at the same carbon potential value and at constant time value, t_K = ct. = 3h (the inferior level), the superficial hardness increases with increasing the value of temperature in all range of variation of temperature values, (900ºC ≤ T_K ≤ 950ºC). At t_K = ct. = 6 h (the base level) on observe that the increasing temperature, in same range of the temperature values affects in slight the superficial hardness value (it remain practically

constant), as with previously analyzed for T_K = 925ºC. When the maintaining time is t_K = ct. = 9 h (the superior level) the increasing value temperature process affects negative, respectively decreases the superficial hardness value.

The analysis presented above emerges that the statistical ensemble of carburizing process the carbon potential has a positive influence on the value of the surface hardness, without overcoming the certain values levels, but the combination between time and temperature can have a negative influence on this characteristic (they can cause the reduction in value of this feature).

3.2. Graphical processing of experimental results

The graphical processing of the experimental research results (Figure 2 and Figure 3) creates a more suggestively picture of the manner in which the three main independent variables (process parameters) of the carburizing process: the temperature at which the process is carried out, T_K, the maintaining time t_K, at this temperature, and the carbon potential, C_{potK}, of the furnace atmosphere influence the value of the surface hardness value.

T_K = ct. = 900 ºC

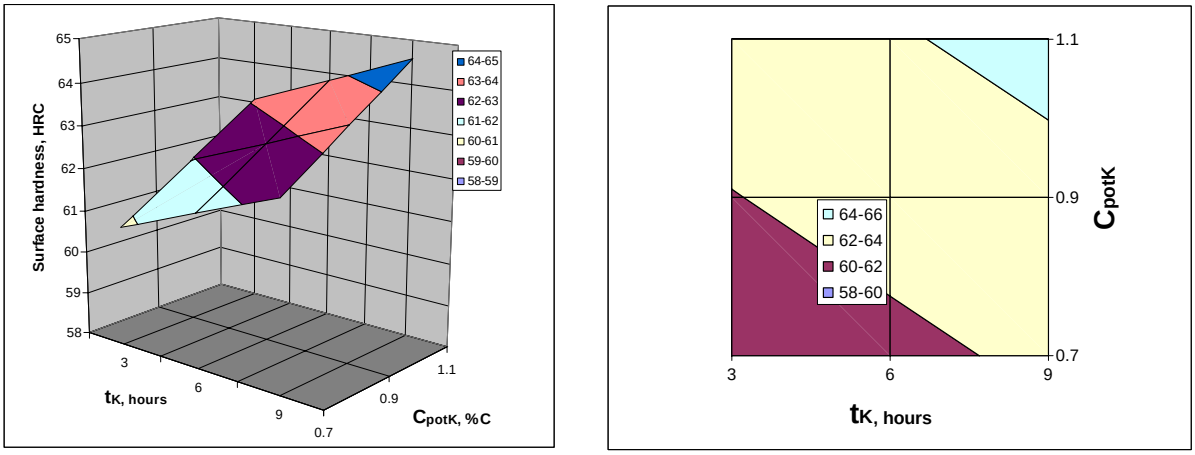

T_K = ct. = 925 ºC

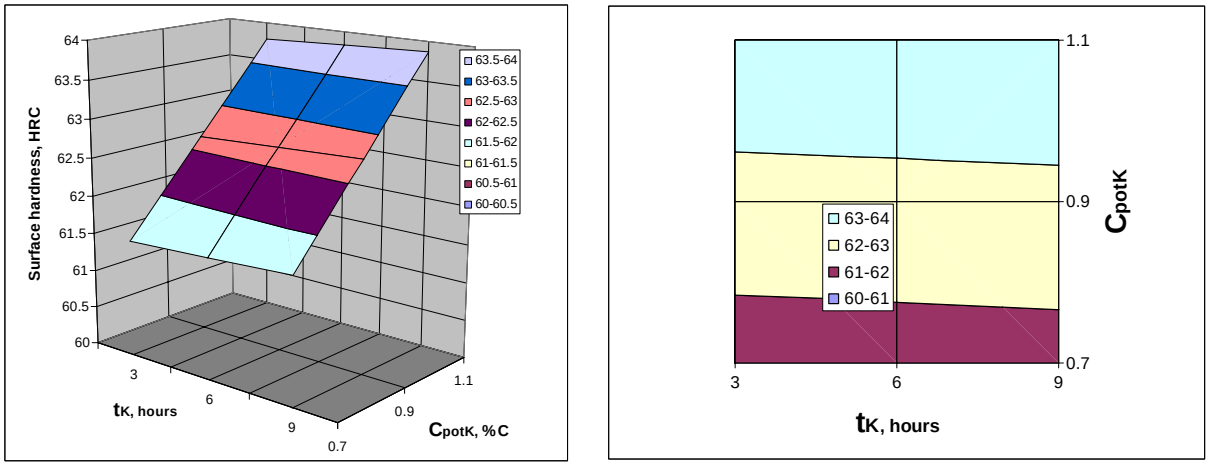

T_K = ct. = 950 ºC

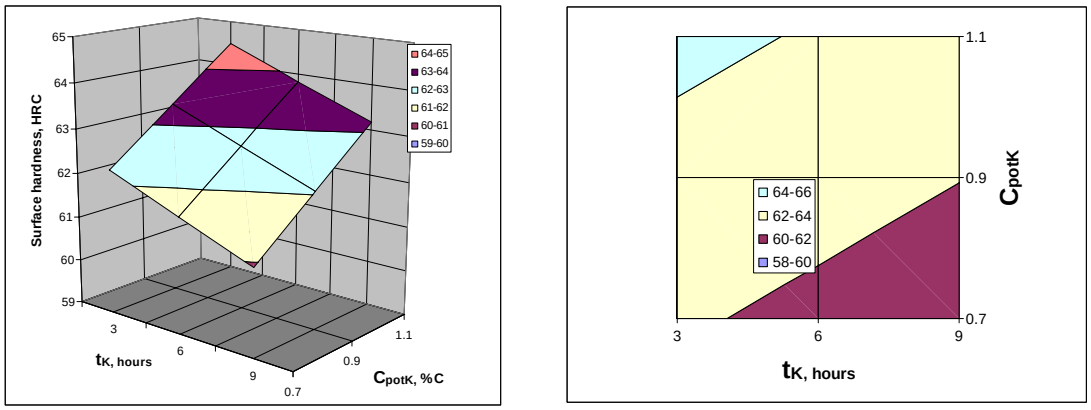

AMS 6265 (SAE 9310)

Fig.2. *The surfaces response of the mathematical model that describes the variation of surface hardness at T_K = 900 ºC, T_K = 925 ºC, T_K = 950 ºC (left) and the delimitation areas of isoproperties (right), depending on the temporal and chemical parameters of the carburizing process AMS 6265 (SAE 9310) steel parts.*

t_K = ct. = 3 hours

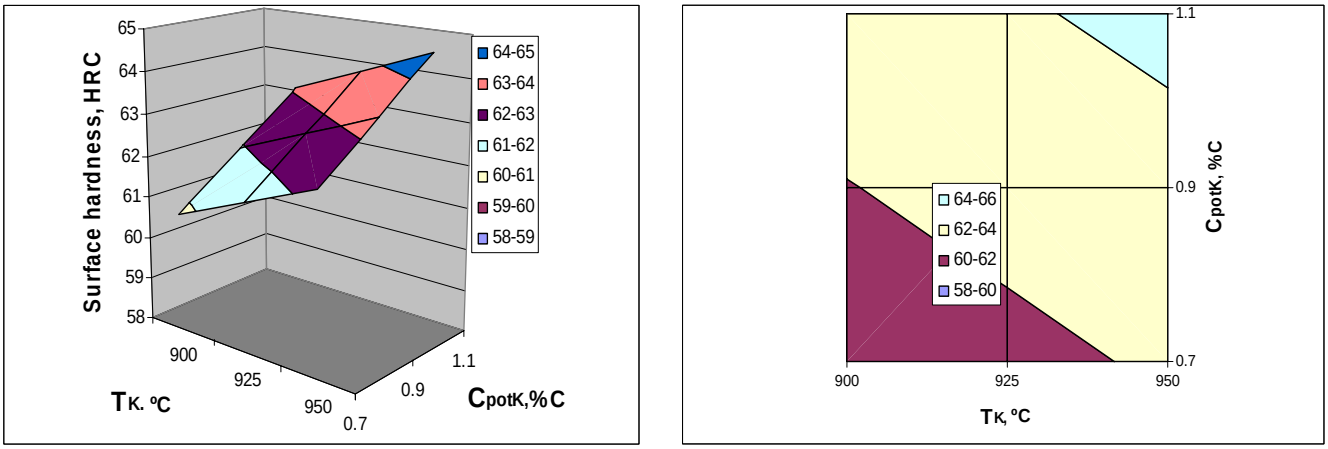

t_K = ct. = 6 hours

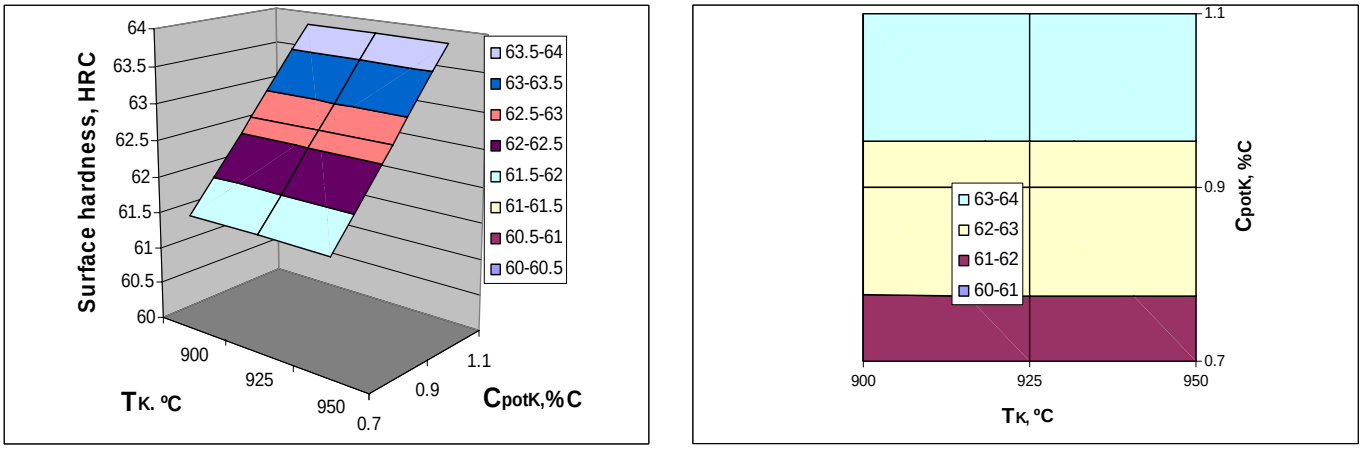

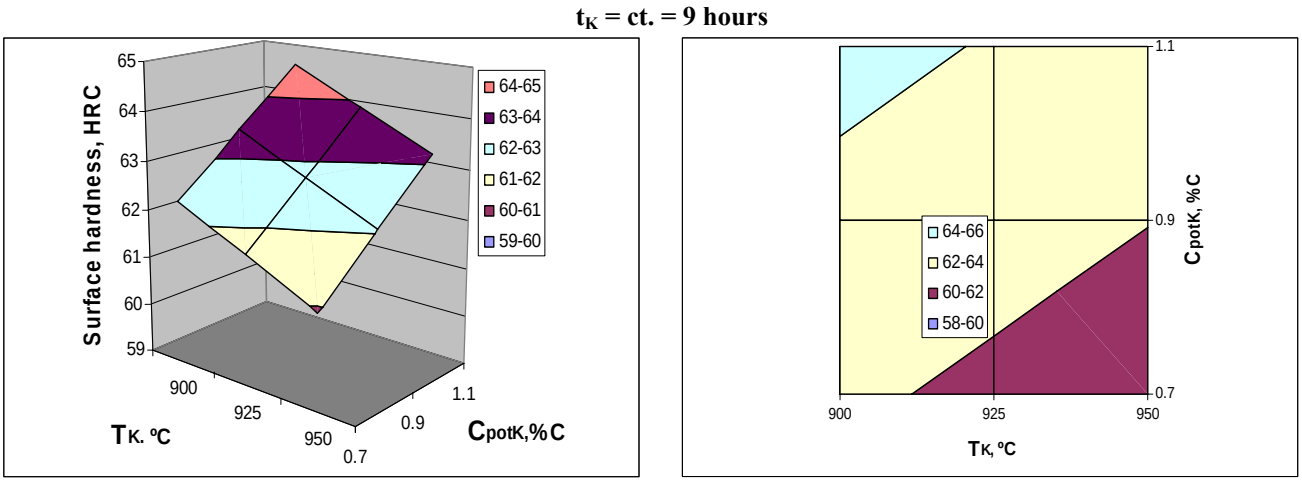

Fig.2. *The surfaces response of the mathematical model that describes the variation of surface hardness at t_K =3 hours, t_K = 6 hours, t_K = 9 hours (left) and the delimitation areas of isoproperties (right), depending on the thermal and chemical parameters of the carburizing process AMS 6265 (SAE 9310) steel parts.*

7. Conclusions

From the analysis of the results obtained after performing experimental study concerning the influence of the three main technological parameters, the thermal, the temporal and the chemical of the carburizing process (which is based on mass transport phenomena by diffusion) on the HRC surface hardness value of the AMS 6265 (SAE 9310) steel parts it can draws the following conclusions:

1. The HRC surface hardness value is positive influenced by the carbon potential of furnace atmosphere and negative by the time and the temperature values, when the values exceed certain levels, according to the mathematical model, calculated and expressed by the both equations (2 and 3). The reason of the positive carbon potential influence on the surface hardness parts consist in the fact that an elevate carbon content in austenite determine, after hardening, a high carbon content in the martensite with a high hardness.

The negative influence of increasing the temperature and the maintaining time of carburizing process above certain limits can be explained by the fact that by increasing the values of these two technological parameters can determine the excessive grows of the austenitic grain size and increases the internal oxidation phenomenon so that, after hardening, on obtain a large proportion of retained austenite and in the surface of parts the martensite is replaced by the high temperature product (troostite) characterized by low values of the hardness.

2. For increasing the parts hardness surface is indicate during the carburizing process, to operate with low temperatures and maintaining times (minimum possible) and with high value of carbon potential, but not more than the solubility limit of carbon in austenite (approximately 1.1% C_{potK}) taking in consideration that the AMS 6265 steel is alloyed in a high enough proportion with chromium;

3. The mathematical model calculated in this work was verified in industrial practice with good results witch allow to use it for to estimate the HRC hardness surface parts and for optimizing thermochemical carburizing treatment of AMS 6265 parts steel, in a large enough range of the key process parameters values:

- temperature: 900 ºC $\leq T_K \leq$ 950 ºC;
- maintain time: 3 hours $\leq t_K \leq$ 9 hours;
- carbon potentials: 0.7 %C $\leq C_{potK} \leq$ 1.1 %C.

References

[1]. D.Taloi, E. Florian, E. Berceanu - *Optimizarea proceselor metalurgice*, Editura Didactică şi Pedagogică, Bucuresti, 1983.
[2] G. Parrish - *Carburizing, Microstructuructures and Properties,* AMS International, 1999.
[3] The Timken Company - *"Timken-Practical Data for Mettalurgist"*, The Timken Company, 14th edition, 1999.
[4] N. Popescu, M. Cojocaru - *Cementarea oţelurilor prin instilarea lichidelor organice*, Editura Fair Matrix Rom, Bucureşti, 2005.
[5] M. Cojocaru - *Procese de transfer de masă*, Editura Matrix Rom, Bucureşti, 2004.
[6] M. Cojocaru, M. Târcolea - *Modelarea interacţiunilor fizico-chimice ale produselor metalice cu mediile*, Editura Matrix Rom, Bucureşti, 1998.

THE ANNALS OF "DUNAREA DE JOS" UNIVERSITY OF GALATI.
FASCICLE IX. METALLURGY AND MATERIALS SCIENCE
N^0. 4 – 2011, ISSN 1453 – 083X

COOLING RATE DEPENDENCE OF STRUCTURES CHARACTERISTICS IN Ce-INOCULATED LOW-S GREY IRONS

Irina Varvara ANTON, Iulian RIPOSAN*
Politehnica University of Bucharest
*Corresponding author
email: riposan@foundry.pub.ro

ABSTRACT

The efficiency of Ce,Ca,Al-FeSi alloy was tested for lower addition rates (0.15-0.25wt.%), as, traditionally, high inoculant addition rates have been used in low sulphur grey cast irons, comparing to the base iron and conventional inoculated irons (Ba,Ca,Al-FeSi commercial alloy). The present work explores chill and associated structures in hypoeutectic grey iron chill wedges, with cooling modulus 0.21 cm and a large variation of the cooling rate, from the apex to the base of W_2 samples [ASTM A 367, furan resin mould]. The chill tendencies of the experimental irons correlate well with the structure characteristics, displayed as the carbides/graphite ratio of undercooled graphite morphologies. Carbide sensitivity is lower with increasing wedge width, but depends on whether the state of the iron is as base iron or inoculated with different alloys. Undercooled graphite was present for both un-inoculated irons and higher cooling rate inoculated irons. As expected, inoculation as well as an increase in wall thickness of the same wedge sample led to improved undercooled graphite control. The difference in effects of the two inoculants addition is seen as the ability to decrease the amount of carbides and undercooled graphite, with Ce-bearing FeSi alloy outperforming the conventional inoculant, especially at the low alloy addition and high cooling rate solidification.

KEYWORDS: Grey iron, Low S, Cooling rate, Inoculation, Ce, Structure, Carbides, Graphite morphology

1. Introduction

Inoculation is a means of controlling the structure and properties of cast iron by minimizing eutectic undercooling and increasing the number of active graphite nucleation sites during solidification. The role of an inoculant, usually as a FeSi-based alloy including one or more inoculating elements (Ca, Ba, Sr, Ce, La etc), is to influence the formation, characteristics and, thereby, the quality of nuclei for flake graphite and the eutectic structure, respectively.

It accomplishes this by improving the micro-inclusions that already exist in the iron melt (such as sulphides), rather than by creating new compounds. However, this is possible especially as nitrides, in iron melts with very low sulphur content.

Generally, well inoculated grey irons are characterized by graphite nucleation with a low degree of eutectic undercooling, usually as more than 25^{o}C above the metastable (carbidic) eutectic equilibrium temperature (Tmst), which is the base condition to promote Type A graphite (random graphite flakes form uniformly in the iron matrix).

As the undercooling increases and graphite nucleation start is closer to Tmst, the graphite will branch, forming abnormal patterns. This is known as Types B, D and E graphite ***(Fig. 1).***

A further increase in undercooling will suppress the formation of graphite and results in a hard and brittle white iron carbide structure, at very low machinability.

The avoidance of both carbides and undercooled graphite morphologies (B, D, E) in the advantage of Type A graphite formation is the most important objective of the inoculation in grey cast iron production.

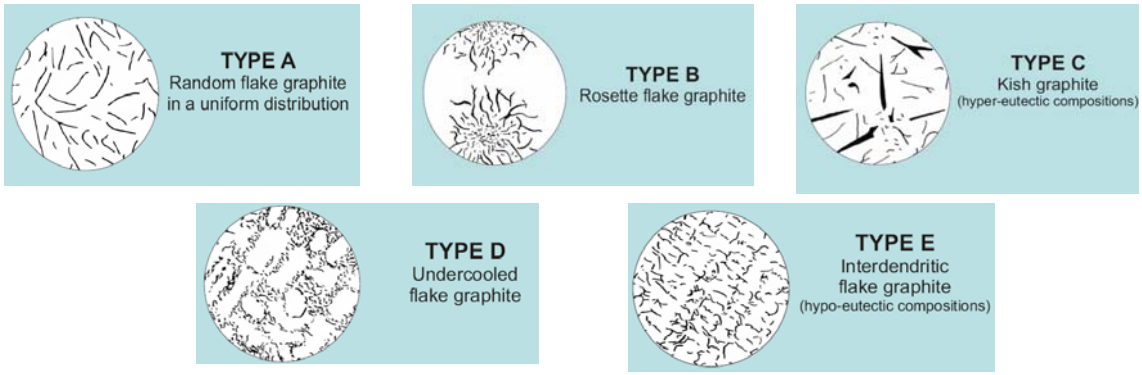

Fig. 1. *Typical graphite morphologies in grey cast iron (ASTM).*

There are a lot of causes for higher eutectic undercooling and undercooled graphite formation in grey irons, such as lower carbon equivalent level (low carbon and / or silicon), detrimental contents of Mn, S and Al [< 0.05%S, < 0.03 as (%Mn) x (%S) control factor, < 0.004%Al] to sustain complex (Mn,X)S compounds formation as major graphite nucleation sites [1-6], melting practice (high steel scrap amount, high superheating and holding time etc) and pouring practice (low pouring temperature, moulds with high thermal conductivity, thin wall castings etc) [7-9].

The actual world practice in grey iron foundries, involving melting shops including the new generation, acid lined, medium frequency coreless induction furnaces (200-1000Hz, > 250 kW/t specific power) and thin wall castings production led to critical conditions for iron solidification, as base iron chemistry [< 0.05%S, < 0.005%Al, < 0.03 (%Mn) x (%S)], more than 1500^{o}C superheating and more than 2^{o}C/sec cooling rate during solidification.

These irons are notoriously difficult to inoculate, in order to avoid carbides and/or undercooled graphite morphologies, especially in economic conditions.

Previous experiments [7,10-12] illustrated the efficiency of some special inoculating variants in low sulphur grey irons, such as Rare Earth (RE) bearing FeSi alloys (Ce, La or Mischmetal variants) or complex inoculants, such as the most representative Ca,Ba,Al-FeSi, Zr,Sr-FeSi, and Ca,Ce,Al-FeSi alloys.

The main objective of the present paper is to examine the effect of Ce,Ca,Al-FeSi alloy on the structure characteristics of low sulphur grey cast irons, comparing to a conventional (commercial) inoculant in Ba,Ca,Al-FeSi alloy system, at lower addition rates procedures (< 0.3wt% inoculant) and a large variation of the cooling rate during solidification, as castings geometry.

2. Experimental procedure

The experimental melts were obtained using an induction furnace (acid lining, 100kg, 2400Hz).

The iron melt was heated to 1540^{o}C held for 10 min, then tapped into the pouring ladle (10kg) at 1530^{o}C allowing a final pouring temperature at 1350^{o}C into furan resin sand moulds.

A proprietary Ce-bearing FeSi alloy [1.5-2.0%Ce, 0.75-1.25%Ca, 0.75-1.25%Al, 70-76%Si, Fe bal] [10] was used, comparing to a conventional (commercial) Ba,Ca,Al-FeSi inoculant (typically chemistry: 1.5%Ca, 1.0%Ba, 1.0%Al, 65%Si, Fe bal), both of them at 0.2-0.7mm grain size range.

Addition rates were as 0.15wt.% and 0.25wt.%, point of addition was into the stream when tapping from the furnace into the pouring ladle.

The following final chemical compositions of the inoculated irons were obtained: 3.15-3.3%C, 1.50-1.55%Si, 0.67-0.70%Mn, 0.020-0.025%S, 0.001-0.002%Al, 0.015–0.018%Ti, 0.0060-0.0100%N, 0.05-0.1%Cr, 0.025-0.050%Ni, 0.009-0.015%Mo, 0.004 – 0.006% V, at carbon equivalent 3.6-3.8% CE.

Chill wedges of the type W_2 (10.2mm base width, 31.8mm height, cooling modulus CM=0.21cm) specified in the ASTM A-367 wedge test were considered (resin sand mould), as usually used chill samples in grey iron foundries.

CM is defined as the ratio between volume and the total external casting surface and is an expression of the capacity to transfer a given quantity of heat through an existing surface to the mould.

Higher CM equates to slower cooling rate (CR) and lower undercooling during eutectic solidification. The equivalent cooling modulus, represented by W_2 wedges, corresponds to round bars with diameter of 8.4 mm.

3. Results and discussion

In a chill wedge, that portion nearest the apex, entirely free of grey areas, is designated as the clear chill zone (W_c).

The portion from the end of the clear chill zone to the location where the last presence of cementite, or white iron is visible, is designated the mottled zone (W_m).

The region from the junction of grey fracture to the first appearance of chilled iron (apex) is designated the total chill (W_t).

The parameters relative clear chill (RCC) and relative total chill (RTC) were also considered:

$$RCC = 100\ [W_c / B]\ (\%) \quad (1)$$

$$RTC = 100\ [W_t / B]\ (\%) \quad (2)$$

Where B is the maximum width of the test wedge.

A medium solidification rate, represented by a W_2 wedge sample, was also used to evaluate the structure formation in un-inoculated and different inoculated irons, with the two considered inoculants (Ce,Ca,Al-FeSi and Ba,Ca,Al-FeSi alloys) at the two addition rates (0.15wt.% and 0.25wt.%) ***(Table 1).***

Table 1. *Structure characteristics [W_2 – wedge sample, ASTM A367]*

Wedge width (mm)	Inoc. (%)	Carbides, %			Graphite; %			Undercooled Graphite (B+D+E), %			Ferrite, %		
		U.I	Ba,Ca-FeSi	Ce,Ca-FeSi	U.I	Ba,Ca-FeSi	Ce,Ca-FeSi	U.I	Ba,Ca - FeSi	Ce,Ca - FeSi	U.I	Ba,Ca - FeSi	Ce,Ca - FeSi
1.91	0.15	40	30.0	30.0	1.5	1.5	2.25	100	100	100	0	0	0
	0.25		35.0	30.0		1.75	3.25		100	100		0	0
3.25	0.15	40	29.0	20.0	1.5	2.5	3.5	100	100	100	0	0	4.0
	0.25		22.5	7.5		3.5	4.5		100	100		2.5	4.0
4.89	0.15	39.5	6.5	3.0	1.5	3.25	6.0	100	100	90	0	4.0	5.0
	0.25		4.0	1.5		5.0	6.5		100	80		4.0	2.5
6.62	0.15	35	2.5	2.0	1.75	6.5	8.5	100	90	70	0	5.0	5.0
	0.25		0	0		7.5	9.5		65	40		5.57	2.0
8.18	0.15	39.5	6.5	2.0	1.75	8.5	11.0	100	85	70	0	5.0	5.0
	0.25		0	0		10.0	11.5		50	30		6.5	1.0

Fractures of W_2-samples ***(Fig.2)*** were analyzed metallographically, un-etched and etched with Nital (2%), along the geometrical centerline of the chill wedge and at different distances from the apex of the wedge.

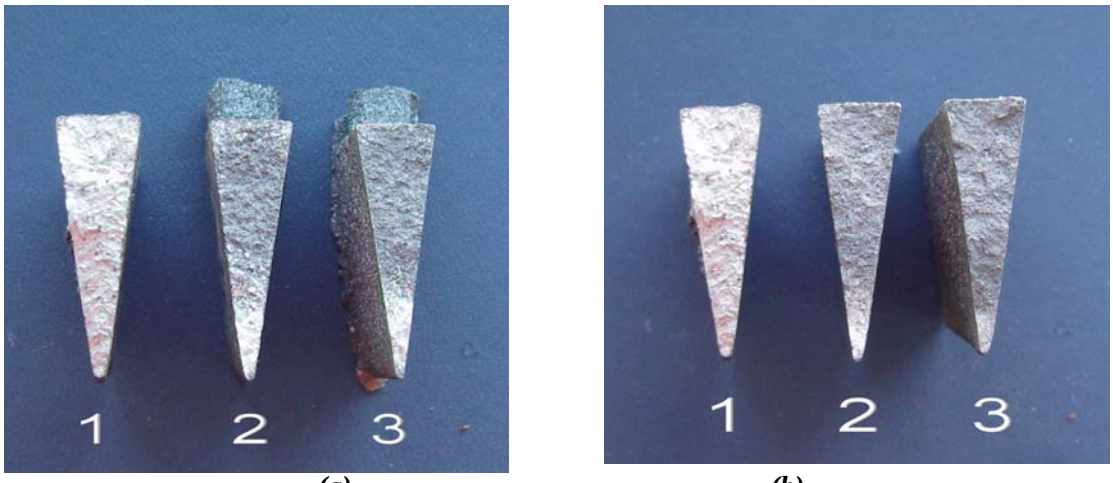

(a) ***(b)***

Fig. 2. *Influence of Ba,Ca,Al-FeSi (a) and Ce,Ca,Al-FeSi (b) inoculation (1 - un-inoculated, 2 - 0.15% alloy and 3 - 0.25% alloy) on the chill wedge W_2-ASTM A367 macrostructure.*

Using chill samples, offering different wall thickness simulated different solidification conditions to be explored. At the farthest distances from the apex of the chill wedge, the cooling rates are very shallow.

The chill tendencies of the experimental irons correlate well with the structure characteristics, displayed as the carbides / graphite ratio and as the presence of undercooled graphite morphologies. Different structures were obtained at the same area (width) of the wedge sample.

Figures 3a and 3b illustrate that an inverse relationship exists between free carbides level and distance from the apex of the chill wedge, and the wedge width, respectively.

Carbide sensitivity is lower with increasing wedge width, but depends on whether the state of the iron is as base iron or inoculated with different alloys and with different additions, too.

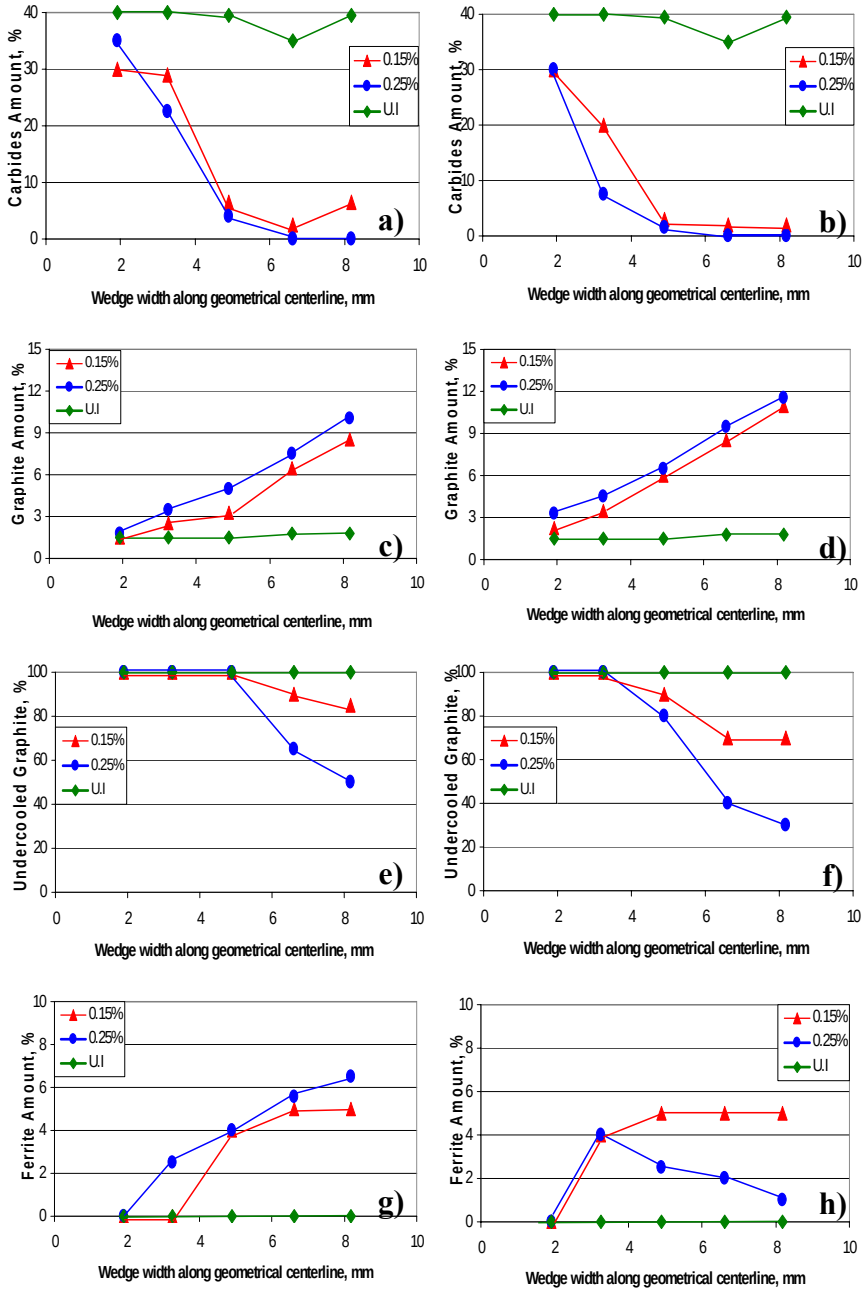

Fig. 3. *Influence of inoculant type (a,c,e,g-Ba,Ca,Al-FeSi; b,d,f,h-Ce,Ca,Al-FeSi) and amount (0.15 and 0.25wt.%) on the structure characteristics along the geometrical centerline of W_2 -ASTM A367 chill wedge comparing to un-inoculated (UI) irons [a, b-carbides amount; c, d-graphite amount; e, f-undercooled graphite amount; g, h-ferrite amount].*

The inoculation was able to totally avoid free carbides formation for more than 6.5mm wall thickness for Ba,Ca-FeSi inoculated irons and 5mm for Ce,Ca-FeSi treatment, with a limited difference for the two inoculant addition rates. Ce-bearing inoculant appears to be more effective especially for thin wall castings (3-4mm), despite the critical conditions of chemical composition.

It was found that despite the white iron appearance, the samples contained different amounts of free carbides and a small amount of graphite, depending on the inoculant type and addition rate ***(Figs. 3c, d).***

According to the higher capacity to prevent free carbides formation, Ce-bearing FeSi alloy led to higher graphite amount for the same cooling rate solidification conditions and for the two addition rate procedures.

Un-inoculated iron is more sensitive not only to free carbides formation (chill tendency) but also to undercooled graphite appearance at the lower solidification rate (at the base of the wedge sample).

Figures 3e and 3f show an inverse relationship between undercooled graphite levels and the distance from the apex of the chill.

Undercooled graphite was present for both un-inoculated irons and higher cooling rate inoculated irons.

As expected, inoculation as well as an increase in wall thickness of the same wedge sample led to improved undercooled graphite control.

The amount of undercooled graphite decreased with increasing the distance from the apex of the wedge. The Ce,Ca-bearing inoculant outperformed the Ba-Ca-FeSi alloy, especially at low inoculant additions. The difference in effects of the inoculant addition rates is seen as the ability to decrease the amount of undercooled graphite, especially above a 5.0 mm wedge width.

The amount of ferrite ***(Figs. 3g, h)*** is strongly dependent on the presence of undercooled graphite: the highest level of ferrite is typical in the mottled iron area, at the highest undercooled graphite amount.

The association of ferrite and carbides in the same area is an anomaly in the structure (pearlite and carbides normally coexist) and is typically linked to the presence of type D undercooled graphite morphologies. Medium eutectic undercooling led to free carbides and type D graphite formation during eutectic solidification (carbides at the beginning and graphite at the end of the eutectic reaction). The presence of type D graphite favors carbon diffusion during the eutectoid reaction due to the shorter distance between graphite particles and consequently ferrite formation (Ferrite + Pearlite = 100%), despite a high cooling rate during the eutectoid reaction (also typical for the center of type B graphite).

There is a difference depending on how chill is evaluated for inoculated irons macro-structure (fracture analysis, visual white/mottled iron evaluation) versus microstructure (metallographic analysis, free carbides/graphite presence) ***(Fig. 4).***

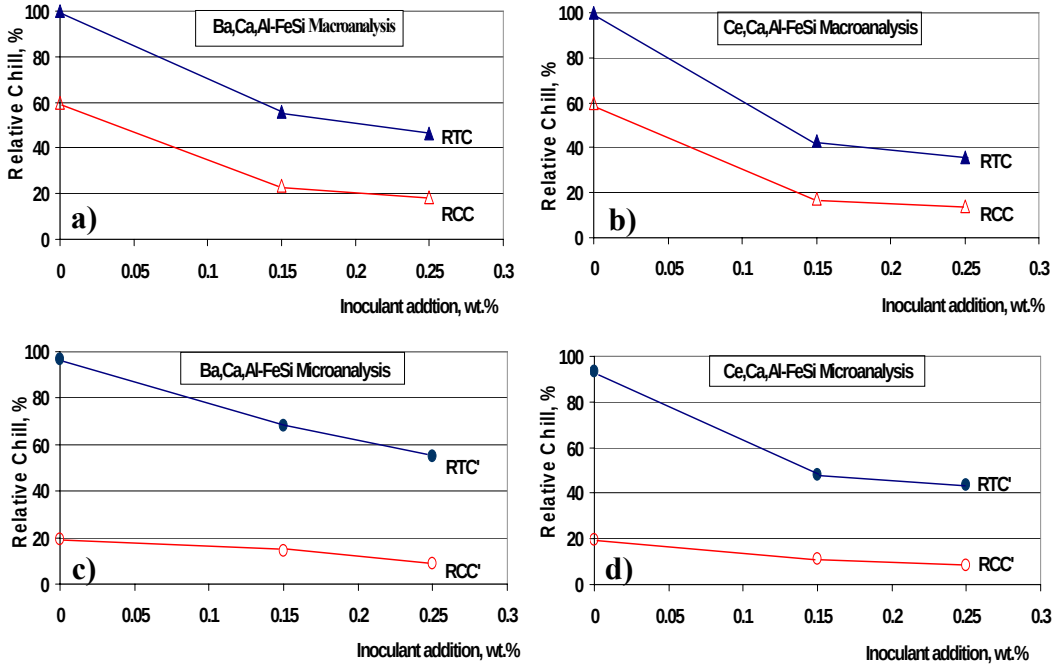

Fig. 4. *Relative clear (RCC) and total (RTC) chill evaluated by macro-analysis (a, b) and micro-analysis (c, d) of un-inoculated and Ba, Ca, Al-FeSi (a, c) and Ce, Ca, Al-FeSi (b, d) inoculated irons [W_2-ASTM A367 chill wedge].*

This difference is higher in inoculated irons, mainly at lower alloy addition rate, for relative clear chill (RCC) evaluation and bearing inoculant, respectively.

Ba, Ca-FeSi alloy inoculated irons.

Specific to the solidification pattern of wedge shaped samples is the end (corner) effect, which is an excessive sensitivity of iron to free carbides and / or undercooled graphite, at the greatest width, corresponding to the B - size parameter.

This phenomenon is more apparent for a lower inoculation potential, such as for 0.15wt.% Ba,Ca-FeSi inoculated cast irons. Ce-bearing FeSi alloy led to the avoidance of this phenomenon, as carbides formation, inclusively at lower addition rate procedure.

High cooling rates, typical for a corner effect [13], led to free carbides and / or undercooled graphite morphologies in all of these cases.

This peculiar solidification pattern of wedge shaped samples could create problems in accurately evaluating chill, especially for thin wall castings and for both relative clear chill and relative total chill criteria.

4. Summary

- The efficiency of a Ce-bearing FeSi inoculant on the structure characteristics (carbide, graphite, metal matrix) of low sulphur [< 0.025%S, (%Mn) x (%S) < 0.02], low aluminium [< 0.002%Al], hypoeutectic [3.6-3.8%CE] electric melt [>1500^{o}C] irons, was tested by comparing if to a conventional inoculant [Ba,Ca,Al-FeSi alloy], at lower addition rates [< 0.3wt.%] and a large variation of the cooling rate during solidification, as casting geometry [1-10mm].
- As expected, an inverse relationship exists between free carbides (in the benefit of graphite) and the undercooled graphite level (in the benefit of type - A graphite) and the distance from the apex of the chill wedge or wedge width, but depending on the inoculant type and addition rate, too.
- The inoculation was able to totally avoid free carbides formation for more than 6.5 mm wall thickness for Ba,Ca-FeSi inoculated irons and 5 mm for Ce,Ca-FeSi treatment.
- Ce-bearing inoculant appears to be more effective especially for thin wall castings (3-4 mm), despite the critical conditions of chemical composition of the base iron.
- According to the higher capacity to prevent free carbides formation, Ce-bearing FeSi alloy led to a higher graphite amount for the same cooling rate solidification conditions and for both of the addition rate procedures. The Ce-Ca-Al-FeSi inoculant outperformed the Ba-Ca-Al-FeSi alloy, especially at low inoculant additions.
- There appears to be a difference in chill (carbides formation) evaluation, for inoculated irons, between macrostructure (fracture analysis) and micro-structure (metallographic analysis).
- The chill tendency at a microstructure evaluation route appears to be important in thin wall castings after inoculation, for both relative clear chill and relative total chill criteria.
- The end (corner) effect, seen as a higher cooling rate at the highest width, leads to free carbides and / or undercooled graphite morphologies / ferrite, more especially for lower inoculation potential, such as Ba,Ca,Al-FeSi alloy and 0.15wt.% addition rate, respectively.

References

[1]. I. Riposan, M. Chisamera, S. Stan, T. Skaland, M.I. Onsoien - *Analyses of Possible Nucleation Sites in Ca/Sr Overinoculated Grey Irons.* AFS Trans., 2001, Vol. 109, pp. 1151-1162.

[2]. I. Riposan, M. Chisamera, S. Stan, T. Skaland -*Graphite Nucleants (Microinclusions) Characterization in Ca/Sr Inoculated Grey Irons.* Int. J. Cast Met. Res., 2003, Vol. 16, No. 1-3, pp. 105-111.

[3]. I. Riposan, M. Chisamera, S. Stan, C. Hartung, D. White. *Three-Stage Model for the Nucleation of Graphite in Grey Cast Iron.* Mater. Sci. Techn., 2010, Vol. 26, No. 12, pp. 1439-1447.

[4]. I. Riposan, M. Chisamera, S. Stan, C. Ecob, D. Wilkinson - *Role of Al, Ti, Zr in Grey Iron Preconditioning/Inoculation.* J. Mater. Eng. Perform., 2009, Vol. 18 (1), pp. 83-87.

[5]. R. Gundlach - *Observations on Structure Control to Improve the Properties of Cast Irons*. The 2008 Honorary Cast Iron Lecture, Div. 5, AFS Metalcasting Congress, Atlanta, Georgia, USA, Paper 08-158.

[6]. C. Hartung, C. Ecob, D. Wilkinson - *Improvement of Graphite Morphology in Cast Iron*. Casting Plant and Technology International, 2008, No. 2, pp. 18-21.

[7]. Cast iron inoculation, The Technology of Graphite Shape Control Brochure, Information on www.foundry.elkem.com, May 2009.

[8]. I. Riposan, M. Chisamera, S. Stan, G. Grasmo, C. Hartung, D. White - *Iron Quality Control During Melting in Coreless Induction Furnace.* AFS Trans., 2009, Vol. 117, pp. 423-434.

[9]. M. Chisamera, I. Riposan, S. Stan, C. Ecob, G. Grasmo, D. Wilkinson - *Preconditioning of Electrically Melted Gray Cast Irons.* AFS International Cast Iron Melting Conference, February 21-23, 2009, Orlando, Florida, USA.

[10]. Reseed® Inoculant–ELKEM Foundry Products Division Brochure. Information on http:// www.foundry.elkem.com (2004).

[11]. I. Riposan, M. Chisamera, S. Stan, E. Stefan, C. Hartung - *Role of Lanthanum in Graphite Nucleation in Grey Cast Iron.* Key Engineering Materials-KEM, Vol.457 [Science and Processing of Cast Iron IX], (2011), pp. 19-24. Trans. Techn. Publications, Switzerland.

[12]. I.V. Anton, I. Riposan - *Structure Characteristics of Ce-Inoculated, Low Sulphur Grey Cast Irons*. Advanced Materials and Structures - AMS '11 International Conference, Timisoara, Romania, Oct. 2011, Paper-045.

[13]. S. Stan, M. Chisamera, I. Riposan, E. Stefan, M. Barstow - *Solidification Pattern of Un- inoculated and Inoculated Gray Cast Irons in Wedge Test Samples.* AFS Trans., 2010, Vol. 118, pp. 295-309.

THE ANNALS OF "DUNAREA DE JOS" UNIVERSITY OF GALATI.
FASCICLE IX. METALLURGY AND MATERIALS SCIENCE
N^0. 4 – 2011, ISSN 1453 – 083X

PHOSPHATE PASSIVATION SOLUTIONS ENHANCED BY CHEMICAL ADDITIVES FOR TREATMENT OF THE HOT DIP GALVANIZED STEEL

Anișoara CIOCAN, Tamara RADU
Faculty of Metallurgy, Materials Science and Environment
"Dunărea de Jos" University of Galati
aciocan@ugal.ro

ABSTRACT

To stabilize the surface of the galvanized steel it is important to apply a passivation treatment during its manufacturing. The general aim of the passivation treatment is to prevent the formation "storage stain" or "white rust". For many decades, the chromium conversion treatments involving the use of chromic acid containing Cr6+ species have been used for their corrosion protection and adhesion promotion performances. Today all hexavalent chromates have been banned by the EC. Toxicological studies have evidenced the hazardous character of hexavalent chromium. Therefore more economical and environmentally friendly passivation solutions have been studied and used to replace the chrome passivations on galvanized steel.

Phosphate conversion coatings are commonly used on the galvanized steel. They form a thin protective film on steels surface. However, the formation of a stable and uniform coating for corrosion protection remains a challenge. More complexes passivating solutions with chemical activators added are the potential alternatives.

In this paper are presented the studies about such molybdate–phosphate passivation solutions as environmentally friendly alternative for chromium passivates. The results of treatments realized for different treatment times and more compositions were analyzed. Also the corrosion resistance of the passivated samples has been studied.

KEYWORDS: hot dip galvanized steel, molybdate–phosphate passivation film, corrosion resistance

1. Introduction

The protection of steel sheets is often obtained using a zinc coating by hot dip galvanizing technology. For inhibition of the formation "storage stain" or "white rust" on the surface of galvanizing steels must applied the passivating treatments.

The reducing the corrosion rate of the zinc layer, in the past, a very common and popular way was chromate conversion coating based on Cr^{6+}. This could increase the passivation tendency of zinc layer. However, hexavalent chromium is regarded as toxic and cancer-producing, there are environmental and health risks associated with the use of chromate ions [1, 2]. Therefore, all hexavalent chromates have been banned by the EC and have been generally replaced by other chromium-free passivates [3 - 6].

As potential alternatives to hexavalent chromium was studied several passivating inhibitors like molybdates, tungstates, permanganates, vanadates, and organic compounds [7, 8].

The phosphating is one of the most important chemical conversion processes used for corrosion protection or painting primer for the galvanized layers [9 - 11]. Zinc phosphate is used as main component for the passivating solutions. Molybdate can be added for the deposition of a superior zinc phosphate coating. This is an environmentally acceptable and effective corrosion inhibitor for galvanized steel [12, 13].

The molybdate additives into phosphate solution lead to accelerate the phosphating processes or to improve the corrosion resistance of phosphate coatings [14 - 16].

Molybdate films are amorphous, but they have cracks during a longer immersion [17]. As result were proposed molybdate–phosphate solutions. The molybdate–phosphate system was introduced by Tang et al. for corrosion protection of galvanized steel [18].

Other studies have been suggested that molybdate-phosphate based conversion coatings are an attractive alternative to chromate conversion coatings [19, 20]. For building films of significant thickness the presence of fluoride ions is also important [21].

In this paper are presented the results of study about the utilization of three molybdate–phosphate passivation solutions with different compositions to enhance the properties of coatings on the surface of galvanized steel sheets.

The treatments realized at different concentrations and dipped times were analyzed.

Also the corrosion resistance in sea water solution of the passivating samples has been studied and discussed. Was make a comparative analyzes of corrosion rates for different passivation solutions and different times of exposure in corrosion medium.

2. Experimental method and materials

More series of rectangular galvanized steel sheet samples were used. Zinc protective coating was obtained by hot dip galvanized process.

Before passivation the specimens were cleaned sequentially. The galvanized steel samples were degreased with acetone. The surface that has been subjected to phosphating was rinsed with deionized water to remove any residue and non-adherent particles present on it. After rinsing the samples were dried. The zinc phosphate coating is applied by immersion of samples in a zinc phosphate solution. After the passivating film is deposited, the steel samples are removed from solution and then thoroughly rinsed and dried.

The solution used for coatings obtaining was prepared with zinc dihydrogen phosphate ($Zn(H_2PO_4)_2$). Also molybdate diamonium ($(NH_4)_2MoO_4$) as source of molybdenum ions was added. Fluotitanic acid (H_2TiF_60) for pH correction and source of active ion Ti for activation passivating process was added in solution.

Table 1. *Composition of the phosphating solutions used in this work*

Code of treatment solution	Zinc dihydrogen phosphate	Fluotitanic acid	Molybdate diamonium
	[g/L]		
I	30	10	10
II	45	15	15
III	90	30	30

Three compositional variants for the passivation solution that has been applied on the surface of galvanized steel sheet samples are given in Table 1. The specimens were dipped in each passivating solution (open to air) at room temperature for 10, 15, 20, 30 and 60 seconds.

The corrosion properties of passivated samples have been tested by their exposing in the sea water solution as corrosion medium for different exposure times. The solution for corrosion tests have 27g/L NaCl, 6g/L $MgCl_2$, 1g/L $CaCl_2$, 1g/L KCl at pH = 6.5-7.2. The protective properties of the molybdate–phosphate conversion coatings obtained for those three passivating solutions and different exposure times (168, 336, 504, 672 and, 840 h) have been evaluated by corrosion rates measurements.

3. Results and discussions

To evaluate the quality of molybdate–phosphate conversion coatings the physical characteristics as well as the performance in corrosive environment were determined.

Firstly was analyzed the physical characteristics of passivating films. To determine the passivated coating thickness the determination of coating weight was adopted.

Table 2. *Passivated coating thickness as coating weight in g/m^2 at increasing immersion time*

Immersion time in s	Coating thickness as coating weight in g/m^2 for:		
	Solution I	Solution II	Solution III
10	1.314	3.775	12.375
15	1.579	3.85	8.204
20	3.256	2.318	9.414
30	2.06	2.95	8.979
60	2.11	3.595	7.97

This method involves the determination of change in weight of a coated specimen after immersion in the treatment medium.

The difference in weight after coating and before is divided by the surface area of sample in m^2 to obtain unit coating weight in g/m^2. The time evolution of the layer thickness corresponding to the samples dipped into the three solutions is presented in Table 2, respectively Figure 1.

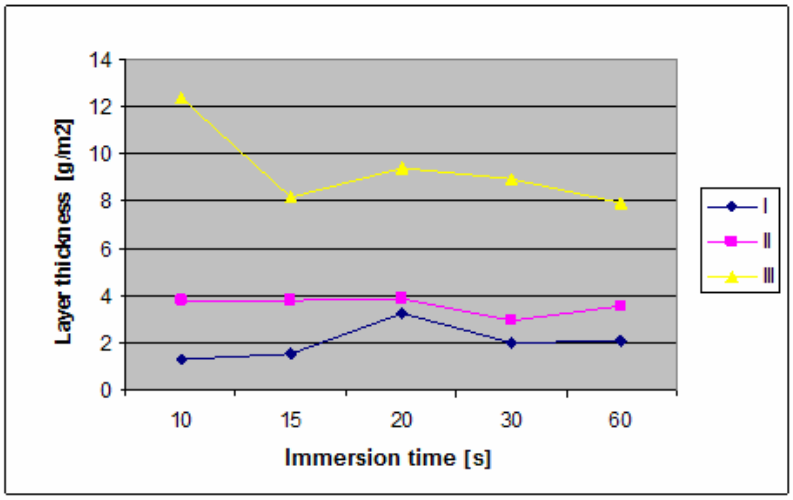

Fig. 1. *Layer thickness of molybdate–phosphate conversion coatings as a function of duration of immersion for different passivating solutions.*

The thicknesses of conversion films obtained at different immersion times and the composition of the passivating solutions have been different. The thicker film was obtained for the solution III with higher phosphate and molybdate addition. At prolongation of the immersion time a slowly reducing of the thicknesses of the layers was observed for all solutions. For the treatments developed into all solutions the films were developed rapidly. In simple passivating solutions, phosphating reaction tends to be slow owing to the polarization caused by the hydrogen evolved in the cathodic reaction. To achieve coating formation in a practicable time for classical phosphating solution, some mode of acceleration must be employed. For this study the chemical additives were added into zinc phosphate solution and their action was evidently. Molybdenum and titanium compounds were added into phosphating bath as chemical accelerators. For all solutions after short immersion times (~15-20s) were obtained stable thicknesses for layers.

The length of period for developing of a stable film corresponds with the first stage in coating formation (namely, the induction stage) into classical phosphating process. For developing a stable layer is observed that the classical phosphating process involves more time.

The process for the coating formation care divided into four distinct stages: the induction stage, the commencement of film growth, the main exponential growth stage and the stage of linear increase in film growth [22].

The quality of passivating process for different solutions and immersion times was analyzed by examination of physical appearance of coated surfaces of samples. The surface morphologies of the molybdate-phosphate films are presented in the Figure 2-4.

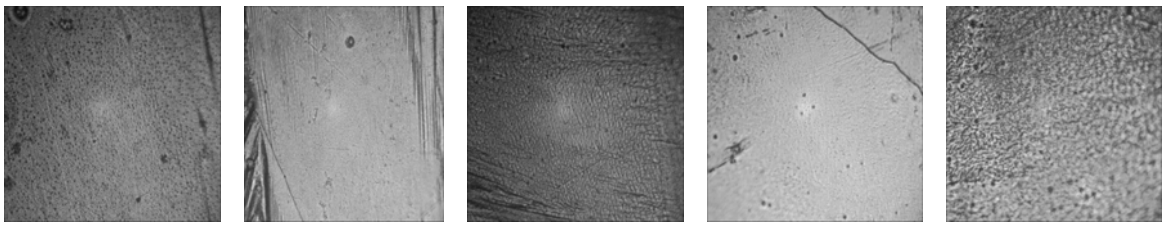

a) *b)* *c)* *d)* *e)*

Fig. 2. *Surface appearance of passivating layer for solution I at different immersion times: 10 (a), 15 (b), 20 (c), 30 (d) and, 60s (e).*

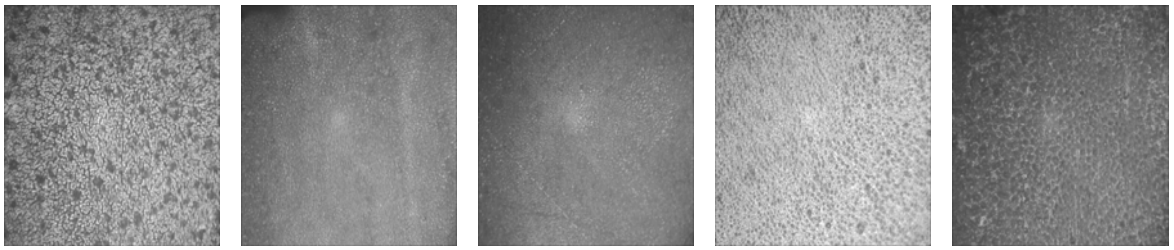

a) *b)* *c)* *d)* *e)*

Fig.3. *Surface appearance of passivating layer for solution II at different immersion times: 10 (a), 15 (b), 20 (c), 30 (d) and, 60s (e).*

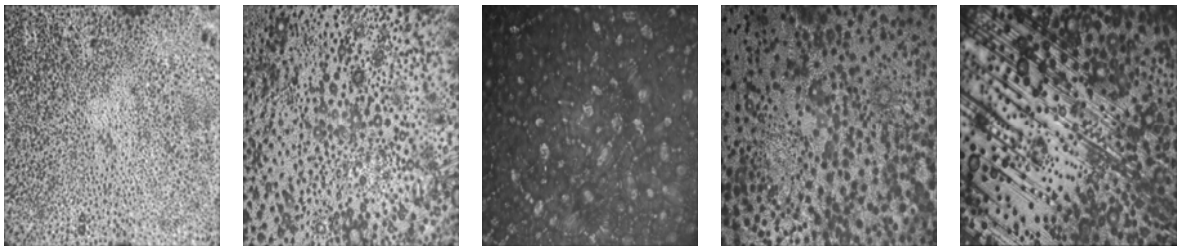

a) *b)* *c)* *d)* *e)*

Fig.4. *Surface appearance of passivating layer for solution III at different immersion times: 10 (a), 15 (b), 20 (c), 30 (d) and, 60s (e).*

During the treatment the surface is in contact with the phosphate solution that dissolves a small amount of the coating. At the surface of the zinc, the attack of the zinc phosphate produces a localized increase in the pH, resulting in the precipitation and deposition of insoluble zinc phosphate crystals on the surface of the zinc coating.

After some time of reaction developing, this crystallizing action leaves behind a continuous, relatively thick solid film of zinc phosphate.

The phosphate films on surface of hot dip galvanizing steel may range in colors from light gray to dark gray, depending on the type of bath and the grade of steel substrate used. The chemical additives can generated the depositions with other colors. The layers obtained in the experimental are have yellowish green color for solution I and green for solution III.

For solution I at all immersion times tested the passivating film obtained is uniform and adherent.

For obtaining an optimum surface appearance at dipping into solution II was necessary an immersion time in range of 15-20s. This is lower than the corresponding immersion in solution I.

The solution III has a higher content of dihydrogen phosphate and as result the passivating reaction is more intensive.

As result a thicker layer was developed. Because over 20s the layer becomes less uniform and adherent must be established the optimum immersion time. In respect to these parameters of the passivating treatments (the composition of the solutions and immersion times) can concluded that a bigger thickness was obtained for a solution enriched in phosphate and for controllable immersion time. More phosphate addition negatively affects the coating. Sometimes for solution III was obtained non uniform and rough layers. Also uncovered areas were observed.

It is generally accepted that the composition of the phosphate layer has a strong influence on its chemical stability. For this reason in this study this was analyzed by corrosion tests at which were subjected the samples after the passivating treatments.

Is knows that the passivity (or reactivity) of the molybdate–phosphate layer at interaction with a corrosive medium is an important property of conversion layer. In order to determine the corrosion speeds in sea water medium the samples (obtained at different passivating treatments and different immersion times) were maintained at room temperature in sea water solution with 27g/L NaCl, 6g/L MgCl2, 1g/L CaCl2, 1g/L KCl, pH = 7.1.

The corrosion speeds were measured for different exposure times in corrosion medium: 168, 336, 504, 672 and 840 h. The results of experiment are given in comparison charts, Figure 5.

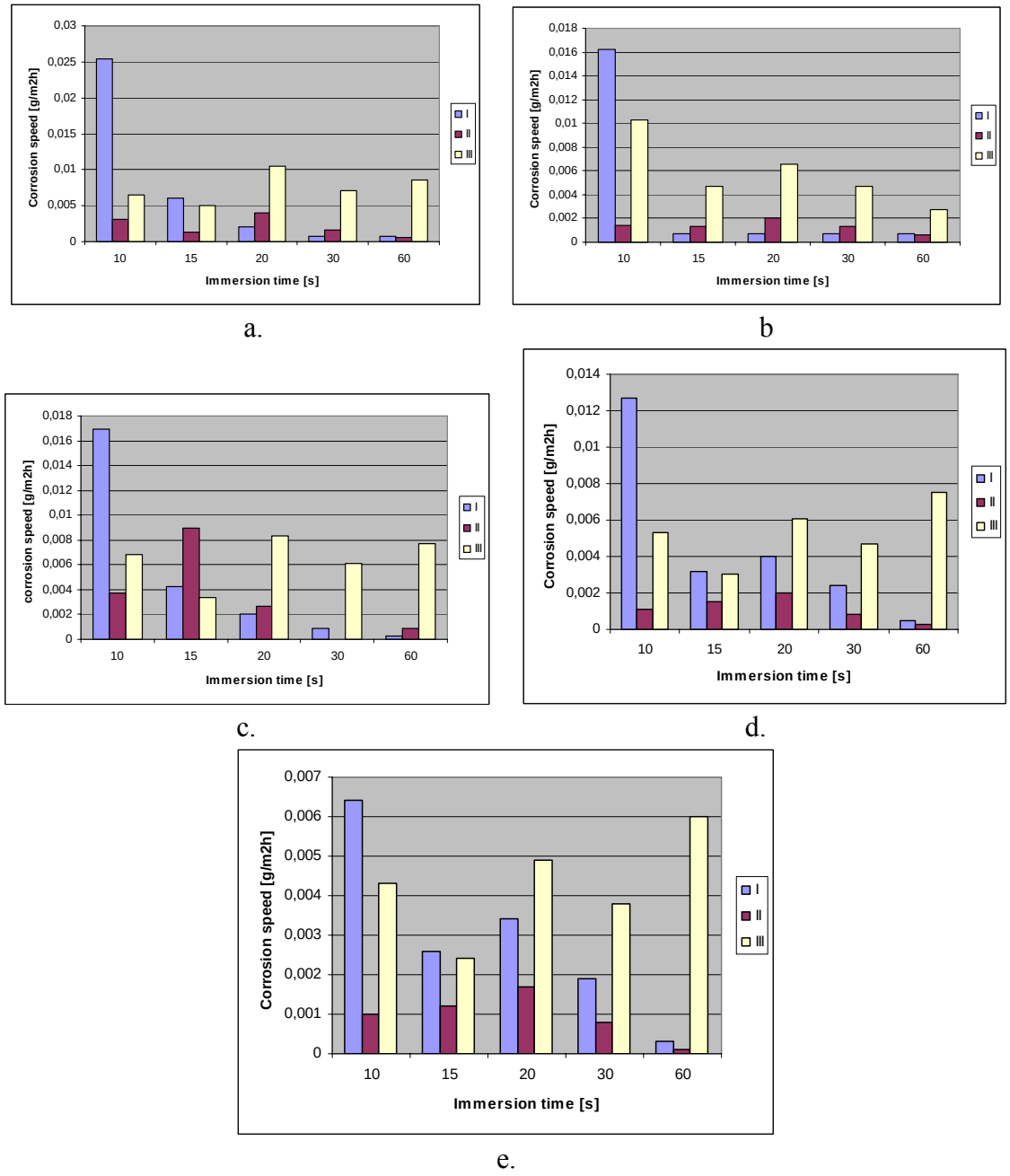

Fig.5. *Comparison chart of corrosion speeds for different passivation solutions and different immersion times at variation of exposure time in corrosion medium: 168 (a), 336 (b), 504 (c), 672 (d) and, 840 hours (e).*

By selecting the results for corrosion tests obtained for the three passivating solutions and variable immersion times in these solutions was possible to choose the better treatment, Figure 6.

For solution III was obtained passivation layer the thickest but it did not show the best resistance to corrosion. This explication is done by the quality of the layer developed at higher phosphate content into passivating solution.

Can be observed that for passivation solution with more molybdate–phosphate content the corrosion rate slowly decreases with exposure time into corrosion medium.

For the other solutions the corrosion speeds are lower and appreciatively remain at these lower values at prolongation of exposure time.

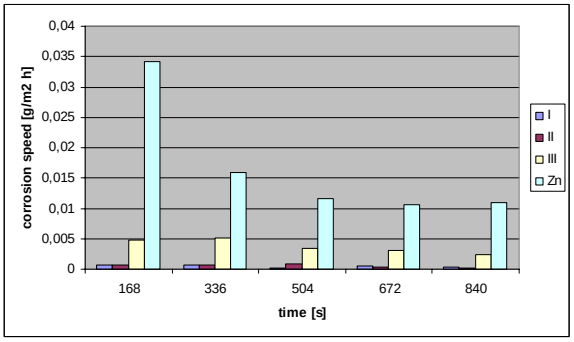

Fig.6. *Variation of the corrosion speed as a function of the exposure time to the corrosive environment.*

4. Conclusions

The surface quality of the passivating hot dip galvanized steel sheet is important for its corrosion behavior.

The thickness of passivating coating obtained on galvanized steel surface varies with immersion times and phosphating compounds added. The addition of chemical additives influences the process. Comparatively with the classic process the times required for forming of continuous and solid molybdate-phosphate films were lower and their color was yellowish green or green. The passivating process was developed rapidly.

The thickness of molybdate–phosphate conversion coatings depends by chemical composition of the passivating solutions and by times of immersion.

The thickness of layer is higher for solution III, minimum for the solution I and, medium for solution II. The solution with the following chemical composition zinc dihydrogen phosphate 45g/L fluotitanic acid 15g/L, molybdate diamonium 15g/L and immersion time of 60 second gives the best corrosion resistance. The appearance of the corroded surfaces for all the samples shows a general and uniform corrosion.

References

[1]. **Lunder O., Walmsley J.C., Mack P., and Nisancioglu K. -** *Formation and characterisation of a chromate conversion coating on AA6060 aluminium*, Corros. Sci., 2005, 47: 1604

[2]. **LIU Guangming, YU Fei, Yang Liu, Tian Jihong, and DU Nan** - *Cerium-tannic acid passivation treatment on galvanized steel, Cerium-tannic acid passivation treatment on galvanized steel Rare Metals*, Vol. 28, No. 3, Jun 2009, p. 284

[3]. Hao J.J., An C.Q., and Mou S.H. - *Advances in research on unchromium passivation of galvanized zinc layer,* Mater.Rev., 2003, 9 (17)

[4]. Thierry L., Pommier N. - *Hexavalent chromium-free passivation treatments in the automotive industry,* COVENTYA SAS, April 2003

[5]. Yunying Fan, Yehua Jiang, Rong Zhou - *New passivating method to galvanized Zn coatings on steel substrate,* Advanced Materials Research Vols.163-167 (2011), pp.4555-4558

[6]. Wang D. and Tang X. - *A study of the film formation kin etics on zinc in different acidic corrosion inhibitor solutions by quartz crystal microbalance*, *Corros. Sci.*, 2005, 9 (47): 2157

[7]. Bexell U. and Grehk T.M. - *A corrosion study of hot-dip galvanized steel sheet pre-treated with γ-mercaptopropyltrimethoxysilane, Surf. Coat. Technol.*, 2007, **201**: 4734

[8]. Deflorian F., Rossi S., Fedrizzi L., and Bonora P.L. - *EIS study of organic coating on zinc surface pretreated with environmentally friendly products*, *Prog. Org. Coat.*, 2005, **52**: 271.]. The phosphating is one of the most important chemical conversion processes used for corrosion protection or painting primer for the galvanized layers

[9]. Lorin G. - *Phosphating of metals: constitution, physical chemistry and technical applications of phosphating solutions* [M]. Hampton Hill: Finishing Publications, 1974: 146−155

[10]. Freeman D B. - *Phosphating and metal pre-treatment* [M]. New York: Industrial Press, 1986: 134−139

[11]. Rausch W. - *The phosphating of metals* [M]. Ohio: ASM International, 1990: 112−116.1−3

[12]. Vukasovich M S, Farr J P G. - *Molybdatein corrosion inhibition*—A review [J]. Mater Perform, 1986, 25(5): 9−18

[13]. Aramaki K. - *The inhibition effects of chromate-free, anion inhibitors on corrosion of zinc in aerated* 0.5 mol/L NaCl [J]. Corros.Sci, 2001, 43(3): 591−604

[14]. Li Guang-yu, Niu Li-yuan, lian Jian-she, Jiang Zhong-Hao - *A black phosphate coating for C1008 steel* [J]. Surf Coat Technol, 2004, 176(2): 215−221

[15]. Saliba-Silva A M, de Oliveira M C L, Costa I. - *Effect of molybdate on phosphating of Nd-Fe-B magnets for corrosion protection* [J]. Mater Res Bull, 2005, 8(2): 147−150

[16]. Lin Bi-lan, Lu Jin-tang, **Kong Gang, Liu Jun.** *Growth and corrosion resistance of molybdate modified zinc phosphate* conversion coatings on hot-dip galvanized steel [J]. Trans Nonferrous Met Soc China, 2007, 17(4): 755−761

[17]. Lu Jin-tang, Kong Gang, Chen Jin-Hong, Xu Qiao-Yu, Sui Run-Zhou. - *Growth and corrosion behavior of molybate passivation film on hot dip galvanized steel* [J]. Trans Nonferrous Met Soc China, 2003, 13(1): 145−148

[18]. Tang T. and Beth-Nielsen G. - *Molybdate-based alternatives to chromating as a passivation treatment for zinc, Plat. Surf.Finish*., 1994, **18** (11): 20

[19]. Ogle K., Tomandl A., Meddahi N., Wolpers M. - *The alkaline stability of phosphate coatings I: ICP atomic emission spectroelectrochemistry*, Corrosion Science 46 (2004) pp.979–995

[20]. Ogle K., Bucheit R. - *Conversion coatings, in: A.J. Bard, M. Stratmann* (Eds.), Encyclopedia of the Electrochemistry, vol. 5, Wiley-VCH, Weinheim, 2003, p. 460

[21]. Brooman E.W. - *Chromium alloy plating*, ASM Handb Int. 5 (1994) 270

[22]. Sankara Narayanan T.S.N. - *Surface Pretreatment By Phosphate Conversion Coatings.* A REVIEW, Rev.Adv.Mater.Sci. 9 (2005) 130-177.

THE ANNALS OF "DUNAREA DE JOS" UNIVERSITY OF GALATI.
FASCICLE IX. METALLURGY AND MATERIALS SCIENCE
N^0. 4 – 2011, ISSN 1453 – 083X

MATHEMATICAL MODELING OF THERMOMECHANICAL TREATMENT PROCESS APPLIED TO ALUMINUM BASE ALLOYS FOR AERONAUTICS

Marian NEACSU, Doru HANGANU, Elisabeta VASILESCU
„Dunarea de Jos" University of Galati
email: uscaeni@yahoo.com

ABSTRACT

To optimize the thermo-mechanical processing of aluminum base alloys, mathematical modeling was used in a laborious research program by planned experiment of thermomechanical treatment process applied to an Al-Zn system alloy. The paper presents the modeling stages, the type of mathematical model that allows for the analysis of the main influences (technological parameters),their influence size and the type of correlationsbetween them. The simulation of the thermomechanical treatment process by varying the process parameters within the tested values and thermomechanical treatment optimization (getting the optimal complex of strength and plasticity properties in a convenient treatment option) is possible using the mathematical model developed.

KEYWORDS: mathematical model, aluminum alloy, thermomechanical treatments

Introduction

Mathematical modeling means transposing of a real physical process into a mathematized form. The construction of the models associated to processes and systems is a vital part of the simulation process, being absolutely necessary to distinguish between different types of models that can be used by analysts. Process modeling can be considered as consisting of two stages: one that specifies the form under which the model must be expressed, and the second describing how it is used to provide a series of predictions or provide the optimal solution of the problem studied. In this paper we conducted the mathematical model of thermomechanical treatment process applied to alloys studied by statistical methods i.e. regression analysis by active experiment.

Currently, the most effective methods for programming the experiment are those concerning solving extreme problems involving the determination of levels of independent quantities (input), u1, u2,...uk, for which the objective function:

$$y = f(u_1, u_2, ..., u_k) \quad (1)$$

has extreme values (maximum or minimum) as well as the calculation of these values.

For each basic factor the base levels, u_{01}, u_{02} respectively u_{03}, are determined, whichare actually thecoordinates in the factorial space of the randomlychosen starting point as well as the ranges Δu_1, Δu_2 and Δu_3. By addingthe variation interval to the basic level, the superior level is obtained, and by lowering it the inferior level of the factor is obtained. If the encoded value of ui factor is denoted by xi, resulting from the relationship:

$$x_i = \frac{u_i - u_{0i}}{\Delta u_i}$$

the higher level will be coded with a score, the lower by -1, and the basic level to 0.

Experimental conditions

In the case of high strength aluminum alloy AlZn5.7Mg2.6 processed according to the schedule in Figure 1, in which the solution hardening involves primarily hardening compounds leaching, a process that takes place through activation of diffusion phenomena in solid form, taking into account diffusion laws, it can be said that the solution temperature and the maintaining time at this temperature will have a decisive influence on the

effectiveness of treatment by their influence on the diffusion coefficients and on the process dynamics.

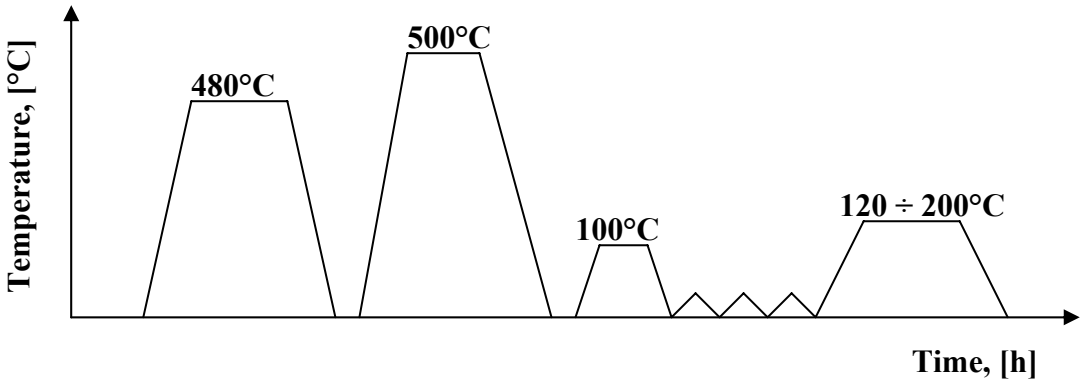

Fig.1 *Technological scheme of achieving experiments*
I-homogenization; II-solution hardening; III -artificial aging;
IV - cold plastic deformation, V - artificial aging

Cold plastic deformation was experimented with three different degrees of deformation, namely: ε1 = 10%, ε2 = ε3 = 20% and 30%. In this way the hard compounds deform (elongate in the direction of the deformation) or crumble.

Given the above, the following factors will be considered as process parameters: 1- artificial aging temperature - T, [° C]; 2- maintaining time – τ [h]; 3- the degree of deformation – ε [%].

Table 1 shows the correspondence between different levels of the factors expressed in natural values with those expressed in coded values for the three factors used in the thermomechanical treatment process.

Table 1. *Correspondence between the values of the factors expressed in natural and coded units [1]*

Factor	Process temperature		Process time		The degree of deformation	
	Natural units, in ° C	Values coded	Natural units, in hours	Values coded	Natural units, in hours	Values coded
Base level	$u_{01} = 160$	$\frac{160-160}{40} = 0$	$u_{02} = 12$	$\frac{12-12}{4} = 0$	$u_{03} = 20$	$\frac{20-20}{10} = 0$
The ranges	$\Delta u_1 = 40$	0	$\Delta u_2 = 8$	0	$\Delta u_3 = 10$	0
Higher	$u_{1s} = 200$	$\frac{200-160}{40} = +1$	$u_{2s} = 20$	$\frac{20-12}{8} = +1$	$u_{3s} = 30$	$\frac{30-20}{10} = +1$
Lower	$u_{1i} = 120$	$\frac{120-160}{40} = -1$	$u_{2i} = 4$	$\frac{12-20}{8} = -1$	$u_{3i} = 10$	$\frac{10-20}{10} = -1$

In the coded representation of the experiment the following notations and symbols were used:
• x1 – artificial aging temperature, T, ° C;
• x2 – mentaining time, τ, [h];
• x3- deformation degree, ε [%];
• Y1 - tensile strength, Rm, [MPa];
• Y2 - yield strength, Rp02 [MPa];
• Y3 – specific elongation at break, A5, [%];
• Y4 - hardness, HB;

Between the natural and coded values of x_i factors there are the following linking relations:

$$x_1 = \frac{t - t_0}{\Delta t},\ x_2 = \frac{\tau - \tau_0}{\Delta \tau},\ x_3 = \frac{\varepsilon - \varepsilon_0}{\Delta \varepsilon}, \qquad (2)$$

To determine the dispersion of results reproducibility , six experiments were performed at the basic levels of the factors. In this way a full factorial experiment of the type 2^3 was performed as shown inTable 2.

Table 2. *Matrix determination for the factorial experiment of the type 2^3 [1]*

Nr. exp.	X_0	X_1	X_2	X_3	X_1X_2	X_1X_3	X_2X_3	Y_1	Y_2	Y_3	Y_4
1	+1	+1	+1	+1	+1	+1	+1	487	424	8,1	135
2	+1	-1	+1	+1	-1	-1	+1	630	591	6,8	194
3	+1	+1	-1	+1	-1	+1	-1	455	384	8,7	122
4	+1	-1	-1	+1	+1	-1	-1	569	516	7,7	155
5	+1	+1	+1	-1	+1	-1	-1	435	391	10,4	121
6	+1	-1	+1	-1	-1	+1	-1	577	531	8,4	171
7	+1	+1	-1	-1	-1	-1	+1	411	377	11,0	109
8	+1	-1	-1	-1	+1	+1	+1	507	468	9,5	135
9	+1	0	0	0	0	0	0	498	452	10.0	123
10	+1	0	0	0	0	0	0	512	473	9,0	145
11	+1	0	0	0	0	0	0	506	459	8,9	143
12	+1	0	0	0	0	0	0	503	456	8,5	140
13	+1	0	0	0	0	0	0	514	475	9,2	148
14	+1	0	0	0	0	0	0	509	462	9,1	144

Considering the function Yi as the analytical expression of the order I model, that is:

$$Y_i = c_0 + \sum_{i=1}^{3} c_i \cdot x_i + \sum_{\substack{i=1 \\ j=1 \\ i \neq j}}^{3} c_{ij} x_i x_j \qquad (3)$$

Equation (3) is written as matrix form:

$$Y = X \cdot C \qquad (4)$$

where: X is the matrix of experimental conditions

$$X = \begin{Vmatrix} x_{01} & x_{11} & x_{21} & \dots & x_{m1} \\ x_{02} & x_{12} & x_{22} & \dots & x_{m2} \\ x_{03} & x_{13} & x_{23} & \dots & x_{m3} \\ \dots & \dots & \dots & \dots & \dots \\ x_{0n} & x_{1n} & x_{2n} & \dots & x_{mn} \end{Vmatrix}$$

m - number of terms of equation (3);
n - number of considered experiences;
C – column vector of coefficients c_i
C = [c0, c1,..., cn] T
T – matrix transposition symbol
Y - matrix of experimental results

$$\mathbf{Y} = [\, Y_1 , Y_2 , \dots , Y_n \,]^T \qquad (5)$$

where : Y_1 = [487 630 455 569 435 577 411 507 498 512 506 503 514 509]
Y_2 = [424 591 384 516 391 531 377 468 452 473 459 456 475 462]
Y_3 = [8,1 6,8 8,7 7,7 10,4 8,4 11 9,5 10 9 8,9 8,5 9,2 9.1]
Y_4 =[135 194 122 155 121 171 109 135 123 145 143 140 148 144]

For this case, the linear function (3) has a particular form:

$$Y_i = c_0 + c_1 \cdot x_1 + c_2 \cdot x_2 + c_3 \cdot x_3 + c_{12} \cdot x_1 \cdot x_2 + c_{13} x_1 \cdot x_3 + c_{23} \cdot x_2 \cdot x_3 \qquad (6)$$

Multiplying at the left side each term of the matrix equation by unitary matrix

$$E = [XT\ X]^{-1} \times XT \qquad (7)$$

there follows:

$$C = [XT\ X \times]^{-1} [XT\ x\ Y] \qquad (8)$$

expression that represents the relationship for calculating the coefficients of regression equation. Using the values in Table 2, based on relation (8), first order models coefficients are obtained, summarized in Table 3.

Table 3. *Values of first-order models coefficients*

c_i \ Y_i	Y_1	Y_2	Y_3	Y_4
c_0	508.0714	461.3571	8.95	141.7857
c_1	-61.875	-66.25	0.725	-21
c_2	23.375	24	-0.4	12.5
c_3	26.375	18.5	-1	8.75
c_{12}	-9.375	-10.5	0.1	-6.25
c_{13}	-2.375	-8.5	-0.15	-2
c_{23}	-0.125	4.75	0.025	0.5

Therefore the mathematical model of first-order equation (7) for each property in part, is:

$$Y_1 = 508{,}0714 - 61{,}875 \cdot x_1 + 23{,}375 \cdot x_2 + 26{,}375 \cdot x_3 - 9{,}375 \cdot x_1 \cdot x_2 - 2{,}375 \cdot x_1 \cdot x_3 - 0{,}125 \cdot x_2 \cdot x_3 \quad (9)$$

$$Y_2 = 461{,}3571 - 66{,}25 \cdot x_1 + 24 \cdot x_2 + 18{,}5 \cdot x_3 - 10{,}5 \cdot x_1 \cdot x_2 - 8{,}5 \cdot x_1 \cdot x_3 + 4{,}75 \cdot x_2 \cdot x_3 \quad (10)$$

$$Y_3 = 8{,}95 + 0{,}725 \cdot x_1 - 0{,}4 \cdot x_2 - \cdot x_3 + 0{,}1 \cdot x_1 \cdot x_2 - 0{,}15 x_1 \cdot x_3 + 0{,}025 \cdot x_2 \cdot x_3 \quad (11)$$

$$Y_4 = 141{,}7857 - 21 \cdot x_1 + 12{,}5 \cdot x_2 + 8{,}75 \cdot x_3 - 6{,}25 \cdot x_1 \cdot x_2 - 2 x_1 \cdot x_3 + 0{,}5 \cdot x_2 \cdot x_3 \quad (12)$$

By replacing the variables xi with relations (2) and doing the respective calculations in the above equations, the following equations are obtained representing expressions of mathematical first –order models for the four properties considered:

$$Y_1(t,\tau,\varepsilon) = 592{,}1339 - 1{,}0766\, t + 7{,}6406\, \tau + 3{,}6063\, \varepsilon - 0{,}0293\, t \cdot \tau - 0{,}0059\, t \cdot \varepsilon - 0{,}0016\, \tau \cdot \varepsilon \quad (13)$$

$$Y_2(t,\tau,\varepsilon) = 536{,}621 - 0{,}8375 t + 7{,}0625\, \tau + 4{,}5375\, \varepsilon - 0{,}0328 t \cdot \tau - 0{,}0213 t \cdot \varepsilon + 0{,}0594\, \tau \cdot \varepsilon \quad (14)$$

$$Y_3(t,\tau,\varepsilon) = 8{,}125 + 0{,}0219 \cdot t - 0{,}1063 \cdot \tau - 0{,}0438 \cdot \varepsilon + 0{,}0003 \cdot t \cdot \tau - 0{,}0004 \cdot t \cdot \varepsilon + 0{,}0003 \cdot \tau \cdot \varepsilon \quad (15)$$

$$Y_4(t,\tau,\varepsilon) = 137{,}5357 - 0{,}1906\, t + 4{,}5625\, \tau + 1{,}6 \cdot \varepsilon - 0{,}0195\, t \cdot \tau - 0{,}005 t \cdot \varepsilon + 0{,}0063\, \tau \cdot \varepsilon \quad (16)$$

First-order mathematical models have been verified statistically, using Fischer criterion to decide if they can be used for studying the analysed process or if it is necessary to determine the higher order models.

The values calculated using Fischer criterion for the four first order mathematical models are summarized in Table 4.

Table 4 shows that all models are consistent with the experimental data and can be used in process optimization.

To verify the significance of coefficients for the appropriate model, the following ratio is determined for each coefficient:

$$F_{csi} = \frac{PM_{bi}}{PM_{rez}}$$

Table 4. *Calculation data for checking model adequacy*

Calculated values	Y_1	Y_2	Y_3	Y_4
SP_{rez}	224.1752	478.2142	1.525	419.3571
PM_{rez}	32.025	68.316	0.22	59.90815714
SP_{er}	176	430.8333	1.2283	401.5000
PM_{er}	35.2	86.16666	0.2457	80.3
SP_{in}	48.1752	47.3809	0.2967	17.8571
PM_{in}	24.0876	23.69045	0.1484	8.92855
F_{ci}	0.6843	0.275	0.60388	0.11118991
Accordance	Concorde	Concorde	Concorde	Concorde

Where PMrez is the average square of reziduals calculated in Table 4 PM_{bi} is the average square of the coefficients which are calculated with the matrix relation

*PM*bi = *D (X ^{t} Y)*, where D is the diagonal matrix with the model coefficients as the main diagonal elements, the other elements of the matrix being null.

X is the matrix of experimental conditions at the considered levels (-1, 0, 1)

Y – the matrix of experimental results at the levels considered (-1, 0, 1) Using equation (17) we obtain the values of the Fcsi ratio for the model coefficients shown in Table 4.

Coefficients c_i for which Fcsi> FT [1, frez, (1-α)%] are considered significant; in this case FT (1, 7, 95%) = 5.79.

Thus the four equations become:

$$Y_1(t,\tau,\varepsilon) = 611{,}51 - 1{,}195 \cdot t + 7{,}609 \cdot \tau + 2{,}64 \cdot \varepsilon - 0{,}029 \cdot t \cdot \tau \quad (18)$$

$$Y_2(t,\tau,\varepsilon) = 590{,}371 - 1{,}262 \cdot t + 8.25 \cdot \tau + 1{,}85 \cdot \varepsilon - 0{,}032 \cdot t \cdot \tau \quad (19)$$

$$Y_3(t,\tau,\varepsilon) = 8{,}65 + 0{,}018 \cdot t - 0{,}05 \cdot \tau - 0{,}1 \cdot \varepsilon \quad (20)$$

$$Y_4(t,\tau,\varepsilon) = 189{,}535 - 0{,}525 \cdot t + 1{,}562 \cdot \tau + 0{,}875 \cdot \varepsilon \quad (21)$$

Equations (in t, τ and ε) (18), (19), (20) and (21) are valid for t = 120 ... 200 °C, τ = 4 ... 20 hours and ε = 10 .. .30%. Using relations (18), (19), (20) and (21) for examplification, we have drawn graphs of variation of each property function of time for a treatment temperature of 160 ° C, in the case of the deformed alloy where the degree of deformation is - 20%.

As shown in Figures 2 ÷5 mechanical property values determined by calculations using mathematical models are close to the experimentally determined values. This is the proof that the mathematical modeling achieved allow for simulation of thermomechanical treatment process con- ducted according to the scheme in Figure 1.

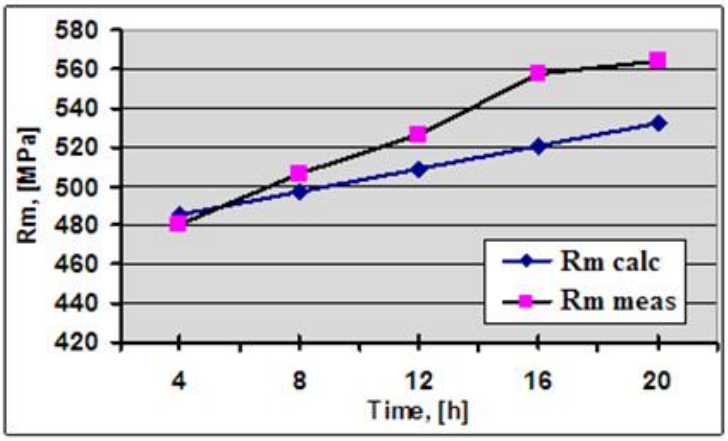

Fig.2. *Variation of mechanical resistance according to treatment time.*

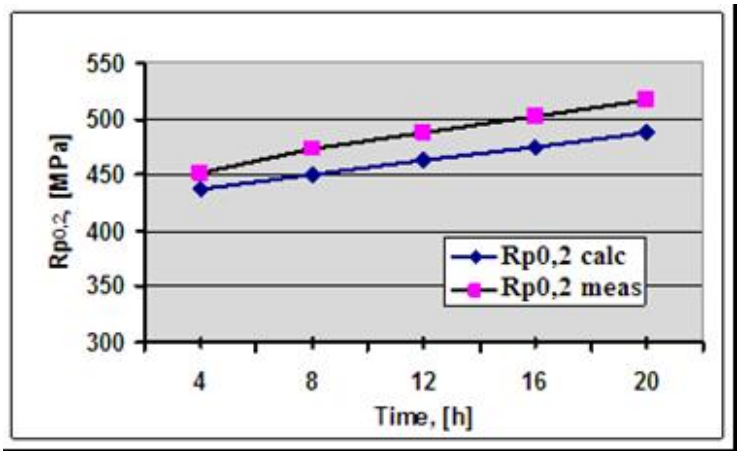

Fig.3. *Variation of yield stress with treatment time.*

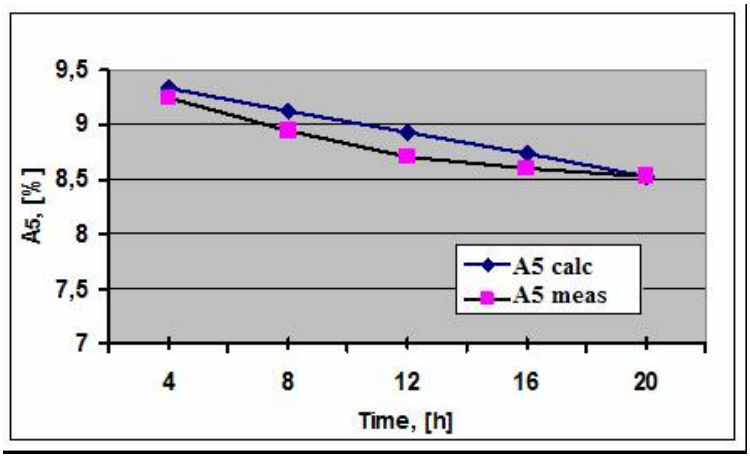

Fig.4. *Variation of elongation at break with treatment time.*

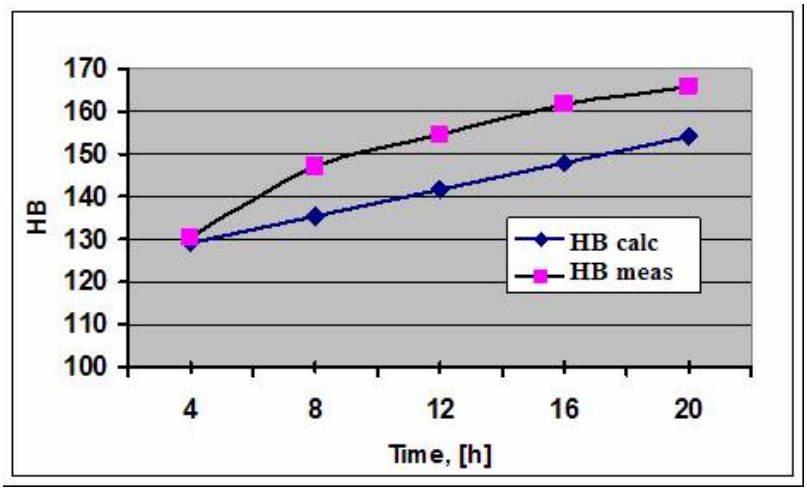

Fig.5. *Brinell hardness variation with treatment time.*

Conclusions

The mathematical model presented in the set of equations (30)÷(33) allows simulation of thermomechanical treatment process, by varying the process parameters values, within experimental limits.

The aging factor has the biggest influence on the increase of mechanical strength as the value of the influence factor coefficient is positive and of the highest value. The next important influencing factor is the degree of cold plastic deformation, as the coefficient of this factor shows, mechanical strength properties increase as the degree of deformation value increases. The value of the temperature parameter coefficient indicates that when the temperature increases, there is a decrease in strength properties.

Elongation at break is influenced according to the model, first by treatment temperature, meaning that as treatment temperature increases, the elongation increases too. From the analysis of the regression equations obtained, it results that an increase in the final aging temperature, in the range considered, above 180 C will lead to lower strength characteristics (tensile strength, yield strength and hardness); instead the plasticity increases (relative elongation increases to some extent with increasing aging temperature).

Mechanical strength depending on aging time increases with time, and elongation at break decreases.

Regarding the influence of the degree of deformation on the properties of resistance (Rm, Rp02 and hardness) that they have higher values than those prescribed by EN 485-2-2007, for all three degrees of deformation.

The mathematical model presented allows for establishing the technological conditions that can lead to obtaining the optimal properties complex of strength and plasticity, in alternative technology involving minimal costs.

References

[1]. Taloi D, Florian E, Bratu C.- *Optimizarea proceselor metalurgice* Editura Didactică si Pedagogică, Bucureşti 1983
[2]. Baron, T. s.a. - *Statistică teoretică şi economică.* Editura Didactică şi Pedagogică, Bucureşti, 1995.
[3]. Naisnith, S.J. - *Encyclopedie dictionary of mathematics for engineers and applied scientists*. Editura S.J.N, Oxford, 1986.
[4]. Nistor, L. ş. a. - *Modelarea formei secţiunii transversale a laminatului prin optimizarea puterii consumate în procesul de laminare pe principiul metodei de calcul variaţional.* Metalurgia nr. 5, 1995.

THE ANNALS OF "DUNAREA DE JOS" UNIVERSITY OF GALATI.
FASCICLE IX. METALLURGY AND MATERIALS SCIENCE
N^0. 4 – 2011, ISSN 1453 – 083X

OPPORTUNITIES TO ANALYSE THE POLLUTION IN METALLURGICAL INDUSTRY

Avram NICOLAE, Cristian PREDESCU, Andrei BERBECARU, Maria NICOLAE
"Politehnica" University of Bucharest
email: avramnicolae73@yahoo.com

ABSTRACT

The metallurgical industry is a highly polluting economic sector. In order to establish measures to minimise the pollution, new methods are needed to analyse such processes.

This article analyses the following possibilities:

- *thermodynamic analysis;*
- *analysis with system theory elements;*
- *characterization of pollution as global phenomenon of soiling;*
- *possibilities of maintaining a balance between the economic development and pollution.*

KEYWORDS: pollution, analysis, life cycle

1. Introduction

In metallurgy, the life cycle phases of a product we are mostly interested are:

- **product manufacturing**, in which the material resources and energy, through the technological process, are transformed into product;
- **use of the product**, in which, through the *disintegration of the material and scrapping* (by destruction) of the product, it is transformed into secondary material (waste).

Both phases, objectively, generate pollutants. Some of pollution assessment methodologies that can be used for scientific and practical purposes are represented by:

- thermodynamic analysis;
- analysis with system theory elements;
- characterization of pollution as global phenomenon of pollution;
- possibilities of maintaining a balance between the economic development and pollution.

2. Thermodynamic analysis

The evolution of manufacturing processes, use and generation of pollutants (among which there are wastes, too) is governed by the laws of thermodynamics.

2.1. Analysis using the first principle of thermodynamics

It is recommended that pollution analysis using the first principle of thermodynamics showed to be made by taking into account the considerations below.

- The scheme of the simplest operating system includes the following metallurgical measures (Fig. 1):
  - input measures;
  - output measures, which consist of:
  - useful measures;
  - losses.
- It is proposed that the pollutants (materials and energy transferred to the external environment) should be considered *losses* [1].

- The idea that pollutants are system losses should be reported to the first principle of thermodynamics, that there is no system to function without losses (*zero losses*). In these circumstances, the concept of zero waste plant (launched also in metallurgy), is not justified in terms of thermodynamic. It must be accepted and operationalised as target [2].
- The zero waste status can result only in case of cancellation of the technological process (production stoppage).

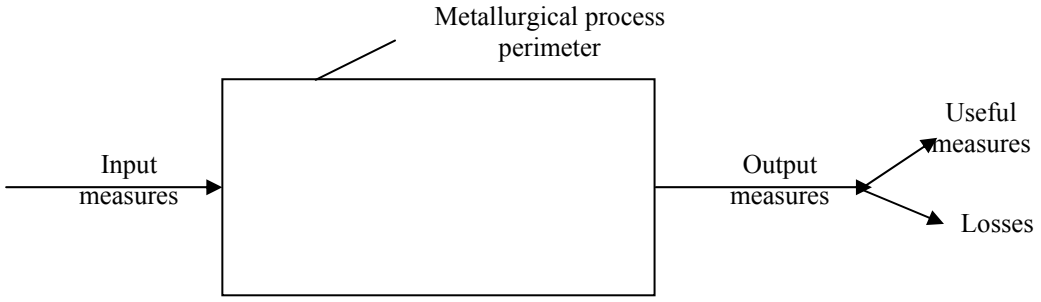

Fig. 1. *Scheme of thermodynamic operation of a technological process.*

- A similar situation concerns the risk analysis. Any industrial activity is associated with risks, reason why the target of environmental policy, of **zero risk** level, is unrealistic, because it can only be achieved by stopping the production [3]. To run the industrial activity, ***we should be aware of the existence of potential risks, to accept the consequences of some of them*** and / or ***to take measures to minimize unacceptable risks.***

2.2. Analysis using the second principle of thermodynamics

In this case, it is an entropic analysis, where two important thermodynamic measures are used:

– *Entropy, S,* which is a measure of the degree of disorder (chaos) in the organization of matter; where the growth of S characterizes the spontaneous tend of the systems to chaos;

– *Negentropy (antientropia), nS,* which characterises the level of the ordered organisation of matter and energy.

For analyses of pollution phenomena using the second principle, we make some recommendations:

- As losses to the environment, *the pollutants represent a state of disorder*. It follows that the generation of pollutants is an anti-entropic phenomenon, inadvisable in terms of the second principle of thermodynamics [1].
- The manufacturing phase (process technology) is an activity to increase the degree of order on the path *natural resources - metal product*. It may be concluded that *advanced processing* of natural resources is recommended in the pollution minimize policies.
- The degree of disorder (entropy S) of pollutants increases with increasing the duration of keeping them in the environment. It is recommended into a flow designed with the reintegration (recirculation, recycling, or regeneration) of wastes *to reduce the number of reintegration*.
- The degree of disorder (entropy S) of wastes increases with increasing the distance between the location of generation and the location of reintegration.

In this situation, it is recommended:

– To decrease the distance between the two locations;

– To use internal reintegration (waste recovery inside the perimeter of the facility that generated them) instead of the external reintegration (recovery of wastes in other locations).

3. Analysis with system theory elements

Analysis of pollution phenomena and pollutants can be also done by using the systems theory. We take into account the aspects presented below.

- *It is proposed* that in the structure of the natural system, the pollution should be considered as *disturbance process*, and the pollutants – *disturbance measures (noises)*, (Fig. 2).
- According to the systems theory, *a certain amount of noise must exist to maintain the order*, because it provides information on system status. It is concluded that *maintaining the life* of the system requires a certain minimal amount of disturbance.

It is argued in this way that ***zero pollution*** *is not only impossible to be reached, but a certain amount of pollution must be kept to a minimum rate*.

- It is proposed that the routes of the secondary materials reintegration should be considered *feedback paths* (Fig. 3).

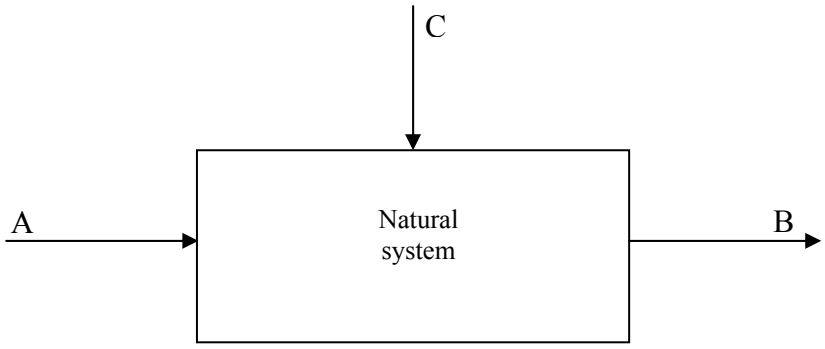

Fig.2. *The simple structure of the natural system.*
A – input measures (control measures; measures to transform the natural ecosystems);
B – output measures (parameters regarding the productive capacity in resources, parameters for rational use of resources, parameters on carrying capacity); C – disturbance measures (pollutants, including wastes).

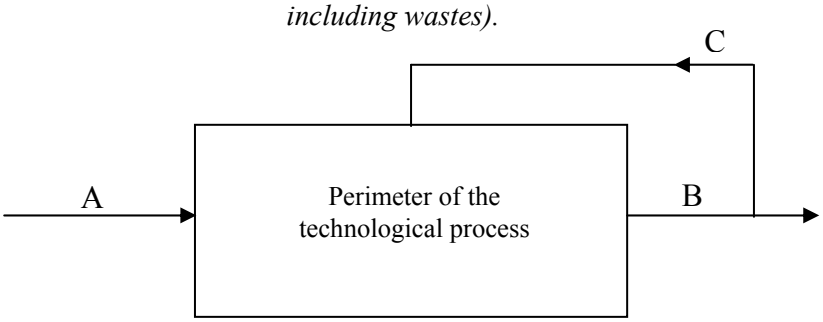

Fig.3. *Diagram of the technological process as a system.*
A – input measures; B – output measures; C – feet-back path of the wastes.

- If the reintegrated secondary materials (wastes) are subject of feed-back, they can perform two functions:
  - Transport of materials (secondary material resources) and energy (secondary energy resources);
  - Information transportation represented by the technological deviations that led to wastes; reintroduced in the primary sequences of the flow, such information becomes levels of the system (self) control.

- The self-adjustment ability of a system, i.e. the capacity of self-sustainability of the natural system in its relations with the economic and social system, depends on the diversity of its behaviour. We deduct from this the *need to diversify* the base of raw materials and energy of metallurgy, on the one hand, and the *metallurgical production*, on the other one.
- The losses to the environment (pollution) must be correlated with another rule of systems theory showing that in a systemic evolution, *the presence of losses stimulates the development*.

4. Characterization of pollution as a global phenomenon of soiling

One of the meanings that can be given to pollution is the soiling. Etymologically, by its Latin origin (poluo-polluere), the term *to pollute* means *to soil*, and *pollution* can be interpreted as soiling. There are many situations (economic, social and environmental) that can be treated as soiling phenomena (quality deterioration). So, it becomes possible a new approach of the phenomena of pollution, by extending the application of the environmental laws in other areas (industrial and even social). In this context, we can say that there are:

– *conventional pollution phenomena* including the known classic cases on the related environmental pollutants → environmental factors → quality of life;

– *unconventional pollution phenomena* relating to the process interaction between environments and special items, of which qualitative alteration can be studied based on principles of ecology.

For the second case, this article refers to two situations: use of metallic implants and the use of metal ornaments. The interactions between them and the substances of human body are considered to be a process of pollution. The process of interaction between human body and the objects mentioned above is in fact a process of soiling them or their bodies.

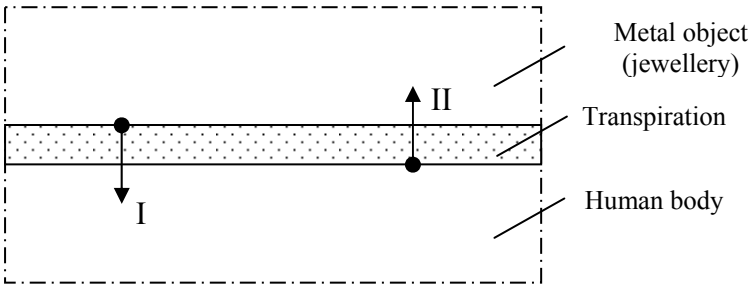

Fig. 4. *Examples of unconventional pollution (soiling): I) direct pollution; II) indirect pollution.*

It can be conclude that it is a process of bi-univocal pollution (Fig. 4):

– *unconventional direct pollution*, which means pollution on the relation *metal object* → *human body* and refers to the negative impact of the object on the body;

unconventional indirect pollution, which means pollution on the relation *human body* → *object* and refers to the negative impact of body on the object, with direct implications on the duration of its social utility.

5. Possibilities of maintaining a balance between the economic development and pollution

Optimizing the correlation between development and pollution is a fundamental issue of knowledge in today's society. It is also known as the *contradiction* between the *human activity* and *environmental conditions*.

The currently recommended measures to mitigate this contradiction are placed in two categories:

– measures of technical and technological nature;

– measures of social-political-administrative nature.

In this article, we analyse a possible situation in metallurgy.

- The target-binding development in metallurgy can be characterized by the production of steel P [tonnes of steel / year]. Under development strategies, it must have an upward trend (Fig. 5, trend 1).

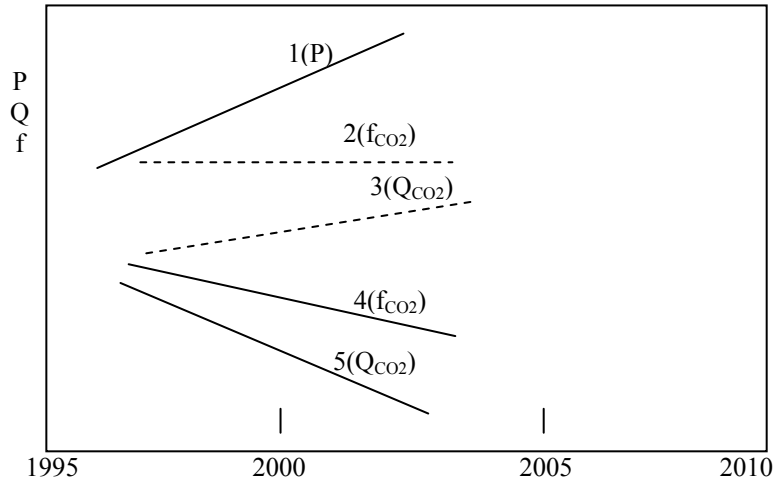

Fig.5. *Dynamics of relationship between development and pollution.*

- Manufacture of steel is accompanied by CO_2 generation. The process is evaluated using the emission factor $f_{CO_2}[t \cdot CO_2 / t \cdot steel]$. Where no action is taken to minimize the CO_2 emissions, the factor f_{CO2} has constant values (Fig. 5, trend 2).
- The CO_2 quantity is Q_{CO2}:

$$Q_{CO_2} = P \cdot f_{CO_2}\ , [t \cdot CO_2 / year]$$

Where no action is taken to minimize the CO_2 emissions, this indicator is trending upward (Fig. 5, trend 3).

- By taking measures to decrease the CO_2 emissions, the factor f_{CO2} is trending downward (Fig. 5, trend 4).
- By reducing f_{CO2}, we can also reduce Q_{CO2} (Fig. 5, trend 5), although P increases.

6. Conclusions

∗ It is proposed that pollutants should be considered *losses* from the technological process perimeter to the environment.

∗ It is proposed that pollutants should be considered disturbances (noises) in the natural system.

∗ The activities and the anti-entropy actions determine the reduction of the pollutants quantities.

∗ To use the environmental laws to analyze the phenomena in different areas, it is recommended for pollution to be considered a soiling process.

∗ To solve the contradiction between development and pollution, it becomes necessary to minimize the emission factors given by the industrial activities.

References

[1]. Nicolae A., et. a. - *Econologie metalurgică*, Ed. Printech, Bucureşti, 2009.
[**2]. Nicolae A., et. a.** - *Management ecometalurgic*, Ed. Fair Parners, Bucureşti, 2001.
[3]. Ursul A., Rusandu I., Capvelea A., (2009), *Dezvoltarea durabilă: abordări metalurgice şi de operaţionalizare*, Ed. Ştiinţifică, Chişinău.
[4]. Vădineanu A. - *Managemtul dezvoltării: o abordare ecosistemică*, Ed. Ars Docendi, Bucureşti, 2004.

THE ANNALS OF "DUNAREA DE JOS" UNIVERSITY OF GALATI.
FASCICLE IX. METALLURGY AND MATERIALS SCIENCE
N^0. 4 – 2011, ISSN 1453 – 083X

RESEARCHES REGARDING WASTE PROCESSING OF CELLULOSIC MATERIALS BY PYROLYSIS PROCESS

Ana DONIGA, Dumitru DIMA, Paula POPA, Elisabeta VASILESCU
"Dunărea de Jos" University of Galaţi
email: ana_doniga@yahoo.com

ABSTRACT

In this paper were performed laboratory experiments regarding processing by pyrolysis process of urban waste components (wood, paper, textiles). The authors designed and developed an experimental equipment and were applied several technological parameters such as temperature and plant maintenance time. The analysis of physical and chemical properties of obtained products found that pyrolysis process can be an effective alternative treatment of urban waste to reduce their quantity and to increase environmental protection.

KEYWORDS: urban waste, physical and chemical properties

1. Introduction

The waste amount at global level is currently increasing. This is due, firstly, to the global population growth and the urbanization increasing process and secondly, to the high rate of industrialization. These contribute to increasing quantity and diversification of solid waste, not only in developed countries but also in developing countries. Waste concentration is much higher in cities than in rural areas, because of the urban population tendency to consume more than the rural one. Therefore, currently, there is more acute the problem of waste reduction, recycling and recovering a part of the waste, or by destruction, using different methods of those who cannot be recovered.[1]

Recycling and recovering of urban waste at global level is aiming, firstly, to an advanced processing (and therefore decrease the amount) and, secondly, to reduce pollution and environmental protection. Products obtained from these processes can be used in other industries.

The largest amount of urban waste is organic (biomass): wood products, plastics, paper, cardboard, textiles, food waste, rubber, leather, etc.. The main substances contained in municipal solid waste are: cellulosic substances, albuminoidal and protein, fat, minerals, etc.

There are different methods of waste processing: biological, mechanical, thermal, etc. Among the most commonly used heating methods are drying, incineration, pyrolysis and co-incineration.

Pyrolysis is a thermal process occurring in the absence of oxygen and consists of successive decomposition of the main constituents (cellulose, lignin, hemicellulose), which have different thermal stability. The process of breaking and rearrangering of the bonds in polymers (constituents) that form the biomass, leading to a large number of products, grouped into three fractions:

- *solid fractions* (coal) is the solid residue formed mostly of carbon;
- *liquid fraction* (bio-oil, tar, steam): a mixture of compounds, volatile pyrolysis temperature, which then condenses at ambient temperature. They are high molecular weight components;
- *gas fraction:* CO, CO_2, H_2, hydrocarbons. They are low molecular weight components. Considering that biomass has as basic component the cellulose, we state that the pyrolysis (thermal decomposition) is governed by the following scheme (Figure 1) [2].

In terms of energy, pyrolysis reactions are endothermic and have multiple effects:

- removal and transformation (neutralization) of waste and other waste type, take into account the environmental conditions;
- reducing of treated waste in volume and weight;
- obtaining liquid and gaseous fuels.

The composition and quality of products obtained from pyrolysis depend on the processed waste quality, but also on the equipment operating and service conditions. With appropriate equipments, some products can be separated and recovered completely as fuel or raw material for chemical industry.

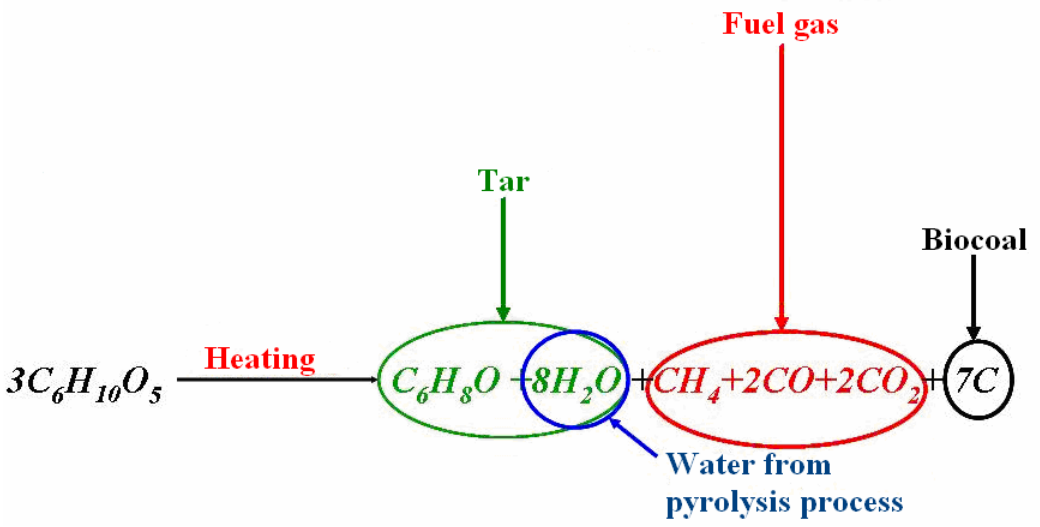

Fig. 1. *Cellulose pyrolysis.*

Pyrolysis can be applied in several ways, depending on working conditions: [3]

- low temperature pyrolysis (400 ... 600 ° C) and medium temperature (600 ... 1000 ° C);
- high temperature pyrolysis (2000 ° C);
- pyrolysis in molten metal bath salts or;
- vacuum pyrolysis.

2. Materials used and experimental procedure

To achieve the laboratory experiments, were used household waste as wood flour, paper packaging (cardboard) and yarns [4]. All these materials have approximately the same composition:

- Cellulose ($C_6H_{10}O_5$) x, proportion of 40 ... 50%;
- Similar hemicellulose xylan ($C_5H_8O_4$) m, proportion of 15 ... 25%;
- Lignin [C_9 H_{10} .3 (OCH 3) 0.9 to 1.7] n about. 20 ... 30% (characteristic for wood – it is found in bole, leafage and bark)
- Organic substances: polysaccharide, pentozans, hexozans, resins, tannins, dyes, waxes, alkaloids.

To carrying out the pyrolysis process in optimal conditions, fine particles materials are necessary. It has been selected wood flour and cardboard was cut into very fine strips, while for textile were chosen cotton waste.

The experiments were conducted in the University "Dunarea de Jos" of Galati, Faculty of Metallurgy, Materials Science and Environment and Faculty of Chemistry laboratories.

It has been established a technology to carry out the pyrolysis process, based on the following steps (Fig. 2).

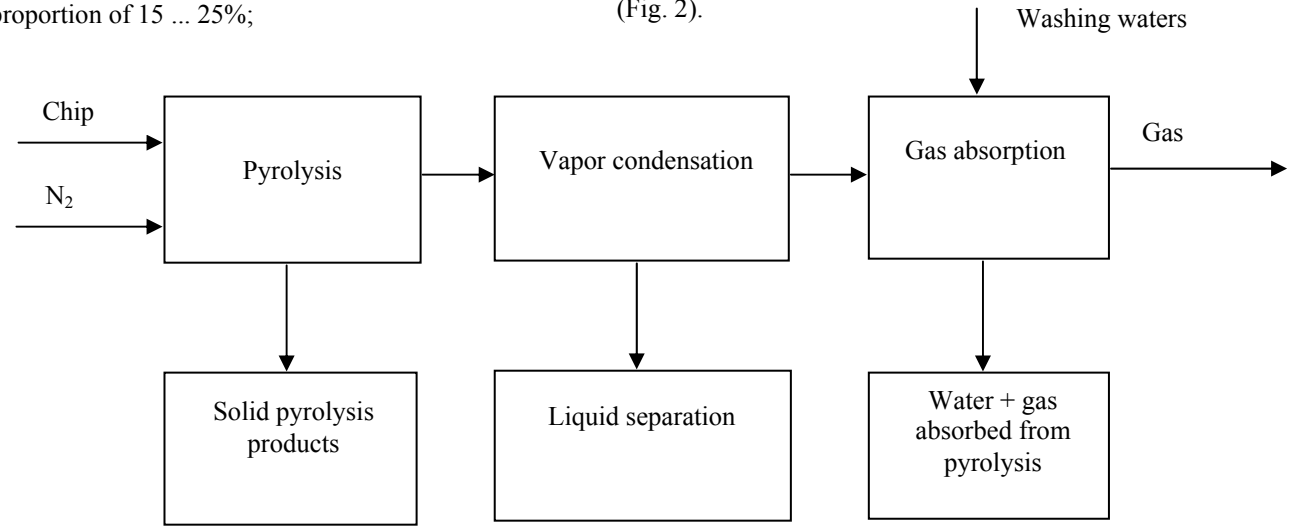

Fig.2. *Pyrolysis process technology diagram for wood waste.*

It was designed an equipment consisting of an Automatica electric furnace with silit bar heaters in which an air-tight enclosure with protective atmosphere was entered.

For a complete removal of resulting gas, it was introduced nitrogen, circulating throughout the deployment process at a pressure of $1.2x10^5$ Pa.

For gas capture, two vessels for washing plastic (PET) were used and introduced in distilled water and were connected to the pyrolysis chamber. Resulting gas were dissolved in water and the liquid can be analyzed. The third plastic container was left empty, to capture the last amount of gas insoluble in water (Fig.3).

Fig.3. *Pyrolysis equipment.*

Pyrolysis process was carried out according to the following steps:

- *sample preparation*. Waste samples were dried in the oven, placed in two metal tanks and were weighed on an electronic balance, then placed inside the enclosure work.

- *pyrolysis process.* We have chosen several temperatures: 600^0C, 400^0C, 300^0C, 200^0C. Maintenance times: 4 hours, 1 hour, ½ hours. Nitrogen continuously circulated through the equipment.

- *process ending.* The equipment stops by furnace cooling after the established time and nitrogen flows through to fully capture any resulting gas;

- *sampling and laboratory analysis.*

Final, pyrolysis products are presented as three fractions:

- solid fractions of small particles (wires) of coal with original waste size and shape (Fig. 4);
- liquid fraction, collected in a silicone rubber coil, connected to the first gas capture container;
- gas fraction, dissolved in distilled water containers. We used this method to determine the physical properties of resulted gases.

Fig. 4. *Solid fraction resulting from pyrolysis process:*
a – from wood flour, b – from paper.

3. Experimental results

In the process of pyrolysis were analyzed the resulting three fractions as follows: *Solid fraction.* The obtained coal sample was weighed and compared to initial sample in terms of mass, after its chemical composition was analyzed.

In Tables 1, 2, 3 are presented the main parameters of the process and mass samples, initial and final mass loss after thermal processing.

Applied thermal regime and mass loss of analyzed samples

Table 1. Wood Flour

Sample	Thermal regime		Solid mass fraction (g)		Weight loss (ΔG)	
	Temperature (^{0}C)	Time (hours)	initial G_0	final G_1	(g)	%
B_1	600	4	20	5.30	14.70	73.5
B_2	600	1	20	6.40	13.60	68.0
B_3	400	1	20	6.59	13.41	67.07
B_4	300	1	20	8.10	11.90	59.5
B_5	200	1/2	20	8.70	11.30	56.5

Table 2. Paper waste

Sample	Regime		Solid mass fraction (g)		Weight loss (ΔG)	
	Temperature (^{0}C)	Time (hours)	initial G_0	final G_1	(g)	(%)
H_1	300	1	20	6.90	13.10	65.50
H_2	300	1/2	20	7.49	12.51	62.55
H_3	200	1	20	9.23	10.77	53.85
H_4	200	1/2	20	11.17	8.83	44.15

Table 3. Textile waste

Sample	Thermal regime		Solid mass fraction(g)		Weight loss (ΔG)	
	Temperature (^{0}C)	Time (hours)	initial G_0	final G_1	(g)	%
T_1	600	1	20	3.95	16.05	80.25
T_2	400	1	20	7.49	12.51	62.55
T_3	300	1	20	9.07	10.93	54.65

ΔG mass loss is determined by the relationship: $\Delta G = G_0 - G_1$

The diagrams in Figure 5 show the variation of mass loss depending on process parameters and sample's material.

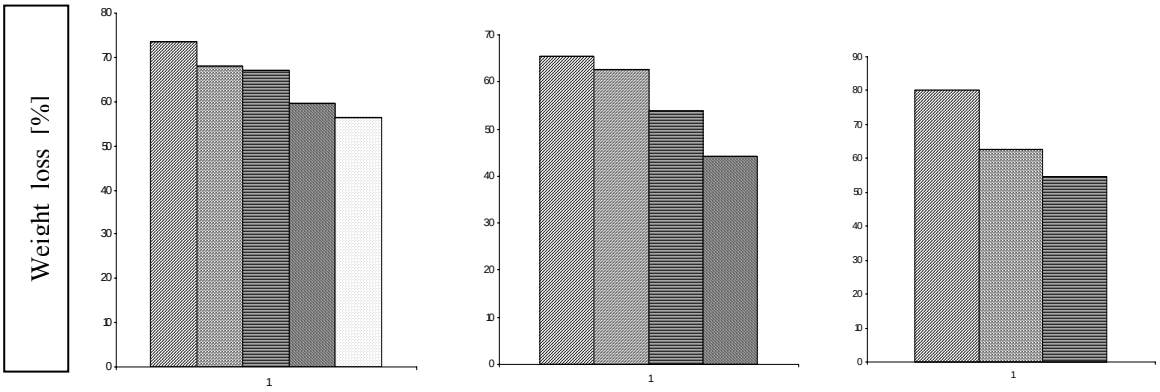

Fig.5. *Mass loss resulting from pyrolysis: a) wood flour, b) board, c) textile.*

Mass loss increases with increasing temperature and working time, also is quite important even at low temperatures (200 ... 300^{0}C). On an LECO equipment was analyzed the result coal of pyrolysis of wood and cardboard waste. The carbon percentage shows the process efficiency and solid fraction recovery possibilities (Table 4). Carbon content is high, so the thermal decomposition is advanced even at low temperatures.

For identification of other elements present in the solid fraction was used XRF spectrometer. The results are presented in Table 5.

Table 4. *Carbon and sulphur content of analyzed samples*

Material	**Sample**	**Thermal regime**		Carbon (%)	**Sulphur** (%)
		Temperature (^{0}C)	**Time** (hours)		
Wood flour	B_4	300	1	73.24	0.30
Wood flour	B_5	200	1/2	71.90	0.32
Wood flour	B_6^*	300	1	70.95	0.34
Cardboard	H_1	300	1	57.33	0.18
Cardboard	H_2	300	1/2	56.89	0.17
Cardboard	H_3	200	1	53.44	0.18

$^*B_6$ sample was obtained by pyrolysis of wood waste in the absence of nitrogen.

Table 5. *The content of the main elements present in pyrolysis material*

Sample	**Zn**	**Fe**	**Mn**	**Cr**	**Ca**	**K**
H_1 (Cardboard)	31.61	353.93	41.91	386.01	15728.2	28552.15
B_4 (Wood flour)	26.29	321.09	39.62	335.07	15310.34	27698.71
T_3 (Textile)	442.91	362.89	-	396.46	12162.84	3033.41

The analyzed samples were subjected to the same working regime (temp = 300^0 C, time = 1 hour). Liquid fraction resulted is a strong smelling tar, dark brown color and consistency of oil. Because small amount were obtained, could not achieve a complete material analysis. The resulting gas from pyrolysis was dissolved in distilled water to determine the physicochemical properties of the resulting liquid, using a multifunctional analyzer with Consort C862. For each sample were determined pH, electrical potential (V), conductivity (λ), resistivity (ρ) and total dissolved salts (TDS).

The results are presented in Table 6.

Table 6. *Physical properties of dissolved gases*

Parameter	**Measurement units**	**Sample code**		
		Wood flour (B_4)	**Cardboard** (H_1)	**Textile** (T_3)
pH	upH	3.74	4.44	3.67
V	eV	164	116	185
λ	μS/cm	62.5	24.9	141
ρ	kΩ·cm^{-1}	15.99	47.5	7.09
TDS	mg/L	37.1	11.2	83.6

All liquid samples analyzed have low acidic pH. The sample's acidity is given by the content of organic acids and carbon dioxide, retained as a result of distilled water barbotage of the gas resulting from the pyrolysis process.

Liquid samples have variable conductivity, the highest values occurring in those from the textile waste. The total content of dissolved salts recorded higher values throughout the textile waste.

Gas fraction. For gas analysis was conducted a wood waste pyrolysis at a temperature of 300^0 C for one hour.

Gases were captured in two plastic containers, without using distilled water. It was used a combustion gas analyzer MSI type. The results are shown in Table 7.

The pyrolysis conditions applied resulted in a high content of NO and CO.

Table 7. *Gas fraction composition of wood waste pyrolysis*

Container	O_2 (% vol)	SO_2 (ppm)	NO (ppm)	CO (ppm)	CO_2 (% vol)
1	10.8	281	509.5	853.6	9.8
2	19.4	35	412.3	543.8	1.5

4. Conclusions

The experimental research led to the following observations:

- the organic decomposition by pyrolysis process was carried out in a simple equipment with low energy consumption;
- the low temperature and time process;
- the small amount of solid fractions after pyrol.ime and working conditions;
- the resulted coal is called "biological coal" and it has a high mineral content, useful as fertilizer in agriculture;
- the captured gases contain a high percentage of NO and CO. In an industrial gas plant, the resulted gas can be used as fuel in the pyrolysis process, thereby eliminating carbon monoxide;
- the possibility of energy recovery products;
- the possibility of a wide variety of organic waste;
- low environmental impact.

From observations during experimental research it can be concluded that in an urban area, depending on waste storage and processing possibilities, pyrolysis may be preferred to other waste treatment processes due to the advantages it presents:

- waste consumption;
- use of charcoal as a solid material for wastewater treatment, including those resulting from the pyrolysis.

References

[1]. Ndiaye F. T. - *Pyrolyse de la biomasse en reacteur cyclone-recherche des conditions optimales de fonctionnement,* I.N.P. Lorraine, 2008.
[2]. Ion V.Ion - *Energia biomasei* – Energie nr.7 (38), 2006, p. 14-30.
[3]. G.I.E. PROCEDIS - *Pyrolyse – gazéification de dechets solides,* Etude ADEME/ Procedis -2004.
[4]. G. Finqueneisel – *Les mécanismes primaires de pyrolyse de la biomasse,* Université de Metz – 2009.

THE ANNALS OF "DUNAREA DE JOS" UNIVERSITY OF GALATI.
FASCICLE IX. METALLURGY AND MATERIALS SCIENCE
N^0. 4 – 2011, ISSN 1453 – 083X

SOME EFFECTS OF MICROWAVE HEATING OF CHROMITE ORE FOR Fe-Cr-Al ALLOYS BY ALUMINOTHERMY

Petre Stelian NITA
Faculty of Metallurgy, Materials Science and Environment,
"Dunarea de Jos" University of Galati
email: pnita@ugal.ro

ABSTRACT

Processes and prime materials involved in Fe-Cr-Al alloys production by aluminothermy are presented having in view new possibilities to produce them more ecological and more efficient, using energy of microwave field.

The capacity of heating pieces of chromite ore containing 56.52 %mass Cr_2O_3 and a ratio (% massCr_2O_3/ %massFeO)=2.622 in a domestic microwave oven is evaluated at the maximal power of the microwave field of 700W where a maximal temperature about 260^{0}C was obtained after 16minutes heating. A rapid cooling from this temperature to 20^{0}C, by water immersion induces an increasing of the internal voids due to new cracks and the development of pre-existing cracks of about 0.15-0.29 %, which helps to reduce the energy consumption in chromite comminution. The final heating temperatures show a low possible contribution to the reduction of energy consumptions in direct metallurgical processes on the account of chromite ore heating in microwave field.

KEYWORDS: chromite ore, microwave heating, internal voids, cracks

1. General aspects

Classical metallothermy is based on the thermal energy released by exothermic reactions of different oxides mainly that or those of the metal recuperated in ferroalloy, which spontaneously proceed after the ignition of an exothermic mixture. Igniting mixtures presents characteristics of a low ignition temperature and a high thermal effect. Around the ignition place a zone of important heat emission develops and the thermal energy contribution makes possible the development of the main metallothermic reactions related to the ferroalloy which is the object of this activity.

The main reaction could be generically written in the following form:

$$MeO + R \rightarrow Me + RO \quad (1)$$

The condition for such reaction to take place in the direct sense, at a temperature T, is:

$$\Delta G^0_T < 0 ,$$

where:

$\Delta G^0_T = \Delta H^0_{298} - T\Delta S^0_{298}$ is the standard variation of the free enthalpy.

According to basic papers [1][2], certain class of materials are necessary to compose an exothermic mixture of materials to obtain ferrochromium without carbon content, through the aluminothermic process. The sources of chromium are usually chromium concentrates containing 60% Cr_2O_3 and cca. 14% mass FeO. Chromite ore contain mainly the spinel of chromium $FeO \cdot Cr_2O_3$ and other oxides as magnesia (MgO), substituting for FeO and alumina (Al_2O_3) or the ferric oxide (Fe_2O_3), substituting for Cr_2O_3 are the main mineral materials used to obtain these concentrates. According to possibilities or requirements in the mixture are used partially materials bringing oxide as CrO_3 or oxy-salts $K_2Cr_2O_7$, instead of Cr_2O from chromite ore. Handling and storing by-products must be extremely controlled in the case of chromium trioxide CrO_3, due to carcinogenic potential of the Cr^{6+}. Chromates, dichromates, chlorates, perchlorates, nitrates, calcium permanganate, silicon permanganate, sodium permanganate are used as oxidizing materials. Aluminium, silicon, calcium, sometimes manganates are used as reducers. CaO as lime and CaF_2 as fluorine are used as fluxing agents. Mixtures, as barium peroxide and aluminium powder or sodium nitrate and magnesium powder, are used as igniting agents. In order to give a certain solid consistency to the column of granular and powder materials, cement, sodium silicate as aqueous solution or certain organic materials are used as binder.

2. Thermodynamic aspects of aluminothermy in obtaining chromium metal and alloys

Reduction of various oxides of chromium and other compounds containing chromium using aluminium as reducer are presented as chemical reactions in the Table 1.

The reasons of introducing of an oxidizing material, as mentioned before, consist in the energetic needs to ensure the progress of the reduction of the main chromium source. According to the data presented in the table 1., both two possible reactions of reducing Cr from Cr_2O_3 using aluminium as reducer are not enough exothermic to fulfill the necessary thermal energy.

In the case of metallic chromium and ferrochromium without carbon using the aluminothermy process, the main reduction reactions of chromium oxides with aluminium are not enough exothermic, compared to necessities. In the Table1 these effects are presented.

The bolded reactions are those making the object of aluminothermy.

The main problem of metallothermy, in general, is to ensure the necessities of thermal energy required in each volume where there are accomplished all the other conditions for reduction of oxides source of required metal in the ferroalloy.

According to ref. [2], the necessary unitary thermal effect which must develop to ensure the reduction reaction could be evaluated using the relation:

$$\Delta H = \frac{\Delta H^0_{298}}{M_{MeO} + M_R}, \quad \text{kJ/kg}$$

where:

M_{MeO} - is the molar mass of the oxide of the metal to be recuperated in the ferroalloy;

M_R- is the molar mass of the metal used as a reducer.

The required value of the necessary released heat must be: ΔH>2300kJ/ kg charge

According to the ref.[3] the required unitary thermal effect must be: ΔH>2700kJ/ kg charge. In these conditions it was evaluated that a metallothermic process runs spontaneously, that means it is self–sustaining and ensures an adequate separation of metal product and slag, if the following condition is accomplished [3]:

ΔH^0_{298}< -302kJ/gr.at Al According to the table 1[1-4] reduction reactions of chromium oxides with aluminum do not satisfy this conditions, also reduction of silicium dioxide with aluminium and reactions (2)(7)(8) are carcinogenic. Reduction of Fe_3O_4 with aluminium satisfies the required condition and the heat released is in an evident excess, compared to the condition. This physical evidence is not enough investigated and valorized, despite its high economical and ecological potential. In aluminothermy process applied to obtain chromium metal or alloys without carbon or silicon content, also in other metallothermic processes, other reactions mainly exothermic could be produced and also they have harmful effects being toxic, carcinogenic or present risks of strong inflammability and explosion.

Table 1. *Values of ΔH^0_{298}, [kJ/ mol Al] of different reactions possible to take place in metallothermic production of chromium alloys based on chromite, and of different associated reactions*

Crt no.	Reduction reaction	Variation standard enthalpy ΔH^0_{298}	Observations on reaction and on main reactant; [1]-[4]
1	$1/2Cr_2O_3+Al \rightarrow Cr+1/2Al_2O_3$	-272.2	deficit of heat
2	$1/2CrO_3+Al \rightarrow 1/2Cr+1/2Al_2O_3$	-547.2	Carcinogenic, deliquescent
3	$Cr_2O_3+2Al+CaO \rightarrow 2Cr+CaO\cdot Al_2O_3$	-275.8	deficit of heat
4	$Cr_2FeO4+8/3Al \rightarrow 2Cr+Fe+4/3Al_2O_3$	-290.6	deficit of heat
5	$Cr_2FeO4+8/3Al+4/3CaO \rightarrow 2Cr+Fe+ +4/3CaO\cdot Al_2O_3$	-298,6	deficit of heat
6	$CrO_3+2Al+CaO \rightarrow Cr+CaO\cdot Al_2O_3$	-550.8	Carcinogenic, deliquescent
7	$K_2Cr_2O_7+4Al \rightarrow 2Cr+2\ Al_2O_3+K_2O\uparrow$	-429.7	Carcinogenic
8	$Na_2Cr_2O_7+4Al \rightarrow 2Cr+2\ Al_2O_3+Na_2O\uparrow$	-449.3	Carcinogenic, hygroscopic
9	$3/8Fe_3O_4+Al \rightarrow 9/8Fe+1/2\ Al_2O_3$	-418.3	-
10	$3/4SiO_2+ Al \rightarrow 3/4Si+1/2\ Al_2O_3$	-158.7	deficit of heat

↑- the compound vaporizes or it is a gas at reaction temperature.

3. Experimental trials

3.1. Composition of chromite ore

A piece of chromite ore obtained by cracking, taken into account in this research was analyzed visually.

On the surfaces of the chromite ore piece enough important zones contain thick filaments of silicates grown intimately with chromite. The chemical composition presented in the tab.2, was obtained on granular samples obtained by crushing using an X-rays spectroscopic device.

The result of the analysis of the average sample, obtained by quartation method, is not identical with the arithmetic average of the initial five samples, but enough close to this.

Table.2. *Chromite ore composition*

Crt. No.	Oxides, %mass						Cr_2O_3 /FeO
	Cr_2O_3	FeO	SiO_2	Al_2O_3	MnO	NiO	
1	59.231	19.2	18.97	2.097	0.605	0.693	3.098
2	55.74	20.884	22.267	-	-	1.108	2.669
3	57.281	23.796	16.816	-	0.721	1.386	2.407
4	52.24	20.69	25.71	-	-	1.36	2.525
5	55.48	21.852	21.0	-	-	1.668	2.539
6	59.332	23.157	16.177	-	0.30	1.034	2.562
*	56.52	21.56	20.21	0.23	0.27	1.121	2.622

* Average sample obtained by quartation method.

3.2. Heating of chromite ore in microwave field

Experiments have been performed in the laboratory "Alternative and Non- conventional Processes in Metallurgy" of the Faculty of Metallurgy, Materials Science and Environment of the "Dunarea de Jos "University of Galati.

Four samples of chromite ore of initial mass in the range 73.7-170.9 g measured after the exposure in free air at 20^{0}C for 24 hour, have been submitted to heating in a domestic microwave oven generating a microwave power of 700W.

Chromite samples have been placed inside of a central cavity (height H=80mm, inner diameter I.D=115mm) made in a refractory bond and covered by ceramic refractory wool (1250^{0}C) of 25mm thickness.

A K-thermocouple (1200^{0}C) places in a refractory shell with diameter D=3mm, length L=145mm, coupled to a measuring device Digitron 2751-K was placed centrally through a hole drilled in the roof of the microwave oven, inside of this as closed as possible to the chromite sample. The evolution of temperature is shown in fig. 1

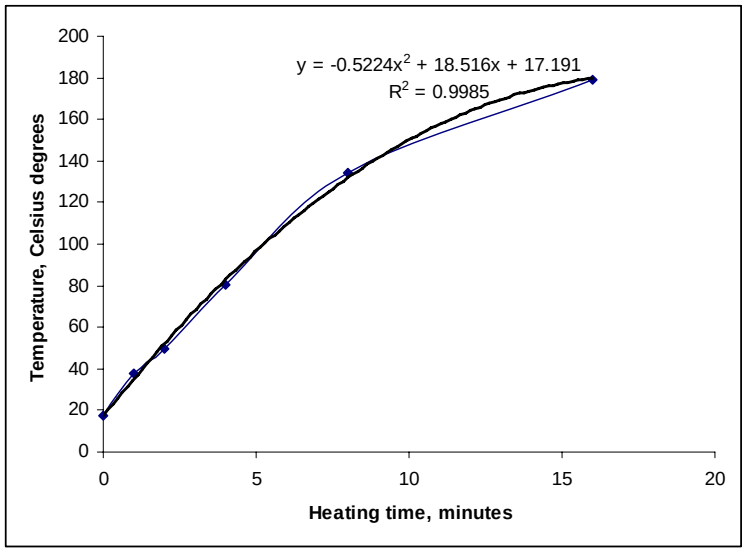

Fig.1*. Evolution of temperature (contact) on the heating time in microwave oven at maximal power 700 W of chromite ore samples no1 and 2 together. Temperature measured after heating pause cycle 1min./pause/1min./pause/2min/pause/4min./pause/8min./final. Total heating time: 16 minutes.*

The registered temperatures upon the heating time (excepting pauses) are presented in the figure 1. The samples at their final temperatures have been cooled in water (20^{0}C) by rapid immersion and weighted mainly in order to evaluate the contribution of the rapid heating and cooling to the cracks development. They have been weighted again after an exposure of 16 hours in a free air at 20^{0}C The distance between the thermocouple and the sample influence much the displayed value of the temperature because of the inertia in heating transmission by different mechanisms, mainly by convection and radiation, but which is desired to take place by direct contact, from sample to the shell of thermocouple and further, inside of this through the thin refractory protection layer, to the junction point chromel–alumel. These aspects could lead to differences of instant temperature of several tenths of degrees, not enough evaluated in the present experimental trials. Therefore, only in the case of the first two samples of chromite, a heating curve could be established, without to take into account the pauses durations, separated or summated.

The maximal performance of heating is better represented by the samples no.3 and no.4. The experimental results in table 2 after 16 minutes at 100% power show a temperature about 259^{0}C by heating of chromite samples in microwave oven and an induced porosity and cracks of samples by cooling in water, of 0.15% (sample no.3) and 0.29% (sample no.4). The total volume of internal voids, concentrated or as active cracks, by the treatment consisting in microwave heating and freezing by immersion in water seems to double, compared to the initial state. These results show the necessity to determine better on more systematic bases the tendency to cracking by heating in microwave oven, followed or not by cooling, commonly in water.

Table 3. *Results of microwave heating applied to samples of chromite ore*

Sample No.	**Mass,** [g]				**Temp.**[^{0}C], **after heating 16 minutes in microwave oven at 100% power**
	Initial	**After heating**	**After cooling in Water [20^{0}C] for 25 minutes and 25 minutes drying at 20^{0}C**	**After 16 hours at 20^{0}C**	
1*	-	73.7	75.2	74.7	179.3**
2*	-	120.6	123.6	122.3	179.3**
3	130.2	129.3	131.9	130.4	259
4	170.9	169.6	172.4	171.4	255

* samples no.1 and 2 have been heated together.
** temperature according to the explanations in the Figure1.

4. Commentaries and conclusions

Thermodynamic data on the specific reactions show an important potential to use iron ores as an oxidizing material and iron source in the final alloys especially when technical alloys Fe-Cr-Al are produced. This could be better exploited by applying a preliminary heating of the oxides mixtures before processing by aluminothermy. Direct heating using microwave field energy is full of benefits because of its fastness and direct mass heating effects resulting from the energy transfer particularities offered by this energetic field. Eventual limitations in extending this process, due to the limitations of power of magnetrons, used to generate microwave field, are not prohibitive in industrial practice, when introduction of preliminary heated amounts of reactants in the aluminothermic process could be done gradually but relative continously in a certain time period, until the whole programmed amount is consumed. In case of a bigger industrial aluminothermic facility several lines for microwave heating working simultaneously at a maximal capacity could use for heating reactant mixtures. In this way, the general classical problem of metallurgical plant consisting in an extremely limited flexibility around initial designed capacity is largely avoided in the case of using heating energy by microwave field for aluminotherhic production of chromium alloys without carbon, not only for alloying steels but also including those containing high contents of iron as basic materials for technical Fe-Cr-Al alloys.

It is expected that heating in microwave even at important rates of temperature increasing due to the particularities of microwave energy transfer from the generated field and the samples of chromite, taken separated or coupled with a relative high cooling rate by immersion in water, induces inner mechanical tensions of dilatation and compression, which locally could exceed the internal mechanical resistance and

further lead to new cracks and to the development in length and/or width of the already existent cracks. In this way the implementation of the microwave heating technology could be useful in decreasing of energy consumptions during different comminution operations applied to chromite ore.

References

[1]. Durrer, R., Folkert - G. *Metallurgia ferrosplavov*, Metallurgia, Moskva, 1976.
[2]. Liakisev, N.P. s.a. - *Aliuminotermia*, Metallurgia, Moskva, 1978.
[3]. Volkert, G., Frank, K.D.(eds.) - *The metallurgy of ferroalloys,* 2nd edition, berlin , Springer, 1972.
[4]. Vacu, S., Berceanu, E., Nita, P.S., Nicolae, M. - *Metalurgia feroaliajelor"*Ed. Did. si Ped, Bucuresti,1980.
[5]. Derin, B., Erçayhan, S., Yücel, O. - *Effects of charge components on reduction of chromites concentrates by aluminothermic process,* Tenth International Ferroalloys Congress,1-4 February 2004 Cape Town South Africa, Marshal Town South Africa, Proceedings The South African Institute Of Mining and Metallurgy, p.78-82.
[6]. Behera, R.C., Mohanty, U.K. - *ISIJ Intl*, vol41(2001), no.8,827-833.
[7]. Behera, R.C., Mohanty, U.K. - *ISIJ Intl*, vol41(2001), no.8,834-843.

THE ANNALS OF "DUNAREA DE JOS" UNIVERSITY OF GALATI.
FASCICLE IX. METALLURGY AND MATERIALS SCIENCE
N^0. 4 – 2011, ISSN 1453 – 083X

A TRIBOLOGICAL MODEL FOR CONTINUOUS CASTING EQUIPMENT OF THE STEEL

Viorel MUNTEANU[1], Constantin BENDREA[2]
[1]Faculty of Metallurgy and Materials Science, Dunarea de Jos University of Galati
[2]Faculty of Science, Department of Mathematics, Dunarea de Jos University of Galati
email: munteanu_viorel48@yahoo.com

ABSTRACT

This paper presents a coupled thermo-elastic contact problem with tribological processes on the contact interface (friction, wear or damage). The unilateral contact between the cilindrical roll system and a deformable foundation (slab, bloom, etc) is modeled by the Kuhn-Tucker (normal compliance) conditions, involving damage and/or wear effect of contact surfaces. The continuum tribological model is based on gradient theory of the damage variable for studying crack initiation in fretting fatigue [11], [14], [15] , and the wear is described by Archard' s law. The friction law that we consider is a regularization of the Coulomb law.

The weak formulation of the quasistatic boundary value problem is described by using the variational principle of virtual power, the principles of thermodynamics and variational inequalities theory. Thus, the main results of existence for weak solution are established using a discretization method (FEM) and a fixed-point strategy [5].

KEYWORDS: Continuous casting, Thermoelastic contact, Friction, Wear, Fretting fatigue, Variational Inequalities, Galerkin Discretization Method

The elastic thermo-deformable body (walls of the mould, cilindrical rolls system) occupies a regular domain $\Omega \subset \mathbb{R}^d$ $(d = 2,3)$ with surface Γ that is portioned into three disjoint measurable part $\Gamma = \Gamma_u \cup \Gamma_\sigma \cup \Gamma_c$ such that means $(\Gamma_u) > 0$. Let $[0,T]$ be the time interval of interest with $T > 0$. The body is clamped on $(0,T) \times \Gamma_u$ and therefore the displacement field vanishes there. We denote by S_d the spaces of second order symmetric tensors, while "$\cdot$" and $|\cdot|$ will represent the inner product and the Euclidean norm on S_d or $\mathbb{R}^d$. Let n denote the unit outer normal on Γ, and everywhere in the sequel the index i,j run from 1 to d (summation over repeated indices is implied and the index that follows a comma represents the partial derivative with respect to the corresponding component of the independent variable).

We also use the following notation and physical nomenclatures:

$\Omega_T = (0,T) \times \Omega$;
$\overline{\Omega}_T = [0,T] \times (\Omega \cup \Gamma)$;
$\Gamma = \partial\Omega$; $\Gamma_T = (0,T) \times \Gamma$;
$\Gamma_{i_T} = (0,T) \times \Gamma_i$, $i \in \{u ; \sigma ; c\}$;

$t \in [0,T]$ time variable;
$x \in \Omega$ spatial variable;
u : $\overline{\Omega}_T \to \mathbb{R}$d displacement vectorial field;
$\dot{u} = \left(\frac{\partial u_i}{\partial t}\right)$; $\ddot{u} = \left(\frac{\partial^2 u_i}{\partial t^2}\right)$ velocity and inertial vectorial fields, respectively;
$\sigma : \overline{\Omega}_T \to S_d$ stress tensor field (second order Piola –Kirchhoff);
$\varepsilon(u) = \frac{1}{2}(\nabla u + \nabla u^T)$ strain tensor field (linearized tensor Green-St. Venant);
$\theta : \overline{\Omega}_T \to \mathbb{R}$ temperature scalar field;

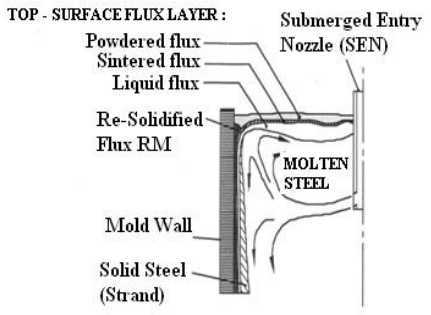

Fig. 1a. *Schematic unilateral contact with pure sliping between the walls of mold and molten steel [5], [12], [14].*

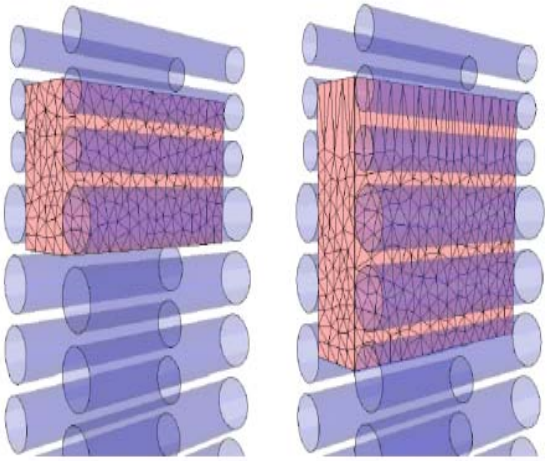

Fig. 1b. *Schematic unilateral contact with pure rolling between the support-rolls and steel slab [5], [12].*

We assume that a quasistatic process is valid and the constitutive relationship of an elastic-viscoplastic material can be written as

$$\sigma = \mathcal{A}\varepsilon(\dot{u}) + \mathcal{G}\varepsilon(u) - \mathcal{C}\theta \qquad (1.1)$$

where $\mathcal{A}$ and $\mathcal{G}$ are *nonlinear* operators whitch will be described below,
and $\mathcal{C} = (c_{ij})$ represents the *thermal expansion tensor*.

Here and below, in order to simplify the notation, we usually do not indicate explicitly the dependence of the functions on the variables $x \in \Omega$ (on the time $t \in [0,T]$ sometimes). Examples of constitutive laws of the form (2.1) can be constructed by using *thermal* aspects and *rheological* arguments, (see e.g. [3], [5], [6], [10], [11]) .

When $\mathcal{C} = \mathcal{O}_{\mathcal{A}}$ the constitutive law (1.1) reduces to the *Kelvin-Voigt viscoelastic* behaviour of the materials ,

$$\sigma = \mathcal{A}\varepsilon(\dot{u}) + \mathcal{G}\varepsilon(u), \qquad in\ \Omega_T \qquad (1.2)$$

Finally, the evolution of the temperature field is governed by the *heat transfer equation* (see [1], [3], [6]),

$$\dot{\theta} - div(K\nabla\theta) = q - \mathcal{C}\cdot\nabla\dot{u}, \ \text{in}\ \Omega_T \qquad (1.3)$$

where : $K = (k_{ij})_{i,j=\overline{1,d}}$
is thermal conductivity tensor;

$$\mathcal{C} = (c_{ij})_{i,j=\overline{1,d}}$$

is thermal expansion tensor;

q represent the density of volume heat sources.

In order to simplify the description of the problem, a *homogeneous condition* for the temperature field is considered on $\Gamma_u \cup \Gamma_\sigma$,

$$\theta = \theta_r, \quad \text{on} \quad \Gamma_{u1T} \cup \Gamma_{\sigma 1T} \qquad (1.4)$$

It is straightforward to extend the results shown in this paper to more general cases.

Also, we assume the associated *temperature boundary condition* is described on Γ_c ,

$$(K\nabla\theta)\cdot n = -k_e(\theta - \theta_r), \ \text{on}\ \Gamma_{c1T} \qquad (1.5)$$

where θ_r is the reference temperature of the obstacle, and k_e is the heat exchange coefficient between the body and the rigid foundation.

Thus, the *thermo-mechanical problem* in the *clasic vectorial formulation*, can be written as follows :
Problem (P):

Find a displacement field u : $\overline{\Omega}_T \to \mathbb{R}d$
a stress tensor field $\sigma : \overline{\Omega}_T \to \mathcal{S}_d$ and,
a temperature field $\theta : \overline{\Omega}_T \to \mathbb{R}$ such that,

$$\sigma = \mathcal{A}(\varepsilon(\dot{u})) + \mathcal{G}(\varepsilon(u)) - \mathcal{C}\cdot\theta \qquad (1.6)$$

$$-div\,\sigma(\varepsilon(u)) = f, \qquad in\ \Omega_T \qquad (1.7)$$

$$\dot{\theta} - div\,(K\nabla_x\theta) = q - \mathcal{C}\cdot\nabla_x\dot{u} \qquad (1.8)$$

$$u = 0, \qquad on\ \Gamma_{u1T} \qquad (1.9)$$

$$\sigma(\varepsilon(u))\cdot n = g, \qquad on\ \Gamma_{\sigma 1T} \qquad (1.10)$$

$$u_n \le 0, \sigma_n \le 0 \ \text{a.i.} \quad u_n\cdot\sigma_n(u) = 0, \quad on\ \Gamma_{c1T} \qquad (1.11)$$

$$|\sigma_\tau(u)| \le \mu|\mathcal{F}\sigma_n(u)|, \quad on\ \Gamma_{c1T}\ \ i.e. \qquad (1.12)$$

$$|\sigma_\tau(u)| < \mu|\mathcal{F}\sigma_n(u)| \Rightarrow \dot{u}_\tau = 0 \qquad (1.13)$$

$$|\sigma_\tau(u)| = \mu|\mathcal{F}\sigma_n(u)| \Rightarrow (\exists)\lambda \ge 0 : \sigma_\tau(u) = -\lambda\dot{u}_\tau \qquad (1.14)$$

$$(K\nabla_x\theta)\cdot n = -k_e(\theta - \theta_r), \quad on\ \Gamma_{c1T} \qquad (1.15)$$

$$\theta = \theta_r, \qquad on\ \Gamma_{u1T} \cup \Gamma_{\sigma 1T} \qquad (1.16)$$

$$u(0) = 0\ ;\ \theta(0) = \theta_0, \qquad in\ \Omega_T \qquad (1.17)$$

Here, $u_0 = 0$ and θ_0 represent the initial displacement and the initial temperature, respectively. Also, a volume force of density f acts in Ω_T and a surface traction of density g acts on $\Gamma_{\sigma 1T}$.

We will consider a nonlocal Coulomb friction law and in fact a regularization of it in order that the boundary terms in the formulation of our problem make sense. In the sequel, $\mathcal{F} : H^{-\frac{1}{2}}(\Gamma) \to L^2(\Gamma)$ will represent a smoothing operator that is linear,

ontinuous and this satisfy,

$$(\mathcal{T}\sigma(u))_n \leq 0 \; if \; \sigma_n(u) \leq 0 \; , \; on \; \Gamma_{c|T} \quad (1.18)$$

2.Variational formulation. Existence and uniqueness results

In order to obtain the *variational formulation* of *Problem* **(P)** , let us introduce additional notation and assumptions on the problem data.

Let, $\varepsilon : \mathbb{H}_1 \to \mathcal{H}_1$ and $div : \mathcal{H}_1 \to \mathbb{H}$ the *Hooke deformation* and *divergente operators*, respectively, defined by:

$$\varepsilon(u) = \left(\varepsilon_{ij}(u)\right)_{i,j=\overline{1,d}} \; ;$$
$$\varepsilon_{ij}(u) = \frac{1}{2}\left(u_{i,j} + u_{j,i}\right) \; ;$$
$$div\,\sigma = (\sigma_{ij,j})_{i,j=\overline{1,d}} \; .$$

Also, we denote the real Hilbert spaces $\mathbb{H}$, $\mathcal{H}$, $\mathbb{H}_1$ and $\mathcal{H}_1$ respectively:

$$\begin{aligned} &H := L^2(\Omega) \; ; \; \mathbb{H} := L^2(\Omega)^d \; ; \\ &H_1 := H^1(\Omega) \; ; \\ &\mathcal{H} := \{\sigma = (\sigma_{ij}) \in \mathcal{S}_d : \\ &\qquad \sigma_{ij} \in L^2(\Omega)\} = \mathcal{S}_d(H) ; \\ &\mathcal{H}_1 := \{\sigma \in \mathcal{H} : \operatorname{div}\sigma \in \mathbb{H}\} ; \\ &\mathbb{H}_1 := \{u \in \mathbb{H} : \varepsilon(u) \in \mathcal{H}\} \end{aligned} \quad (2.1)$$

and the cannonical inner products, defined by:

$$(u,v)_H = \int_\Omega u \cdot v \, dx \; ;$$
$$(u,v)_{\mathbb{H}} = \int_\Omega u \cdot v \, dx \; ;$$
$$(u,v)_{H_1} = \int_\Omega u \cdot v \, dx + \int_\Omega \nabla u \cdot \nabla v \, dx \; ;$$
$$\|u\|_{\mathbb{H}}^2 = (u,u)_{\mathbb{H}} \; ; \quad \|u\|_{H_1}^2 = (u,u)_{H_1} \; ;$$
$$(\sigma,\tau)_{\mathcal{H}} = \int_\Omega \sigma(\varepsilon(u)) : \tau(\varepsilon(u)) \, dx = \int_\Omega \sigma_{ij}\tau_{ij} \, dx \; ;$$
$$\|\sigma\|_{\mathcal{H}}^2 = (\sigma,\sigma)_{\mathcal{H}} \; ;$$
$$((u,v))_{\mathbb{H}_1} = (u,v)_{\mathbb{H}} + (\varepsilon(u),\varepsilon(v))_{\mathcal{H}} \; ;$$
$$\|u\|_{\mathbb{H}_1}^2 = ((u,u))_{\mathbb{H}_1} \; ;$$
$$((\sigma,\tau))_{\mathcal{H}_1} = (\sigma,\tau)_{\mathcal{H}} + (\operatorname{div}\sigma, \operatorname{div}\tau)_{\mathbb{H}} \; ;$$
$$\|\sigma\|_{\mathcal{H}_1}^2 = ((\sigma,\sigma))_{\mathcal{H}_1} \; .$$

We denoted by $\|\cdot\|_{\mathbb{H}}$, $\|\cdot\|_{\mathcal{H}}$, $\|\cdot\|_{\mathbb{H}_1}$ and $\|\cdot\|_{\mathcal{H}_1}$ the cannonical norms induced by coresponding inner products in the respectively spaces.

For every element $v \in \mathbb{H}_1$ we also use the notation v to denote the trace of v or Γ (i.e. $\gamma_0 v = v|_\Gamma$) and, we denote by v_n and v_τ the *normal* and the *tangential components* of v on Γ given by,

$$v_n = v \cdot n \; ; \; v_\tau = v - v_n n \quad (2.2)$$

We also denote by σ_n and σ_τ the *normal* and the *tangential traces* of the element $\sigma \in \mathcal{H}_1$ given by,

$$\sigma_n = (\sigma \cdot n) \cdot n \; ; \; \sigma_\tau = \sigma n - \sigma_n n \quad (2.3)$$

We recall that the following *Green's formula* holds: for a regular function $\sigma \in \mathcal{H}_1$ fixed, and $(\forall)\, v \in \mathbb{H}_1$

$$(\sigma, \varepsilon(v))_{\mathcal{H}} + (\operatorname{div}\sigma, v)_{\mathbb{H}} = - \langle \sigma n, v \rangle_{H^{-\frac{1}{2}}(\Gamma)^d \, . \, H^{\frac{1}{2}}(\Gamma)^d} \quad (2.4)$$

We remember that the elastic-viscoplastic body is occupies of the regular domain $\Omega \subset \mathbb{R}^d$ with the surface Γ that is a *sufficiently regular* boundary, portionned into three disjoint measurable part,

$$\Gamma = \Gamma_u \cup \Gamma_\sigma \cup \Gamma_c$$

such that $ds - meas\,(\Gamma_u) > 0$.

Thus, we define the closed subspaces $\mathbb{V}$ and U of $\mathbb{H}_1$ and H_1, respectively, by:

$$\mathbb{V} := \{v \in \mathbb{H}_1 : v = 0, \; \text{on } \Gamma_u\} \quad (2.5)$$

$$U := \{\theta \in H_1 : \theta = 0 \; , \text{on } \Gamma_u \cup \Gamma_\sigma\} \quad (2.6)$$

and $\mathbb{K}$ be the convexe set of admisible displacements given by,

$$\mathbb{K} := \{v \in \mathbb{V} : v_n \leq 0 \; , \text{on } \Gamma_c\} \quad (2.7)$$

Since $ds - meas\,(\Gamma_u) > 0$, Korn's inequality holds (see [9], 1997 - pp.291) and there exists $\alpha > 0$, depending only on Ω and Γ_u, such that:

$$((\sigma,\tau))_{\mathcal{H}_1} = (\sigma,\tau)_{\mathcal{H}} + (\operatorname{div}\sigma, \operatorname{div}\tau)_{\mathbb{H}} \; ;$$
$$\|\sigma\|_{\mathcal{H}_1}^2 = ((\sigma,\sigma))_{\mathcal{H}_1} \; .$$
$$|v|_{\mathbb{H}_1} \leq \alpha \|\varepsilon(v)|_{\mathcal{H}} \; , \; (\forall)\, v \in \mathbb{V}. \quad (2.8)$$

Hence, on $\mathbb{V}$ we consider the inner product given by,

$$(u,v)_{\mathbb{V}} = (\varepsilon(u) \, . \, \varepsilon(v))_{\mathcal{H}} \; , \; (\forall)\, u, v \in \mathbb{V} \quad (2.9)$$

and the associated norm,

$$\|v\|_{\mathbb{V}} = \|\varepsilon(v)\|_{\mathcal{H}} \; , \; (\forall)\, v \in \mathbb{V} \; .$$

It follows that $\|\cdot\|_{\mathbb{H}_1}$ and $\|\cdot\|_{\mathbb{V}}$ are equivalent norms on $\mathbb{V}$ and therefore $(\mathbb{V}, \|\cdot\|_{\mathbb{V}})$ is a real Hilbert space.

Moreover, by the Soblev's trace theorem and (2.9), we have constant $\gamma > 0$ depending only on the domain Ω and the its boundaries Γ_u and Γ_c such that,

$$\|v\|_{\mathbb{L}^2(\Gamma_c)^d} \leq \gamma \|v\|_{\mathbb{H}_1}, \quad (\forall)\, v \in \mathbb{V} \qquad (2.10)$$

In an analogous way, we can prove that the norm $\|\theta\|_U \leq \|\nabla\theta\|_{\mathbb{H}}$, $(\forall)\, \theta \in U$ associated to the inner product on U given by $(\theta,\eta)_U = (\nabla\theta,\nabla\eta)_{\mathbb{H}}$ is equivalent to the classical norm on H_1 .

Hence $(U, \|\cdot\|_U)$ is a real Hilbert spaces. We also recall, that for every real Banach spaces E we use the notation $C^0([0,T];E)$ and $C^1([0,T];E)$ for the space of continuous and continuously differentiable function from $[0,T]$ to E, respectively, $C^0([0,T];E)$ is a real Banach space with the norm ,

$$\|u\|_{C^0([0,T];E)} = \max_{t\in[0,T]} \|u(t)\|_E \qquad (2.11)$$

while $C^1([0,T];E)$ is the real Banach space with the norm,

$$\|u\|_{C^1([0,T];E)} = \|u\|_{C^0([0,T];E)} + \|\dot{u}\|_{C^0([0,T];E)} \qquad (2.12)$$

If $k \in \mathbb{N}$ and $p \in [1,\infty]$ are arbitrary, then we use the standard notation for the Lebesgue spaces $L^p(0,T;E)$ and for the Sobolev spaces $W^{k,p}(0,T;E)$,

$$\|u\|_{W^{k,p}(0,T;E)} = \sum_{|m|\leq k} \|D^m u\|_{L^p(0,T;E)} \qquad (2.13)$$

While the Banach spaces E is $W^{k,p}(\Omega)$ we have,

$$\|u(t)\|_E = \|u(t)\|_{k,p,\Omega} = \sum_{|m|\leq k} \|D^m u(t)\|_{p(\Omega)} = \sum_{|m|\leq k} \left(\int_\Omega \|D^m u(t)(x)\|^p\, dx\right)^{\frac{1}{p}} \qquad (2.14)$$
$$t \in [0,T];\ m \in \mathbb{N}^k$$

In this paper we use as an example $E = \mathbb{V}$, and we also use the Sobolev space $W^{1,\infty}(0,T;\mathbb{V})$ equipped with the norm ,

$$\|u\|_{W^{1,\infty}(0,T;\mathbb{V})} = \|u\|_{L^\infty(0,T;\mathbb{V})} + \|\dot{u}\|_{L^\infty(0,T;\mathbb{V})} = \operatorname{ess\,sup}_{t\in[0,T]} \|u(t)\|_{\mathbb{V}} + \operatorname{ess\,sup}_{t\in[0,T]} \|\dot{u}(t)\|_{\mathbb{V}} = \operatorname{ess\,sup}_{t\in[0,T]} \|\varepsilon(u(t))\|_{\mathcal{H}} + \operatorname{ess\,sup}_{t\in[0,T]} \|\varepsilon(\dot{u}(t))\|_{\mathcal{H}} \qquad (2.15)$$

Finally, we recall the following abstract result concerning some evolution equations (see [2], 1997-pp.151; [9], 1997- pp.124), and which will be used in *Section 3.* of this paper.

Theorem 2.1

Let $V \subset H \subset V'$ be a *Gelfand triple* , and $A : V \to V'$ is a *hemicontinuous* and *monotone* operator, i.e. $(\exists)\, \alpha,\gamma,\delta \in \mathbb{R}, (\alpha,\gamma > 0)$ such that,

$$\langle Av, v\rangle_{V',V} \geq \alpha\|v\|_V^2 + \delta\,, \quad (\forall)\, v \in \mathbb{V} \qquad (2.16)$$

$$\|Av\|_{V'} \leq \gamma(\|v\|_V + 1)\,, \quad (\forall)\, v \in \mathbb{V}\,. \qquad (2.17)$$

If $u_0 \in H$ and $f \in L^2(0,T;V')$ are given functions, then the *evolution operatorial problem* ,

$$\begin{cases} \dot{u}(t) + Au(t) = f(t)\,, & t \in (0,T) \\ u(0) = u_0 \end{cases} \qquad (2.18)$$

has a *unique solution* which satisfies the L^2-regularity properties,

$$\begin{aligned} &u \in L^2(0,T;V) \cap C^0([0,T];H) \\ &\dot{u} \in L^2(0,T;V')\,. \end{aligned} \qquad (2.19)$$

We recall the Green formula, which is valid in this regular functional context :

$$\left(\sigma(\varepsilon(u)), \varepsilon(v)\right)_{\mathcal{H}} + \left(div\,\sigma(\varepsilon(u)),\, v\right)_{\mathbb{H}} = \langle \sigma(\varepsilon(u))\cdot n\,, v\rangle_{V',V}\,, \quad (\forall)\, v \in \mathbb{H}_1$$

where, we denote the functional spaces :

$$X = \mathrm{L}^2(\Gamma)\ ;\ Y = \mathrm{H}^{\frac{1}{2}}(\Gamma)\ ;$$
$$X_i = \mathrm{L}^2(\Gamma_i)\ ;\ Y_i = \mathrm{H}^{\frac{1}{2}}(\Gamma_i)\ ;\ (i = u,\sigma,c)$$
$$\mathbb{X} = \mathrm{L}^2(\Gamma)^d\ ;\ \mathbb{Y} = \mathrm{H}^{\frac{1}{2}}(\Gamma)^d\ ;$$
$$\mathbb{X}_i = \mathrm{L}^2(\Gamma_i)^d\ ;\ \mathbb{Y}_i = \mathrm{H}^{\frac{1}{2}}(\Gamma_i)^d\ ;\ (i = u,\sigma,c)$$
$$Y' = \mathrm{H}^{-\frac{1}{2}}(\Gamma)\ ;\ \mathbb{Y}' = \mathrm{H}^{-\frac{1}{2}}(\Gamma)^d\ ;$$
$$Y_i' = \mathrm{H}^{-\frac{1}{2}}(\Gamma_i)\ ;\ \mathbb{Y}_i' = \mathrm{H}^{-\frac{1}{2}}(\Gamma_i)^d\ ;\ (i = u,\sigma,c)$$

and obtained,

$$\sigma(u)\cdot n \in \mathbb{Y}'\,, \quad (\forall)\, \sigma \in \mathcal{H}_1.$$

Let $\mathbb{V}$ denote the closed subspace of $\mathbb{H}_1$ defined by,

$$\mathbb{V} = \{v \in \mathbb{H}_1 : v = 0\,, on\ \Gamma_u\} \qquad (2.20)$$

We note that the *Korn inequality* holds (see [9], 1997-pp. 96), i.e. exist $\alpha > 0$ only depend by Ω *and* Γ_u :

$$\|\varepsilon(u)\|_{\mathcal{H}} \geq \alpha\|u\|_{\mathbb{H}_1}\,, \quad (\forall)\, u \in \mathbb{V}\,.$$

By using the inner product on $\mathbb{V}$,

$$(u,v)_{\mathbb{V}} = (\varepsilon(u),\varepsilon(v))_{\mathcal{H}}\,,$$

and the norm induced $\|u\|_{\mathbb{V}} = (u,u)_{\mathbb{V}}$ we obtain that $\mathbb{V}$ is a Hilbert space.

Next, we denote by $t \to F(t)$ an element of $\mathbb{V}'$ given by:

$$\begin{aligned} &\langle F(t), v\rangle_{\mathbb{V}',\mathbb{V}} = (f(t), v)_{\mathbb{H}} + \\ &(g(t), \gamma_0 v)_{\mathbb{X}_\sigma},\ (\forall)\, v \in \mathbb{V},\ t \in [0,T] \end{aligned} \tag{2.21}$$

where, f and g are input data, and $\gamma_0 v \in \mathbb{Y}_\sigma \subset \mathbb{X}_\sigma$ is the trace over Γ of the vector $v \in \mathbb{V} \subset \mathbb{H}_1$.

For the *variational* description of the *friction law*, we denote the *friction functional*,

$$\begin{aligned} &j : \mathcal{H}_1 \times \mathbb{V} \to \mathbb{R}\ , \\ &j(\sigma, v) = \int_{\Gamma_c} |\mu|\,|\mathcal{T}\sigma_n|\,|v_\tau|\ ds \end{aligned} \tag{2.22}$$

where,

$|\mu| = \|\mu\|_{\mathbb{X}_\sigma}$; $|v_\tau| = \|\gamma_0 v - \gamma_\nu v\|_{\mathbb{X}_\sigma}$;

$\mathcal{T} : \mathbb{Y}_\sigma' = H^{-\frac{1}{2}}(\Gamma_c)^d \to \mathbb{X}_\sigma = L^2(\Gamma_c)^d$ i.e.

$|\mathcal{T}\sigma_n| = \|\mathcal{T}\sigma_n(v)\|_{\mathbb{X}_\sigma}$;

Thus, for the *variational* description of the *unilateral contact condition*, we introduce the space $\mathbb{Y}_\sigma = H^{\frac{1}{2}}(\Gamma_c)$ as the set of restrictions to Γ_c of the $\mathbb{Y} = H^{\frac{1}{2}}(\Gamma)$ functions which are null on Γ_u.

Also, we denote by $\langle \cdot, \cdot \rangle_{\mathbb{V}',\mathbb{V}}$ the duality pairing between $\mathbb{Y}_\sigma = H^{\frac{1}{2}}(\Gamma_c)$ and its dual $\mathbb{Y}_\sigma' = H^{-\frac{1}{2}}(\Gamma_c)$,

$$\begin{aligned} &\langle \sigma_n(t), u_n\rangle_{\mathbb{Y}_\sigma',\mathbb{Y}_\sigma} = \int_{\Gamma_c} \sigma_n(t)\, u_n\ ds, \\ &(\forall)\, v \in \mathbb{V},\ \sigma \in \mathcal{H}_1,\ \text{a.p.t. } t \in (0,T). \end{aligned} \tag{2.23}$$

Now, let us introduce the *convex* set of admisible displacements, defined by

$$\mathbb{K} = \{ v \in \mathbb{V} : v_n \le 0 \text{ , on } \Gamma_c \}. \tag{2.24}$$

Finally, in the study of the thermo-mechanical problem $(P) \equiv (1.6) - (1.17)$ we assume that the operators $\mathcal{A}$, $\mathcal{G}$ satisfies some regularity conditons ([5], [6], [12]).

Thus, the *variational formulation* for thermo-mechanical problem $(P) \equiv (1.6) - (1.17)$ is obtained.

Problem (VP) : Find,

a *displacement field* $u : [0,T] \to \mathbb{V}$,

a *stress field* $\sigma : [0,T] \to \mathcal{H}$ which satisfy the *evolutionary quasivariational problem*:

$$\sigma = \mathcal{A}(\varepsilon(\dot{u})) + \mathcal{G}(\varepsilon(u)),\ t \in (0,T) \tag{2.25}$$

$$\begin{aligned} &(\sigma(t),\ \varepsilon(v) - \varepsilon(\dot{u}(t)))_{\mathbb{H}} + \\ &+ j(\sigma(t), v) - j(\sigma(t), \dot{u}(t)) \ge \\ &\ge \langle F(t), v - \dot{u}(t)\rangle_{\mathbb{V}',\mathbb{V}} + \\ &\langle \sigma_n(t), v_n - \dot{u}_n(t)\rangle_{\mathbb{Y}_\sigma', \mathbb{Y}_\sigma}, \\ &(\forall)\, v \in \mathbb{V}\ , \text{ a.p.t.} \\ &t \in (0,T)\ . \end{aligned} \tag{2.26}$$

$$\begin{aligned} &\langle \sigma_n(t), w_n - u_n(t)\rangle_{\mathbb{Y}_\sigma', \mathbb{Y}_\sigma} \\ &(\forall)\, w \in \mathbb{K}\ ,\ (\forall)\, t \in [0,T] \end{aligned} \tag{2.27}$$

$$u(0) = u_0 \tag{2.28}$$

We assume that the *input data* of *quasivariational problem* (**VP**) ≡ (2.25)-−(2.28) satisfies the minimum regularity conditions,

$$\begin{aligned} &f \in L^\infty(0,T;\mathbb{H})\ ;\ g \in L^\infty(0,T;\mathbb{X}_\sigma) \\ &u_0 \in \mathbb{K} \end{aligned} \tag{2.29}$$

Theorem 2.2 ([7])

(for the *existence* of *weak solution* $\{ u : \sigma \}$)

Assume that the input data satisfies the minimum regularity conditions (2.29) , and the regularity hypotesis for the *elasticity operator* $\mathcal{G}$ and for the *viscoplasticity operator* $\mathcal{A}$ respectively, to hold good.

Then, there exist a *weak solution* $\{ u : \sigma \}$ to the problem (**VP**) ≡(2.25)−(2.28) satisfying the minimum regularity conditions,

$$\begin{aligned} &u \in W^{1,\infty}(0,T;\ \mathbb{V}) \cap C([0,T];\mathbb{K}), \\ &\sigma \in L^\infty(0,T;\ \mathcal{H}_1). \end{aligned} \tag{2.30}$$

Remark 2.3

We could have taken data f and g with the L^2 – *regularity properties* in the time variable,

$$f \in L^2(0,T;\mathbb{H})\ ;\ g \in L^2(0,T;\mathbb{X}_\sigma) \tag{2.31}$$

and $u_0 \in \mathbb{K}$, then we would obtain the existence of weak solutions for the problem (**VP**), also, satisfying the L^2–*regularity properties*,

$$u \in H^1(0,T;\ \mathbb{K});\ \sigma \in L^2(0,T;\ \mathcal{H}_1) \tag{2.32}$$

3. Main existence and uniqueness results

In this section we use the *temporal semi-discretization Galerkin method* for the proof of the existence concerning the weak solutions of the (**VP**) problem, (see [5], [6], [12]). For this, we need the

following notations, which assume to introduce a new variational formulation of the initial problem (**P**).

We define the following functionals,

$a : \mathbb{V} \times \mathbb{V} \to \mathbb{R}$ a *bilinear form* by,

$$a(u,v) = \left(\mathcal{A}(\varepsilon(u)),\ \varepsilon(v)\right)_{\mathcal{H}}; \tag{3.1}$$

$b : \mathbb{V} \times \mathbb{V} \to \mathbb{R}$, a *linear form* only with respect to the second argument given by,

$$b(u,v) = \left(\mathcal{G}(\varepsilon(u)),\ \varepsilon(v)\right)_{\mathcal{H}}; \tag{3.2}$$

$l : \mathbb{V} \to \mathbb{R}$ *linear form*,

$$\begin{aligned} l(v) &= (f(t), v)_{\mathbb{H}} + \\ &(g(t), \gamma_0 v)_{\mathbb{H}_\sigma} + \langle \sigma_n(t), v_n \rangle_{V_\sigma', V_\sigma} \\ &= \int_\Omega f(t) v\, dx + \\ &+ \int_{\Gamma_\sigma} g(t) v\, da + \int_{\Gamma_\sigma} \sigma_n(t) v_n\, da \end{aligned} \tag{3.3}$$

a.p.t. $t \in (0,T)$;

Thus, the *quasi-variational evolutionary problem* (**VP**) ≡(2.25)−(2.28) find,

a *displacement field* $u : [0,T] \to \mathbb{V}$, and

a *stress field* $\sigma : [0,T] \to \mathcal{H}$

which satisfies the following *problem for a quasi-variational inequality*,

$$\sigma = \mathcal{A}\left(\varepsilon(u) + \mathcal{G}(\varepsilon(u))\right),\ t \in (0,T) \tag{3.4}$$

$$\begin{aligned} &a\left(\dot{u}(t),\ v - \dot{u}(t)\right) + \\ &b\left(u(t),\ v - \dot{u}(t)\right) + j(\sigma(t),\ v) - \\ &- j\left(\sigma(t),\ \dot{u}(t)\right) \geq l\left(v - \dot{u}(t)\right), \\ &\qquad (\forall)\ v \in \mathbb{V}\ ,\ \text{a.p.t.}\ \ t \in (0,T) \end{aligned} \tag{3.5}$$

$$\begin{aligned} &\langle \sigma_n(t), v_n - u_n(t) \rangle_{V_\sigma', V_\sigma} \geq 0\ , \\ &\qquad (\forall)\ v \in \mathbb{K}\ ,\ \ (\forall)\ t \in [0,T] \end{aligned} \tag{3.6}$$

$$u(0) = u_0. \tag{3.7}$$

4. Conclusions

In the present paper has been investigated a mathematical model for as well triboprocess involving the coupling thermal and mechanical aspects by specific behaviour laws of materials.

The contact condition for this quasistatic processes has described as effect of a normal and tangential damped response properties.

The *classical* as well as a *variational formulations* of the thermo-mechanical problem are presented.

References

[1]. Amassad A., Kuttler L., Rochdi M., Shillor M. - *Quasistatic thermo-viscoelastic contact problem with slip dependent friction coefficient*, Math. Computational Modelling, No. **36**, pp.839-854, 2007

[2]. Andrews K.T., Kuttler K.L, Shillor M. - *On the Dynamic behaviour of a Thermo-Viscoplastic Body in Frictional Contact with a Rigid Obstacle*, European J. Applied Mathematics , vol.**8**, pp.417-436, 1997

[3]. Ayyad Y., Sofonea M. - *Analysis of two Dynamic Frictionless Contact Problems for Elastic-Visco-Plastic Materials*, EJDE , No.**55** , pp.1-17, 2007

[4]. Barbu V. - *Nonlinear Semigroups and Differential Equations in Banach Spaces*, Bucharest–Noordhoff, Leyden, 1976

[5]. Bendrea C. - *Variational evolutionary problems and quasi-variational inequalities for mathematical modeling of the tribological processes concerning continuous casting machine*, Thesis, Galati, 2008

[6]. Bendrea C., **Munteanu V**. - *Thermal Analysis of an Elastic-Viscoplastic Unilateral Contact Problem in the Continuous Casting of the Steel*, Metalurgia International, Vol XIV (2009), No **5**, pp. 72

[7]. Campo M., Fernandez J.R. - *Numerical analysis of a quasistatic thermo—viscoelastic frictional contact problem*, Comput.Math., No.**35**, pp.453- 469, 2005

[8]. Chau O., **Fernandez J.R**., **Han W**., **Sofonea M**. - *A frictionless contact problem for elastic-viscoplastic materials with normal compliance and damage*, Comput. Methods Appl. Mech. Engrg., **191**, pp.5007-5026, 2002

[9]. Ciarlet P.G. - *Mathematical Elasticity* (*vol.* I, II), Elsevier , Amsterdam – New-York, 1997

[10]. Fernandez J.R, Sofonea M., Viano J.M. - *A Frictionless Contact Problem for Elastic-Viscoplastic Matherials with Normal Compliance: Numerical Analysis and Computational Experiments*, Comput. Methods Appl. Mech. Engrg., vol. **90**, pp.689-719, 2002

[11]. Han W., Sofonea M. - *Quasistatic Contact Problems in Viscoelasticity and Viscoplasticiy*, AMS , Int. Press, 2001

[12]. Moitra A.,Thomas B.G. - *Applications of a Thermo-Mechanical Finite Element Method of Steel Shell Behaviour in the Continuous Slab Casting Mold*, SteelMaking Proceedings, vol.**76**, pp.657-667, 1998

[13]. Munteanu V., **Bendrea C**. - *A Thermoelastic Unilateral Contact Problem with Damage and Wear in Solidification Processes Modeling*, Metalurgia International, Vol XIV (2009), No **5**, pp. 83

[14]. Thomas B.G., O'Malley R., Stone G. - *Measurement of Temperature , Solidification and Microstructure in a Continuous Cast Thin Slab* , ISIJ Int., vol.**46**, No.**10** , pp.1394-1415, 2006

[15]. Wang H., Li G.; et. al.- *Mathematical Heat Transfer Model Research for the Improvement of Continuous Casting Slab Temperature*, ISIJ Int. vol.**45**, No.**9**, pp.1291-1296.2005

MANUSCRISELE, CĂRŢILE ŞI REVISTELE PENTRU SCHIMB, PRECUM ŞI ORICE CORESPONDENŢE SE VOR TRIMITE PE ADRESA:

MANUSCRIPTS, REVIEWS AND BOOKS FOR EXCHANGE COOPERATION, AS WELL AS ANY CORRESPONDANCE WILL BE MAILED TO:

LES MANUSCRIPTS, LES REVUES ET LES LIVRES POUR L'ECHANGE, TOUT AUSSI QUE LA CORRESPONDANCE SERONT ENVOYES A L'ADRESSE:

MANUSCKRIPTEN, ZIETSCHRITFTEN UND BUCHER FUR AUSTAUCH SOWIE DIE KORRESPONDENZ SID AN FOLGENDE ANSCHRIFT ZU SEDEN:

After the latest evaluation of the journals achieved by National Center for the Science and Scientometry Politics (**CENAPOSS**), as recognition of its quality and impact at national level, the journal is included in B^+ category, 215 code (http://www.cncsis.ro/2006_evaluare_rev.php).

The journal is indexed in Cambridge Scientific Abstract
http://www.cncsis.ro/userfiles/file/CENAPOSS/B+feb_2011(9).pdf

The papers published in this journal can be visualized on the "Dunarea de Jos" University of Galati site, the Faculty of Metallurgy, Material Science and Environment, page: www.fmsm.ugal.ro.

Publisher's Name and Address:
Contact person: Prof. Dr. Eng. Elena MEREUTA
Galati University Press - GUP
47 Domneasca St., 800008 - Galati, Romania
Phone:+40 336 130103, Fax: +40 236 461353
Email: elena.mereuta@ugal.ro

Editor's Name and Address:
Prof. Dr. Eng. Marian BORDEI
Dunarea de Jos University of Galati, Faculty of Metallurgy, Materials Science and Environment
111 Domneasca St., 800201 - Galati, Romania
Phone: +40 336 130223, Phone/Fax: +40 236 460750
Email: mbordei@ugal.ro

AFFILIATED WITH:

- *ROMANIAN SOCIETY FOR METALLURGY*
- *ROMANIAN SOCIETY FOR CHEMISTRY*
- *ROMANIAN SOCIETY FOR BIOMATERIALS*
- *ROMANIAN TECHNICAL FOUNDRY SOCIETY*
- *THE MATERIALS INFORMATION SOCIETY (ASM INTERNATIONAL)*

Annual subscription (4 issues per year)

Edited under the care of
Faculty of
METALLURGY, MATERIALS SCIENCE AND ENVIRONMENT
and
Center for Nanostructures and Functional Materials (CNMF)

Edited date: 30.12.2011
Issues number: 200
Printed by
Galati University Press
accredited CNCSIS
47 Domnească Street, 800036
Galati, Romania